Influence of ΛNN forces and the nuclear core size on the $^{7}_{\Lambda}$Li level spectrum

V. N. Fetisov*)
Lebedev Physics Institute, Russian Academy of Sciences, 117924 Moscow, Russia

(Submitted 25 June 1999)
Pis'ma Zh. Éksp. Teor. Fiz. **70**, No. 4, 229–234 (25 August 1999)

An effective zero-range ΛNN interaction with the Λ-spin dependence peculiar to dispersive ΛNN forces is introduced in order to estimate its influence on the shell model spectra of light hypernuclei. The parameters of the three-body and pair interactions are evaluated using the values of B_Λ for *s*-shell hypernuclei with $A=4$ and 5. It is shown that the description of the $^{7}_{\Lambda}\mathrm{Li}_{\mathrm{g.s.}}$ doublet energy $\Delta E \simeq 689$ keV, when fitted together with other hypernuclei, gives a reduced radius $R \simeq 2.2$ fm for ^{6}Li bound in $^{7}_{\Lambda}$Li (compared to $R \simeq 2.4$ fm for the free nucleus ^{6}Li) and a dispersive ΛNN force contribution to this energy of ~ 250 keV. A more refined version of the $^{7}_{\Lambda}$Li level spectrum is proposed, including ΛN and ΛNN forces and the compression of the ^{6}Li core. © *1999 American Institute of Physics*. [S0021-3640(99)00116-4]

PACS numbers: 21.80.+a, 21.30.Fe, 21.60.Cs

The current shell model calculations of hypernuclear spectra are based on the pair ΛN interaction, in which case the coupling of the Λ and Σ channels is disregarded.[1,2] However, it is of interest to estimate the contributions of ΛNN forces to the level spacing in connection with the KEK-BNL hypernuclear γ spectroscopy program.[3]

This work was stimulated by results[4] in which a large contribution ($\sim 30\%$) of dispersive ΛNN forces (DF) to the $1^+,0^+$ spin splitting $\Delta E_4(1^+,0^+) \simeq 1.1$ MeV in $^{4}_{\Lambda}$H(He) has been obtained and by the discussion[5] of two forms of DF and their role in light hypernuclei as well.

Recently the $^{7}_{\Lambda}\mathrm{Li}_{\mathrm{g.s.}}$ doublet splitting $\Delta E_7(3/2^+_1,1/2^+) \simeq 689 \pm 4$ keV has been measured in the $(\pi^+,K^+\gamma)$ reaction at KEK.[6] This value exceeds the expected energy[1)] ~ 440 keV evaluated in the shell model with a spin–spin parameter of the ΛN interaction $\Delta(B) \simeq 0.3$ MeV^2 describing hypernuclear levels in the vicinity of $^{10}_{\Lambda}$B. From this KEK result it is inferred that the empirical value of Δ(Li) in $^{7}_{\Lambda}$Li is nearly twice as large as that for heavier hypernuclei.

To elucidate the causes of this difference, let us analyze the dependence of Δ and the $^{7}_{\Lambda}$Li level splitting on the size of the host nucleus (or hypernucleus) and on the ΛNN forces.

For the *p* shell hypernuclei four potential parameters Δ, S_Λ, S_N and T (expressed here in MeV) corresponding to spin–spin, two spin–orbit and tensor parts of ΛN inter-

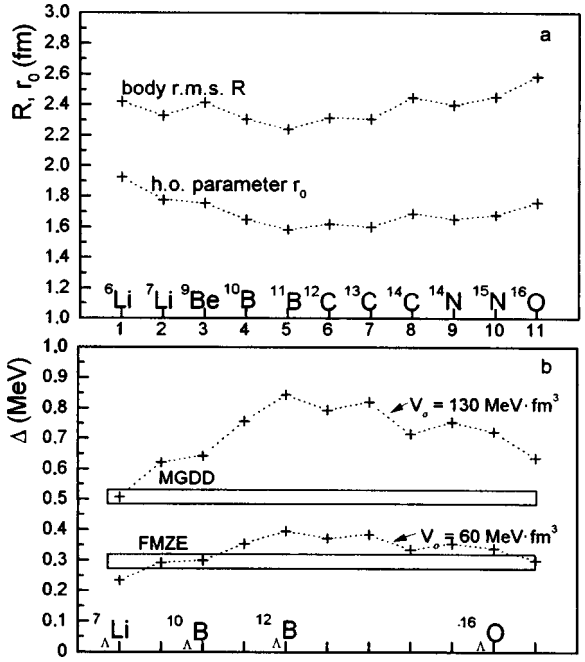

FIG. 1. Nuclear body rms radii, oscillator parameters, and Δ for the p shell hypernuclei.

action determine the level positions.[9] The harmonic oscillator wave functions with a common harmonic oscillator parameter r_0 for the Λ particle and for nucleons are adopted in order to estimate the scale of influence of nuclear sizes on Δ, which is an important parameter for producing a doublet splitting. In this case Δ is of the form

$$\Delta(r_0) = V_\sigma (a/\pi)^{3/2} \frac{(1+ar_0^2-\varepsilon)}{(1+2ar_0^2)^{5/2}}, \tag{1}$$

where $V_\sigma = V_s - V_t$ is a difference of the singlet and triplet volume integrals for the ΛN Gaussian potential $\sim \exp(-ar^2)(1-\varepsilon+\varepsilon P_x)$, with $a = 0.9376\,\mathrm{fm}^{-2}$ (Ref. 10) and $\varepsilon = 0.25$ (Ref. 4).

The body rms radii R and the values of $r_0({}^A Z)$ are shown for the p shell nuclei in Fig. 1a. They were calculated with the Tassie – Barker correction to the center-of-mass motion[11] using the nuclear charge radii and the proton radius ~ 0.8 fm.[12] One of last estimates of $\Delta \simeq 0.5$ has been obtained from a description of $\Delta E_4(1^+,0^+)$ (the MGDD set of parameters).[1] Within the Λ-nucleus model[10] and using ΔE_4 as well we find $V_\sigma \simeq 130\mathrm{MeV}\cdot\,\mathrm{fm}^3$ and a too large value $B_\Lambda({}^5_\Lambda\mathrm{He}) \simeq 6.9$ MeV. For this case Eq. (1) gives the upper curve shown in Fig. 1b. But such large values of Δ were excluded[2] early on by the BNL data.[7] If one accepts $\Delta(B) \simeq 0.3$ (the FMZE set of parameters)[2] and $r_0(B) \simeq 1.74$ fm, then $V_\sigma \simeq 60\,\mathrm{MeV}\cdot\mathrm{fm}^3$, and we have the lower curve in Fig. 1b with $\Delta(\mathrm{Li}) \simeq 0.23$. The value $\Delta(\mathrm{Li}) \simeq 0.23$ is in a contradiction with the KEK data. Indeed, the ${}^7_\Lambda$Li doublet splitting can be written to good accuracy as

$$\Delta E_7\left(\frac{3^+}{2_1},\frac{1^+}{2}\right)\simeq\frac{3}{2}\beta^2\Delta(\mathrm{Li}), \tag{2}$$

where $\beta=0.992$ is the amplitude of the dominant ^{13}S state in the $^6\mathrm{Li}_{\mathrm{g.s.}}$ wave function.[13] For the value $\Delta(\mathrm{Li})=0.23$ obtained for the free nucleus ^{6}Li ($r_0=1.92$ fm) the value $\Delta E_7=340$ keV is too small in comparison with $\Delta E_7^{\mathrm{exp}}\simeq 689$ keV. Since Δ is a decreasing function of r_0, in order to reproduce $\Delta E_7^{\mathrm{exp}}$ the bound nucleus ^{6}Li would have to be compressed to unrealistically small sizes ($R\simeq 1.8$ fm, $r_0\simeq 1.45$ fm), in strong contradiction with the scale of compression ($\Delta R/R\simeq 15\%$) predicted by cluster model calculations.[14] These difficulties of the $^7_\Lambda$Li shell model with the pair ΛN forces lead us to consider the role of ΛNN forces.

Two types of ΛNN forces arise from a strong $\Lambda N\leftrightarrow\Sigma N$ coupling. The first of them, $V^{2\pi}_{\Lambda NN}$, is generated due to the sequential double pion exchange accompanied by $\Lambda\Sigma$ conversion[15] and the other type, the so-called dispersive forces $V^{D}_{\Lambda NN}$, occurs when one of baryons of the intermediate ΣN pair interacts with an additional nucleon (3π exchange).[4,5] The direct employment of explicit expressions for ΛNN forces derived by the pion exchange formalism and given in Ref. 5 is not well grounded in the shell model calculations especially due to their indeterminate behavior at small distances between baryons, which is strongly dependent from short-range correlations. Because of the short-range nature of three-body forces on the scale of hypernuclear sizes it seems reasonable to write them in a zero-range approximation preserving the Λ-spin dependence peculiar to dispersive forces:

$$V_{\Lambda NN}=\delta(\mathbf{r}_\Lambda-\mathbf{r}_1)\,\delta(\mathbf{r}_\Lambda-\mathbf{r}_2)(t+t^s\boldsymbol{\sigma}_\Lambda(\boldsymbol{\sigma}_1+\boldsymbol{\sigma}_2)). \tag{3}$$

Here the constant t includes Λ-spin independent parts of the dispersive and 2π-exchange three-body forces which, as calculations show, have a tendency to compensate each other. The spin-dependent term of the potential (3) is nonzero only in the ^{13}S state of a nucleon pair. Obviously it gives no contribution to matrix elements for nuclear cores with total spin $S=0$. These properties of Eq. (3) probably reflect the suppression of $\Lambda\Sigma$ coupling seen explicitly for $^5_\Lambda$He in the two-channel formalism of the s-shell hypernucleus description.[16]

The four volume integrals $V_{s(t)}$ and t, t^s were determined using B_Λ in the $0^+,1^+$ states of $^4_\Lambda$H(He) and $B_\Lambda(^5_\Lambda\mathrm{He})$ within the Λ-nucleus model[10] with Gaussian nuclear wave functions from the equations

$$-\frac{\hbar^2}{2\mu}\frac{d^2\chi_0}{dr^2}+\left\{S\,\exp\left(-\frac{6}{R_3^2}r^2\right)-V(S)\exp\left(-\frac{3}{2R'^2_3}r^2\right)\right\}\chi_0=(-2.22\ \ \mathrm{MeV})\chi_0, \tag{4}$$

$$-\frac{\hbar^2}{2\mu}\frac{d^2\chi_1}{dr^2}+\left\{P\,\exp\left(-\frac{6}{R_3^2}r^2\right)-aV(S)\exp\left(-\frac{3}{2R'^2_3}r^2\right)\right\}\chi_1=(-1.1\ \ \mathrm{MeV})\chi_1, \tag{5}$$

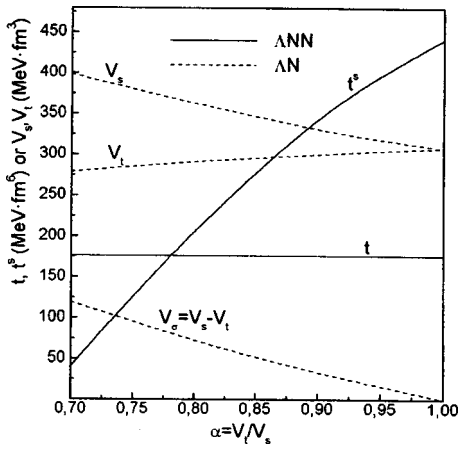

FIG. 2. The volume integrals as functions of α.

$$-\frac{\hbar^2}{2\mu_\alpha}\frac{d^2\chi}{dr^2}+\left\{\frac{81}{16}\left(P+\frac{1}{3}S\right)\left(\frac{R_3}{R_\alpha}\right)^6\exp\left(-\frac{4}{R_\alpha^2}r^2\right)-b\left(\frac{R_3'}{R_\alpha'}\right)^3 V(S)\right.$$

$$\left.\times\exp\left(-\frac{3}{2R'^2_\alpha}r^2\right)\right\}\chi=(-3.12\ \text{MeV})\chi, \tag{6}$$

where χ are the radial functions of the Λ particle;

$$S=\lambda(t-2t^s),\quad P=\lambda\left(t+\frac{2}{3}t^s\right),\quad \lambda=\frac{3^{5/2}}{\pi^3R_3^6},\quad \alpha=V_t/V_s;$$

$$V(S)=\frac{3}{2}(1+\alpha)V_s\left(\frac{3}{2\pi R'^2_3}\right)^{3/2},\quad a=\frac{1+5\alpha}{3(1+\alpha)},\quad b=\frac{2(1+3\alpha)}{3(1+\alpha)};$$

$R_3=\overline{R}(^3\text{H},^3\text{He})=1.6$ fm, $\quad R_\alpha=R(^4\text{He})=1.46$ fm;

$R'_{3(\alpha)}=(R^2_{3(\alpha)}+c)^{1/2},\quad c=1.6026\ \text{fm}^2.$

The volume integrals as functions of the ratio $\alpha=V_t/V_s$ are shown in Fig. 2. For $\alpha\simeq0.67$ one finds $t^s=0$, $V_\sigma\simeq130\ \text{MeV}\cdot\text{fm}^3$, and therefore the entire value of ΔE_4 results from spin–spin ΛN forces. If $\alpha=1$, then $V_\sigma=0$, $t^s\simeq440\ \text{MeV}\cdot\text{fm}^6$, and the total doublet splitting is described by DF. For the acceptable value $V_\sigma\simeq60\ \text{MeV}\cdot\text{fm}^3$ derived from $\Delta(B)=0.3$ we have $\alpha=0.83$ and $t^s=250\ \text{MeV}\cdot\text{fm}^6$.

Now the additional term originates from DF in the final formula for

$$\Delta E_7=\beta^2\left\{\frac{3}{2}V_\sigma(a/\pi)^{3/2}\frac{(1+ar_0(\text{Li})^2-\varepsilon)}{(1+2ar_0(\text{Li})^2)^{5/2}}+\frac{41}{3^{7/2}\pi^3r_0(\text{Li})^6}\cdot t^s\right\}. \tag{7}$$

The curves marked by *a* in Fig. 3 show the separate contributions to ΔE_{tot} from ΛN and ΛNN forces as functions of $r_0(\text{Li})$ (or R) at $V_\sigma=60\ \text{MeV}\cdot\text{fm}^6$. In this case the DF

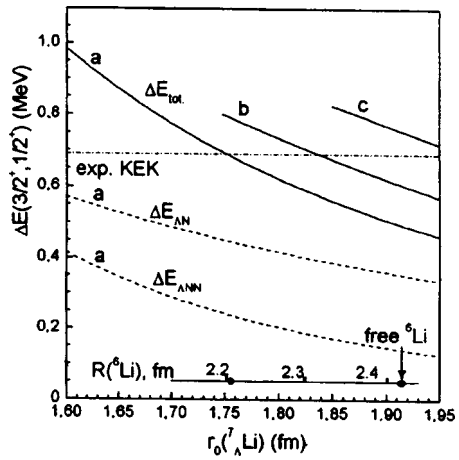

FIG. 3. The dependence of the ${}^{7}_{\Lambda}$Li doublet splitting on r_0 or $R({}^{6}\mathrm{Li})$. The curves are obtained for $V_\sigma = 60\ \mathrm{MeV\cdot fm^3}$ (a), $V_\sigma = 90\ \mathrm{MeV\cdot fm^3}$ (b) and $V_\sigma = 130\ \mathrm{MeV\cdot fm^3}$ (c).

contribution to ΔE_4 is about $1/2\Delta E_4^{\mathrm{exp}} \simeq 500\ \mathrm{keV}$. As Fig. 3 suggests, there is a need to reduce the ^{6}Li radius to $R \simeq 2.2\ \mathrm{fm}$ ($\Delta R/R \simeq 8\%$) in order to reproduce $\Delta E_7^{\mathrm{exp}}$. The parameters used for the curve *b* give somewhat larger values of R and $\Delta(B) \simeq 0.4$, and the DF contribution to ΔE_4 is $\simeq 1/3\Delta E_4^{\mathrm{exp}}$, which is just the value predicted in Ref. 4. Lastly, the curve *c* corresponds to the case when the splitting ΔE_4 is wholly due to spin–spin ΛN forces, and then one needs to increase (!) the ^{6}Li radius to $R \simeq 2.5\ \mathrm{fm}$ to be in agreement with the KEK data.

All the ${}^{7}_{\Lambda}$Li low-lying levels displayed in Fig. 4 have been obtained with Barker's NN interaction[13] using $V_\sigma = 60\ \mathrm{MeV\cdot fm^3}$, $r_0 = 1.74\ \mathrm{fm}$ (for compressed ^{6}Li, $\Delta = 0.3015$), $S_N = -0.4$, $S_\Lambda = -0.02$, $T = 0.02$,[2] $t = 176\ \mathrm{MeV\cdot fm^6}$ and $t^s = 250\ \mathrm{MeV\cdot fm^6}$. The spectrum marked by ΛN is given for $t = t^s = 0$.

The γ deexcitation of the $2049 \pm 2\ \mathrm{keV}\ 5/2^+$ level observed at KEK also is well reproduced with a spin–orbit parameter $-S_N = 0.4$, which is four times the value of $-S_N$ found for other *p* shell hypernuclei. The spectrum depends only on the sum $a + S_N$, where $a = -1.584$ is Barker's single-nucleon spin–orbit constant, taken here for the free nucleus. It suggests that increasing $|S_N|$ should rather be associated with increasing $|a|$ ($\Delta a/a \simeq 20\%$) due to a decrease of the diffuseness of a single-nucleon potential under compression of ^{6}Li. This effect has been recognized recently for ${}^{12}_{\Lambda}$Be and ${}^{16}_{\Lambda}$C in the Skyrme—Hartree–Fock calculations.[17]

In the framework of nuclear and hypernuclear models accepted here it is impossible to reproduce in consistent way the observed ${}^{7}_{\Lambda}\mathrm{Li}_{\mathrm{g.s.}}$ doublet splitting and the level positions in the *s* and *p* shell hypernuclei only with the pair ΛN interaction. A shell model description of this doublet splitting is possible: *i*) if one introduces the Λ-spin dependent dispersive ΛNN forces, and *ii*) if the nuclear core response manifests itself in the compression of ^{6}Li. This conclusion is in line with the cluster model calculations in which a strong ''gluelike'' role of the Λ particle has been revealed[18,14] and the dynamical contraction of ^{6}Li ($\sim 15\%$) has been predicted. In this work the rms radius of bound ^{6}Li as

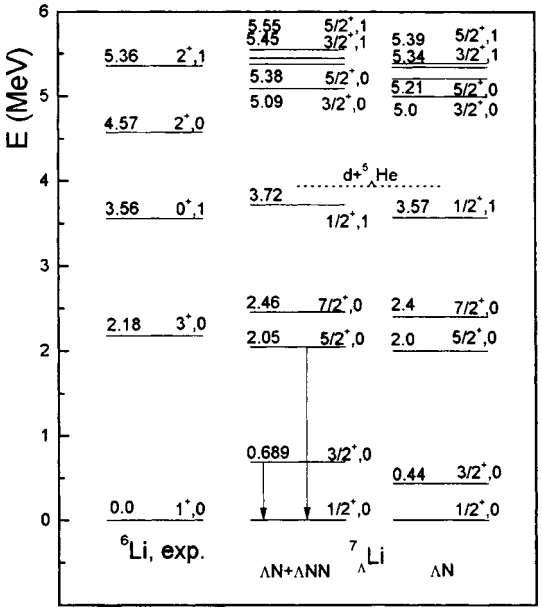

FIG. 4. The measured γ transitions and the new version of the ${}^{7}_{\Lambda}$Li spectrum.

extracted from the doublet splitting is about 2.2 fm, which corresponds to an overall radial compression of $\sim 8\%$ for this nucleus.

The DF contribution to the $T=0$ ground state doublet of ${}^{7}_{\Lambda}$Li is largest and is equal to ~ 250 keV, as against the 50 keV contribution to the $T=1$ doublet in ${}^{7}_{\Lambda}$He. A large value of the induced spin–orbit parameter $|S_N|$ may be an indication of increasing nucleon spin–orbit constant $|a|$ ($\sim 20\%$) due to the compression of ^{6}Li.

The author is very indebted to Profs. H. Tamura and K. Tanida for providing him with the new KEK data, to Profs. D. E. Lanskoy, L. Majling and T. Motoba for helpful discussions, and to Prof. E. Hiyama for sending him papers prior to publication.

*)e-mail: fetisov@sci.lebedev.ru

1)The identification of the ${}^{10}_{\Lambda}$B secondary γ-line with $E_\gamma = 442 \pm 2.1$ keV[7] ascribed[8] to ${}^{7}_{\Lambda}$Li is probably an open problem.

[1] D. J. Millener, A. Gal, C. B. Dover, and R. H. Dalitz, Phys. Rev. C **31**, 499 (1985).
[2] V. N. Fetisov, L. Majling, J. Žofka, and R. A. Eramzhyan, Z. Phys. A **339**, 399 (1991).
[3] H. Tamura, Nucl. Phys. A **639**, 83c (1998); H. Tamura, *Abstracts of the Workshop on Strangeness in Nuclear Physics*, Seoul, Feb. 19–22, 1999, p. 123.
[4] A. R. Bodmer and Q. N. Usmani, Nucl. Phys. A **477**, 621 (1988).
[5] A. Gal, *Proc. of the LAMPF* (π,*K*) *Workshop*, Los Alamos, Oct. 11-13, 1990.
[6] H. Tamura, private communication, January 1999; K. Tanida, *Abstracts of the Workshop on Strangeness in Nuclear Physics*, Seoul, Feb. 19–22, 1999, p. 33.
[7] R. E. Crien, S. Bart, M. May *et al.*, Phys. Rev. C **41**, 1062 (1990).
[8] L. Majling, J. Žofka, V. N. Fetisov, and R. A. Eramzhyan, Z. Phys. A **337**, 337 (1990).
[9] A. Gal, J. M. Soper, and R. H. Dalitz, Ann. Phys. **63**, 53 (1971).
[10] R. H. Dalitz and B. W. Downs, Phys. Rev. **111**, 967 (1958).

[11] L. J. Tassie and F. C. Barker, Phys. Rev. **111**, 940 (1958).
[12] R. C. Barrett and D. F. Jackson, *Nuclear Sizes and Structure*, Clarendon Press, Oxford, 1977.
[13] F. C. Barker, Nucl. Phys. **83**, 418 (1966).
[14] E. Hiyama, M. Kamimura, K. Miyzaki, and T. Motoba, Phys. Rev. C **59**, 2351 (1999).
[15] R. Bhaduri, B. Loiseau, and Y. Nogami, Ann. Phys. (N.Y.) **44**, 67 (1967).
[16] B. F. Gibson, I. R. Afnan, J. A. Carlson, and D. R. Lehman, Suppl. Prog. Theor. Phys. **117**, 339 (1994).
[17] T. Yu. Tretyakova and D. E. Lanskoy, to be published in Eur. Phys. J.
[18] T. Motoba, H. Bandō, and K. Ikeda, Prog. Theor. Phys. **70**, 189 (1983).

Published in English in the original Russian journal. Edited by Steve Torstveit.

Isotope shifts in finite nuclei and the pairing properties of nuclear matter

S. A. Fayans
Kurchatov Institute Russian Science Center, 123182 Moscow, Russia

(Submitted 8 July 1999)
Pis'ma Zh. Éksp. Teor. Fiz. **70**, No. 4, 235–241 (25 August 1999)

A uniform nuclear matter with s-wave pairing is studied within the local energy-density functional approach, incorporating a few parameter sets extracted from the analysis of isotope shifts in finite nuclei. The dilute limit, in which the regime changes from weak to strong pairing, is considered in detail, and, for strong coupling, the ground state properties of that system are found to be completely determined in leading order by the singlet scattering length a_{nn}. The combination of a density-dependent contact pairing interaction and an energy cutoff adjusted to produce a realistic value of a_{nn} is shown to be the preferred choice among the deduced parameter sets. © *1999 American Institute of Physics.* [S0021-3640(99)00216-9]

PACS numbers: 21.65.+f, 21.10.−k

Recent studies[1–3] have shown that nuclear isotope shifts — the differential observables such as the odd–even mass differences and odd–even effects in the charge radii along isotope chains — can be reasonably well reproduced within the local energy-density functional (LEDF) approach with an effective density-dependent contact pairing interaction. The most successful description has been achieved with a phenomenological ''gradient'' force of the form:[2]

$$\mathcal{F}^{\xi}=C_0 f^{\xi}\left(x\left(\frac{\mathbf{r}_1+\mathbf{r}_2}{2}\right)\right)\delta(\mathbf{r}_1-\mathbf{r}_2), \quad f^{\xi}(x(\mathbf{r}))=f^{\xi}_{\mathrm{ex}}+h^{\xi}x^{q}(\mathbf{r})+f^{\xi}_{\nabla}r_0^2(\boldsymbol{\nabla}x(\mathbf{r}))^2, \quad (1)$$

where x is the isoscalar dimensionless density, $x=(\rho_n+\rho_p)/2\rho_0$ with $\rho_{n(p)}$ the neutron (proton) density, and $q=2/3$ (Ref. 3). The normalization factors are the density $2\rho_0$ and the inverse density of states C_0 at the Fermi surface in saturated nuclear matter: $C_0=2\epsilon_{0F}/3\rho_0\equiv\hbar^2\pi^2/k_{0F}m$, with m the free nucleon mass and $\epsilon_{0F}=\hbar^2k_{0F}^2/2m$. Numerically, for the functional DF3 (Ref. 4) used here, $C_0=308.2$ MeV·fm^3, $r_0=1.147$ fm, $2\rho_0=0.1582$ fm^{-3}, $k_{0F}=1.328$ fm^{-1} and $\epsilon_{0F}=36.57$ MeV. As was shown in Ref. 2, self-consistent LEDF calculations with a density-gradient term $\propto f^{\xi}_{\nabla}$ in the pairing force provide the desired size of the isotopic shifts and the right order of odd–even staggering observed in finite nuclei. Different choices of the parameters of the pairing force (1) are possible. In particular, the following sets are deduced for the isotopes of lead:

$$
\begin{aligned}
&f^{\xi}_{\mathrm{ex}}=-0.56, \quad h^{\xi}=0, \quad f^{\xi}_{\nabla}=0 \quad \text{(a)}\\
&f^{\xi}_{\mathrm{ex}}=-1.20, \quad h^{\xi}=0.56, \quad f^{\xi}_{\nabla}=2.4 \quad \text{(b)}\\
&f^{\xi}_{\mathrm{ex}}=-1.60, \quad h^{\xi}=1.10, \quad f^{\xi}_{\nabla}=2.0 \quad \text{(c)}\\
&f^{\xi}_{\mathrm{ex}}=-1.79, \quad h^{\xi}=1.36, \quad f^{\xi}_{\nabla}=2.0 \quad \text{(d)}\\
&f^{\xi}_{\mathrm{ex}}=-2.00, \quad h^{\xi}=1.62, \quad f^{\xi}_{\nabla}=2.0 \quad \text{(e)}\\
&f^{\xi}_{\mathrm{ex}}=-2.40, \quad h^{\xi}=2.16, \quad f^{\xi}_{\nabla}=2.0 \quad \text{(f)}
\end{aligned}
\tag{2}
$$

These LEDF calculations are based on a general variational principle applied to a local functional with a fixed energy cutoff $\epsilon_c=40$ MeV measured from ϵ_F, and on the coordinate-space technique, which involves an integration in the complex energy plane of the Green's functions obtained by solving the Gor'kov equations exactly (see Refs. 3 for details).

In the present paper, the empirical information gained from finite laboratory nuclei is used to study the ground state properties of uniform nuclear matter and the behavior of the energy gap Δ as a function of density $\rho=2\rho_0 x$ (or of the Fermi momentum $k_F=(3\pi^2\rho/2)^{1/3}\equiv k_{0F}x^{1/3}$) in this system. Since the term $\propto f^{\xi}_{\nabla}$ vanishes in this case, only two parameters in (1) are relevant: f^{ξ}_{ex} and h^{ξ}. The gap equation reads

$$
\Delta(x)=-\int_{k\leqslant k_c}\frac{d\mathbf{k}}{(2\pi)^3}F^{\xi}(x)\frac{\Delta(x)}{\sqrt{(\epsilon_k-\epsilon_F(x))^2+\Delta^2(x)}}, \tag{3}
$$

where $k_c=\sqrt{2m(\epsilon_F+\epsilon_c)}/\hbar$, $F^{\xi}(x)=C_0 f^{\xi}(x)$ and $\epsilon_k=\hbar^2k^2/2m$. The solution of Eq. (3) in the weak pairing approximation, $\Delta/\epsilon_F\ll 1$, is given in Eq. (25) of Ref. 5 (see also Eqs. (10) and (22) in Ref. 3). To get a deeper insight into the physics, we can write this solution as

$$
\Delta(k_F)=c\frac{\hbar^2k_F^2}{2m}\exp\left[-\frac{\pi}{2}\cot\delta(k_F)\right], \tag{4}
$$

where we have introduced the Fermi level phase shift $\delta(k_F)$ defined by

$$
k_F\cot\delta(k_F)=-\frac{4k_{0F}}{\pi}\left(\frac{1}{f^{\xi}(k_F)}+\frac{k_c(k_F)}{2k_{0F}}\right)-\frac{k_F}{\pi}\ln\left(\frac{k_c(k_F)-k_F}{k_c(k_F)+k_F}\right), \tag{5}
$$

with $k_c(k_F)=\sqrt{k_{0c}^2+k_F^2}$; $k_{0c}=\sqrt{2m\epsilon_c}/\hbar$, and $c=8e^{-2}\approx 1.083$. Equation (5) corresponds to an exact solution of the nn scattering problem at a relative momentum $k=k_F$ with the states truncated by a momentum cutoff $k_c=k_c(k_F)$ for a contact potential $C_0f^{\xi}(k_F)\delta(\mathbf{r})$ (see, e.g., Ref. 6).

Shown in Fig. 1 are the results for Δ in nuclear matter with the parameter sets of Eq. (2). The approximation (5) works well in the entire range of k_F in Fig. 1 for the set (a), but for the other sets this is true only at k_F greater than ≈ 1.2 fm^{-1} and also, for the sets (b), (c) and (d), at k_F less than 0.42, 0.14, and 0.042 fm^{-1}, respectively (in these regions, $\Delta/\epsilon_F\leqslant 0.1$). It should be stressed that ϵ_F in the integrand of Eq. (3) can be expressed directly in terms of the density ρ as $\epsilon_F=\hbar^2k_F^2(\rho)/2m$, with $k_F(\rho)=(3\pi^2\rho/2)^{1/3}$, only if

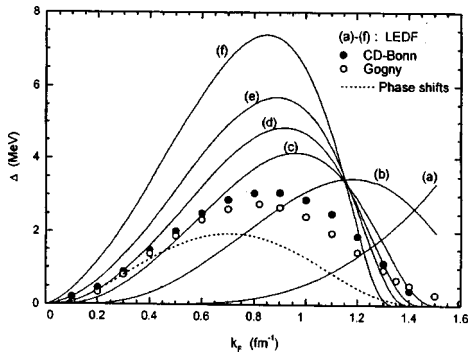

FIG. 1. Pairing gap in nuclear matter as a function of the Fermi momentum. Curves (a)–(f) are calculated using Eqs. (3) and (6) with contact pairing force (1) and correspond, respectively, to the parameter sets (a)–(f) of Eq. (2). The filled (unfilled) circles are the solutions of the nonlocal gap equation with the CD–Bonn potential[7] (with the finite-range Gogny D1 force[8]). The dotted line shows Δ calculated using Eq. (4) with the free nn scattering phase shifts (see text).

the pairing is weak and the dependence of the Fermi energy ϵ_F (and the chemical potential μ) on Δ can be disregarded. Otherwise one should introduce the particle number condition

$$x=\frac{2}{\rho_0}\int_{k\leqslant k_c}\frac{d\mathbf{k}}{(2\pi)^3}n_k(x),\quad n_k(x)=\frac{1}{2}\left(1-\frac{\epsilon_k-\epsilon_F(x)}{\sqrt{(\epsilon_k-\epsilon_F(x))^2+\Delta^2(x)}}\right) \tag{6}$$

and solve the system of two equations (3) and (6) with respect to Δ and ϵ_F. The results shown in Fig. 1 correspond to such a solution.

All parameter sets (2) except (a) reproduce the neutron separation energies and the isotope shifts of the charge radii $\langle r^2\rangle_{ch}$ of lead isotopes fairly well (see Ref. 3). Shown also in Fig. 1 are the values of the $^1S_0$ pairing gap in nuclear matter obtained for the CD–Bonn potential without medium effects (using the free single-particle spectrum $\epsilon_k=k^2/2m$) (Ref. 7) and for the Gogny D1 force in the Hartree–Fock—Bogolyubov framework.[8] The agreement between the two latter calculations is relatively good, while both deviate noticeably from our predictions. The curve for density-independent force, set (a), stands by itself with a positive derivative $d\Delta(x)/dx$ everywhere; no acceptable description of $\langle r^2\rangle_{ch}$ could be obtained in this case.[3]

At very low densities Eq. (5) reduces to

$$k_F\cot\delta(k_F)\approx-\frac{1}{a_{nn}}+\frac{1}{2}r_{nn}k_F^2-\frac{2k_F}{\pi}\left[\frac{k_F}{2k_{0c}}-\frac{2h^\xi}{(f^\xi_{\rm ex})^2}\left(\frac{k_F}{k_{0F}}\right)^{3q-1}\right], \tag{7}$$

where a_{nn} is the singlet scattering length,

$$a_{nn}=\frac{\pi}{2k_{0F}}\left(\frac{\sqrt{2m\epsilon_c}}{\hbar k_{0F}}+\frac{2}{f^\xi_{\rm ex}}\right)^{-1}\equiv\frac{\pi}{4k_{0F}}\left(\frac{1}{f^\xi_{\rm ex}}-\frac{1}{f^\xi_{\rm cr}}\right)^{-1}, \tag{8}$$

and r_{nn} is the effective range, $r_{nn}=4/\pi k_{0c}$. Here we have introduced the critical constant $f^{\xi}_{\rm cr}=-2k_{0F}/k_{0c}$, the value of the vacuum strength $f^{\xi}_{\rm ex}$ at which the two-nucleon problem has a bound state solution at zero energy (in our case, $f^{\xi}_{\rm cr}=-1.912$).

The first two terms in (7) would describe low-energy behavior of the *nn* *s*-wave phase shift through an expansion of $k\cot\delta$ in powers of the relative momentum $k=k_F$ if the interaction were density-independent — i.e., if the coupling strength and momentum cutoff were fixed by $f^{\xi}=f^{\xi}_{\rm ex}$ and $k_c=k_{0c}$, respectively. It follows that, with a density-dependent effective force, such an expansion contains additional terms which are, for the parametrization used here, of the same order as the effective range term. This simply demonstrates that for reproducing the pairing gap, the effective interaction, even at very low densities, need not necessarily coincide with the bare *NN* interaction, as was discussed by Migdal many years ago.[9]

At very low densities, at $k_F\to 0$, to leading order from (5) we obtain

$$\Delta = c\epsilon_F \exp\left(\frac{\pi}{2k_F a_{nn}}\right), \quad a_{nn}<0\,. \tag{9}$$

This expression agrees with the results of Ref. 10 based on a general analysis of the gap equation at low densities when $k_F|a_{nn}|\ll 1$. But we should stress that (9) is valid only in the weak-coupling regime corresponding to negative a_{nn}. In the opposite case, the gap in the dilute limit has to be found in a different way.

At $f^{\xi}_{\rm ex}>f^{\xi}_{\rm cr}$, it follows from (9) and (4) that at low densities the pairing gap is exponentially small and eventually $\Delta(k_F\to 0)=0$. Such a weak pairing regime with Cooper pairs forming in a spin singlet $l=0$ state exists up to the critical point at which the attraction becomes strong enough to change the sign of the scattering length. Then the strong pairing regime sets in, and Δ should be determined directly from the combined solution of Eqs. (3) and (6). In the dilute systems, ϵ_F plays the role of the chemical potential μ. It is defined by $\mu=\epsilon_F(k_F)+U(k_F)$, where $U(k_F)$ is the Hartree–Fock mean field at the Fermi surface, which is negligible for a fermion gas. At the critical point, μ becomes negative, and a bound state of a single pair of nucleons with the binding energy $\epsilon_b=2\mu$ $(=-\hbar^2/ma^2_{nn})$ becomes possible.[11,12] This can be easily seen from the gap equation (3) written in the form

$$\left(\frac{k^2}{m}-2\mu\right)\phi_k = -\,\mathrm{sgn}(\epsilon_k-\mu)\sqrt{1-\phi_k^2}\int_{k'\leqslant k_c}\frac{d\mathbf{k}'}{(2\pi)^3}F^{\xi}\phi_{k'}\,, \tag{10}$$

where we have introduced the functions $\phi_k=\Delta/\sqrt{(\epsilon_k-\mu)^2+\Delta^2}$ and replaced ϵ_F by μ. In the strong coupling regime $\mu<0$, and in the dilute limit, when $\phi_k^2\ll 1$, Eq. (10) reduces to the Schrödinger equation for a single bound pair where 2μ plays the role of the eigenvalue. At low densities in this regime, Δ can be found from (6). In the leading order we get

$$\Delta = \frac{\hbar^2}{m}\left(\frac{2\pi\rho}{a_{nn}}\right)^{1/2}, \quad a_{nn}>0\,. \tag{11}$$

It follows that, in the dilute case, the energy needed to break apart a condensed pair goes smoothly from 2Δ to $2\mu=\epsilon_b$ as a function of the coupling strength as the regime changes from weak to strong pairing. But as seen from (9) and (11), the behavior of Δ at

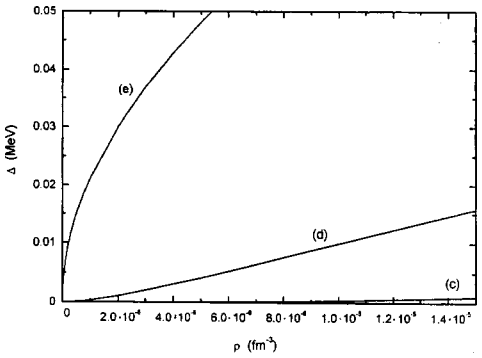

FIG. 2. Pairing gap Δ at very low densities. Curves (c)–(e) correspond to the parameter sets (c)–(e) of Eq. (2), respectively.

low densities is such that the derivative $d\Delta/d\rho$ at $\rho\to 0$ as a function of $f^{\xi}_{\rm ex}$ exhibits a discontinuity from 0 to ∞. This is illustrated in Fig. 2, where we have plotted $\Delta(\rho)$ at very low densities for the sets (c)–(e) of Eq. (2), which embrace both regimes. We note also that the transition between the two regimes is formally reflected by the fact that the analytical expressions (9) and (11) give a pure imaginary gap at the critical point, where the scattering length changes sign.

When the Fermi momentum k_F approaches from below the upper critical point, where the pairing gap closes, Δ becomes exponentially small.[10] In weak coupling, Δ is also exponentially small at low densities. It is noteworthy that in both these cases, for any given interaction, the gap can be calculated directly from (4) through the phase shifts. Such a model-independent result follows from the fact that the gap equation, written in the form similar to that of Eq. (10), at $\phi_k^2 \ll 1$ becomes equivalent to the Schrödinger equation, and the gap closes exactly at the points where the phase shift passes zero, i.e., where the integral in the right-hand side of this equation vanishes. As an illustration, we show in Fig. 1 by the dotted line the values of $\Delta(k_F)$ obtained from (4) using the ''experimental'' nn phase shifts, without electromagnetic effects.[1)] It is seen that Δ obtained this way closely follows the solution of the gap equation with the CD–Bonn potential[7] at low densities. The nn phase shift passes through zero at the relative momentum $k=1.71$ fm^{-1}, and the gap should vanish at the corresponding Fermi momentum. Unfortunately, the solutions for Δ are given in Ref. 7 only in the region up to $k_F=1.4$ fm^{-1}.

For symmetric nuclear matter, with our local functional the energy per particle is

$$\frac{E}{A}(x)=\frac{2}{\rho_0 x}\int_{k\leqslant k_c}\frac{d\mathbf{k}}{(2\pi)^3}\frac{\hbar^2k^2}{2m}n_k(x)+\frac{1}{3}\epsilon_{0F}a_+^{\nu}f_+^{\nu}(x)x+\frac{3\Delta^2(x)}{2f^{\xi}(x)x\epsilon_{0F}}, \tag{12}$$

where $f_+^{\nu}(x)=(1-h_{1+}^{\nu}x)/(1+h_{2+}^{\nu}x)$. Numerically, $a_+^{\nu}=-6.422$, $h_{1+}^{\nu}=0.163$, and $h_{2+}^{\nu}=0.724$.[4] The ''particle–hole'' term $\propto f_+^{\nu}$ vanishes in the dilute limit linearly in the density. The chemical potential is

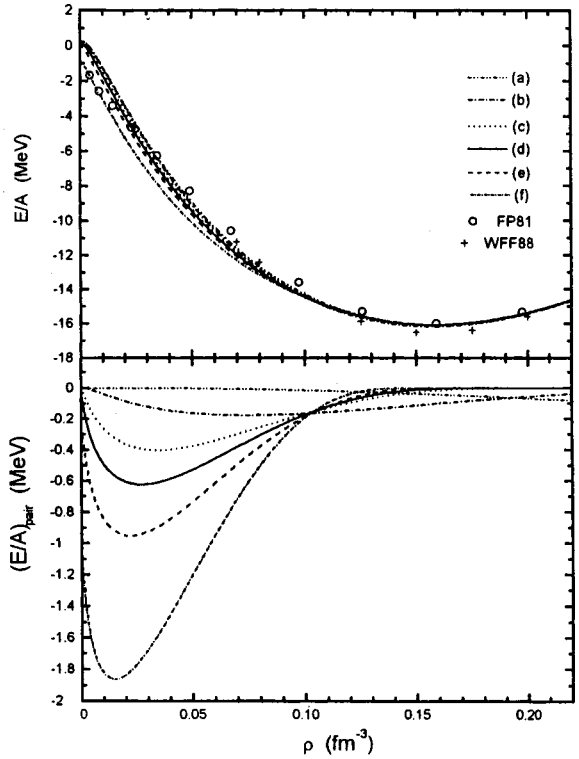

FIG. 3. Energy per nucleon E/A (top) and pairing contribution to E/A (bottom) in symmetric nuclear matter. Curves (a)–(e) are calculated using Eq. (12) and correspond to the strength parameters (a)–(e) of Eq. (2), respectively. The unfilled circles and crosses are the calculations of Refs. 13 and 14, respectively, for the UV14 plus TNI model.

$$\mu(x)=\epsilon_F(x)+\frac{1}{3}\epsilon_{0F}a_+^{\nu}[f_+^{\nu\prime}(x)x^2+2f_+^{\nu}(x)x]+\frac{3f^{\xi\prime}(x)}{2f^{\xi 2}(x)}\frac{\Delta^2(x)}{\epsilon_{0F}}, \tag{13}$$

where the prime denotes a derivative with respect to x, and $\epsilon_F(x)$ and $\Delta(x)$ are determined from (3) and (6). The last two terms in (13), even in the strong-pairing regime, vanish in the dilute limit at least as fast as x^q if $q<1$ or linearly in x if $q\geqslant 1$. Thus, we see again that, for strong coupling, one has in leading order $\mu=\epsilon_F=\epsilon_b/2<0$.

The calculated energy per nucleon as a function of the isoscalar density ρ is shown in the upper panel in Fig. 3 together with the results of the nuclear matter calculations[13,14] for the UV14 plus TNI model. It is seen that DF3 gives qualitatively reasonable description of the energy per particle for nuclear matter and that pairing could contribute noticeably to the binding energy, especially at lower densities. In the lower panel in Fig. 3 we have plotted the pairing energy per nucleon, $(E/A)_{\rm pair}$, obtained by subtracting from (12) the corresponding value of E/A at $\Delta=0$. The pairing contribution increases, as expected, when $f_{\rm ex}^{\xi}$ becomes gradually more attractive, with a shift to lower densities. For the sets (e) and (f) the attraction is strong, $f_{\rm ex}^{\xi}<f_{\rm cr}^{\xi}$. In these cases a nonvanishing binding energy in the dilute limit is solely due to Bose–Einstein condensation of the bound pairs,

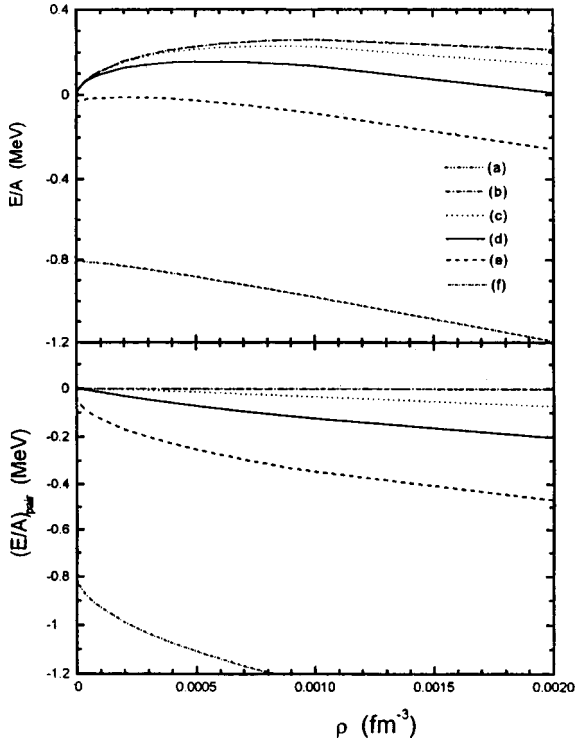

FIG. 4. Energy per nucleon E/A (top) and pairing contribution to E/A (bottom) for symmetric nuclear matter at low densities. The notation is the same as in Fig. 3.

the spin-zero bosons, when all three quantities μ, E/A, and $(E/A)_{\text{pair}}$ reach the same value $\epsilon_b/2=\hbar^2/2ma_{nn}^2$ ($\epsilon_b=-0.0646$ and -1.616 MeV for the sets (e) and (f), respectively). This is illustrated in Fig. 4, where we have plotted E/A and $(E/A)_{\text{pair}}$ as functions of ρ at very low densities.

In conclusion, we have considered nuclear matter with *s*-wave pairing within the LEDF framework and demonstrated some results, including extrapolation to the dilute limit, with a few possible parameter sets of the pairing force deduced from experimental data for finite nuclei. At low densities, in the $T=0$ case of symmetric $N=Z$ matter, the ${}^3S_1-{}^3D_1$ pairing, leading to the formation of a Bose deuteron gas, is more important,[15] since the $n-p$ force is more attractive than in the $p-p$ or $n-n$ pairing channels. Thus, our approach, with the ${}^1S_0$ pairing only, would be more appropriate for an asymmetric $N\neq Z$ case and for pure neutron systems. From this point of view the best choice for the LEDF calculations seems to be the pairing force with set (d) of Eq. (2), since it gives a singlet scattering length $a_{nn}\approx-17.2$ fm, which corresponds to a virtual state at $\approx$140 keV known experimentally. As is seen in Fig. 1, for this choice the behavior of Δ at low densities agrees well with calculations based on realistic NN forces. At higher densities, however, our predictions for Δ with the set (d) go much higher, reaching a maximum of $\approx$4.84 MeV at $k_F\approx0.92$ fm^{-1}, while the calculations of Ref. 7 give a maximum of about 3 MeV at $k_F\approx0.82$ fm^{-1}. With a bare NN interaction, if one assumes charge indepen-

dence and that $m_n = m_p$ in the free single-particle energies, the pairing gap would be, at a given k_F, exactly the same both in symmetric nuclear matter and in neutron matter. As was shown in Refs. 16 and 17, if one includes medium effects in the effective pairing interaction, Δ in neutron matter would be reduced substantially, to values of the order of 1 MeV at the most. Whether such a mechanism works in the same direction for symmetric nuclear matter is still an open question. With a smaller gap compared, for instance, to the one obtained with the Gogny D1 force, which is also shown in Fig. 1, it would be difficult to explain the observed nuclear pairing properties. Calculation with the preferred set (d) of Eq. (2) leads to a larger pairing energy in nuclear matter than the Gogny force, but in finite nuclei there is a compensation due to the repulsive gradient term. The force (1) contains dependence on the isoscalar density only, since we have analyzed the existing data on separation energies and charge radii for finite nuclei with a relatively small asymmetry $(N-Z)/A \leqslant 0.25$. An extrapolation to neutron matter with such a simple force would give a larger pairing gap than for nuclear matter. This suggests that some additional dependence on the isovector density $\rho_n - \rho_p$ should be present in the effective pairing interaction. We are planning a test of this possibility in a future study.

The author thanks S. T. Belyaev, V. A. Khodel, E. E. Saperstein, S. V. Tolokonnikov, and D. Zawischa for valuable discussions. This work was partially supported by the Deutsche Forschungsgemeinschaft and by the Russian Fund for Fundamental Research, Project 98-02-16979.

[1)]We thank Rupert Machleidt for providing us with these *nn* phase shifts.

[1] N. Tajima, P. Bonche, H. Flocard *et al.*, Nucl. Phys. A **551**, 434 (1993).
[2] S. A. Fayans and D. Zawischa, Phys. Lett. B **383**, 19 (1996).
[3] S. A. Fayans, S. V. Tolokonnikov, E. L. Trykov, and D. Zawischa, JETP Lett. **68**, 276 (1998); Noise Control Eng. J. **111 A**, 823 (1998).
[4] I. N. Borzov, S. A. Fayans, E. Krömer, and D. Zawischa, Z. Phys. A **355**, 117 (1996).
[5] S. T. Belyaev, A. V. Smirnov, S. V. Tolokonnikov, and S. A. Fayans, Yad. Fiz. **45**, 1263 (1987) [Sov. J. Nucl. Phys. **45**, 783 (1987).
[6] H. Esbensen, G. F. Bertsch, and K. Hencken, Phys. Rev. C **56**, 3054 (1997).
[7] Ø. Elgarøy and M. Hjorth-Jensen, Phys. Rev. C **57**, 1174 (1998).
[8] H. Kucharek, P. Ring, P. Shuck *et al.*, Phys. Lett. B **216**, 249 (1989).
[9] A. B. Migdal, *Theory of Finite Fermi Systems and Applications to Atomic Nuclei*, Interscience, New York, 1967.
[10] V. A. Khodel, V. V. Khodel, and J. W. Clark, Nucl. Phys. A **598**, 390 (1996).
[11] L. V. Keldysh and A. N. Kozlov, Zh. Éksp. Teor. Fiz. **54**, 978 (1968) [Sov. Phys. JETP **27**, 521 (1968)].
[12] P. Nozières and S. Schmitt-Rink, J. Low Temp. Phys. **59**, 195 (1985).
[13] B. Friedman and V. R. Pandharipande, Nucl. Phys. A **361**, 502 (1981).
[14] R. B. Wiringa, V. Fiks and A. Fabrocini, Phys. Rev. C **38**, 1010 (1988).
[15] M. Baldo, U. Lombardo, and P. Schuck, Phys. Rev. C **52**, 975 (1995).
[16] J. Wambach, T. L. Ainsworth, and D. Pines, Nucl. Phys. A **555**, 128 (1993).
[17] H.-J. Schulze, J. Cugnon, A. Lejeune *et al.*, Phys. Lett. B **375**, 1 (1996).

Published in English in the original Russian journal. Edited by Steve Torstveit.

Discovery of a narrow resonance state of the system K_SK_S at mass 1520 MeV

B. P. Barkov, V. V. Vladimirskiĭ, V. K. Grigor'ev, O. N. Erofeeva, Yu. V. Katinov, I. Ya. Korol'kov, V. I. Lisin, V. N. Luzin, V. N. Nozdrachev, V. V. Sokolovskiĭ,*) G. D. Tikhomirov, S. A. Uzunyan, and Yu. P. Shkurenko,

Institute of Theoretical and Experimental Physics, 117259 Moscow, Russia

I. A. Gridnev

Moscow Engineering Physics Institute, 141700 Dolgoprudnyĭ, Moscow Region, Russia

(Submitted 16 July 1999)
Pis'ma Zh. Éksp. Teor. Fiz. **70**, No. 4, 242–246 (25 August 1999)

Data are presented which indicate the existence of a previously unknown narrow resonance near mass 1520 MeV, discovered while analyzing the system K_SK_S. The data were obtained at ITEP using the 6-m magnetic spectrometer in a beam of 40-GeV negative particles. The resonance is observed in π^-p and K^-p interactions with a total statistical confidence of not less than 5 standard deviations. The width of this state is comparable to the mass resolution of the spectrometer (~ 5 MeV). The mass is 1521.5 ± 2.5 MeV. Estimates of the product $\sigma \cdot \mathrm{BR}(K_SK_S)$ give ~ 5.0 nb in π^-p interactions and ~ 250 nb in K^-p interactions. From the fact that the production cross section of this resonance in the K^- beam is approximately 50 times greater than the production cross section in the π^- beam, it can be concluded that this new state belongs to a system of mesons with hidden strangeness. © *1999 American Institute of Physics.* [S0021-3640(99)00316-3]

PACS numbers: 13.85.Ni, 13.85.Hd, 14.40.Aq

One of the currently central problems in modern elementary-particle physics is the search for exotic states. Exotic states are particles whose properties do not fit within the predictions of the elementary quark model relative to their quantum numbers and the ratios between various decay channels. Narrow decay widths can also be a manifestation of the exotic particle properties.

In the present letter we continue to report the results of an investigation of pair production of K_S mesons on the basis of the experimental data obtained at the ITEP with the 6-m spectrometer in a 40-GeV beam of negative particles. Here we present data indicating the existence of a narrow (width of the same order of magnitude as the mass resolution of the spectrometer) resonance near the mass 1520 MeV, discovered during an analysis of the K_SK_S system. The data were obtained during sessions in the period 1986–1989. A detailed description of the apparatus and the results of investigations of the K_SK_S system on the spectrometer at the ITEP is contained in Refs. 1–8. Here we note

two properties of the spectrometer that are important for the present investigation: For an energy of a system of two K_S mesons of the order of 1.5 GeV, the detection efficiency of such a system is not less than 50%, and the mass measurement accuracy is not worse than 5 MeV.

A beam of negative particles in channel 2A of the U-70 accelerator, where the spectrometer was installed, at the Institute of High-Energy Physics (Protvino) contains π^- ($\sim$95%), K^- mesons ($\sim$4.0%), and antiprotons. The π^- and K^- mesons in the beam are discriminated using differential (K^-) and threshold (π^-) Cherenkov counters. The corresponding signals are recorded together with the detected events and simultaneously influence the operation of the trigger. When the beam particle is a π^- meson, the trigger is tuned to select the reaction

$$\pi^- p \to K_S K_S n. \tag{1}$$

For this, a liquid-hydrogen target is surrounded on all sides, except at the opening through which the beam particles reach the target, with scintillation counters interlaid with lead converters. The counters are connected in anticoincidence. Therefore, those beam interactions with the target material which produce charged particles and γ rays are excluded. The detected events include events (amounting to $<$20%) in which a baryon and one or several pions are produced instead of a neutron at the bottom vertex:

$$\pi^- p \to K_S K_S (n\pi^0, \ldots, p\pi^-, \ldots). \tag{2}$$

These events are detected on account of the nonideality of the trigger system.

If the beam particle is a K^- meson, then when the spectrometer detects two fast K_S mesons at the bottom vertex of the reaction, on account of the law of conservation of strangeness, a hyperon must be produced, the decay products of which include charged particles or γ rays or both together:

$$K^- p \to K_S K_S (\Lambda, Y^*, \ldots). \tag{3}$$

For this reason, for detecting reactions involving the production of a system of two K_S mesons in a K^- beam, the signals from the counters surrounding the target were not fed to a trigger but instead were stored in a computer together with the rest of the information about the event. The charged particles and γ rays moving in the forward direction were suppressed. Together with the events of the reaction (3), cases with two K_S mesons could arise as a result of the production of three K^0 mesons, one of which was not detected by the spectrometer. But, as we showed in Ref. 4, the fraction of such events is negligibly small.

Investigating the behavior of the $K_S K_S$ system near 1.5 GeV, we could not ignore a characteristic feature in the spectrum of the invariant mass of a pair of K_S mesons — a narrow peak at $\sim$1520 MeV, systematically appearing in all exposures. This peak is observed in the effective-mass distributions constructed for a system of two K_S mesons for $\pi^- p$ and $K^- p$ interactions (Fig. 1). It is characterized by a small width (more than an order of magnitude smaller than the width of the known $f_2'(1525)$ meson), comparable with the resolution of the 6-m spectrometer in the corresponding mass range of $K_S K_S$ ($\sim$5 MeV). For a $K_S K_S$ system produced in a π^- beam, data-quality cuts according to the missing mass squared $MM^2 > 0$ and transverse momentum squared $p_T^2 > 0.15$ GeV^2 were made (in this paper we use a system of units in which $c = 1$). The cut according to

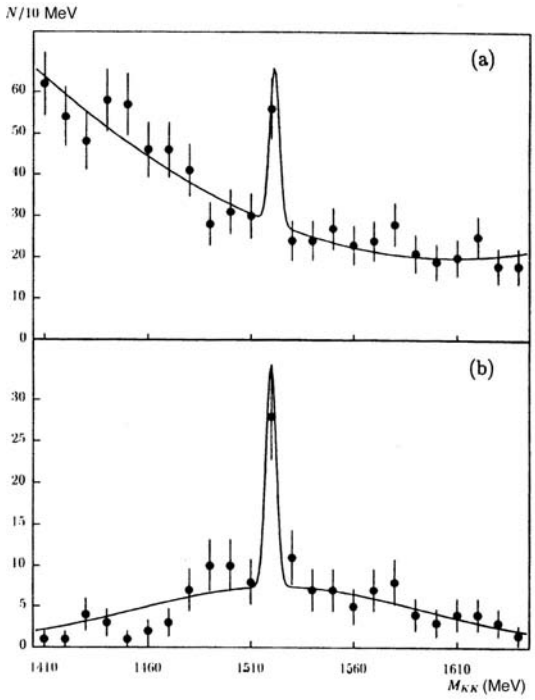

FIG. 1. a) Distribution of events produced in $\pi^- p$ and $K^- p$ interactions over the invariant mass of the $K_S K_S$ system, with a 10 MeV step and with $p_T^2 > 0.15$ GeV^2 and $MM^2 > 0$ GeV^2 cuts. The curve shows the result of the fitting. b) Distribution of events produced in the $K^- p$ interactions over the invariant mass of the $K_S K_S$ system, with a 10 MeV step and with a $MM^2 > 0$ GeV^2 cut. The curve shows the result of the fitting.

the transverse momentum squared is motivated by the need to suppress the contribution of single-pion exchange processes. For the $K^- p$ interaction, the distribution was constructed with the same missing mass squared cut but, in contrast to the distribution in Fig. 1a, without the p_T^2 cut.

A much larger number of cases of pair production of K_S mesons was detected in $\pi^- p$ interactions than in $K^- p$ interactions, but the signal/background ratio for the feature under discussion is approximately two times smaller. For this reason, a stricter cut according to the effective mass of the system of two charged π mesons from the decay of a K_S meson and a cut according to χ^2, which characterizes the quality of the fit of the momenta of the particles forming the ''fork'' to the intersection of the tracks and the equality of the effective mass and to the tabulated value of the K_S meson mass, were used for the events obtained in the π^- beam. We used similar cuts in Refs. 7 and 8 to improve the conditions for observing the narrow resonances $f_2(1786)$ and $a_2(1768)$. Such cuts decrease the statistical sample by $\sim 25\%$, but the signal/background ratio improves by a factor of 2. For events obtained in the K^- beam, such a procedure is ineffective, since in this case the signal/background ratio is quite high (~ 3) even without special data cuts.

A fit of both mass spectra was made. A Gaussian function was used to describe the observed narrow resonance. For events obtained in the π^- beam, the background is the decaying part of the peak from the $f_2(1270)$ and $a_2(1320)$ resonances. This background

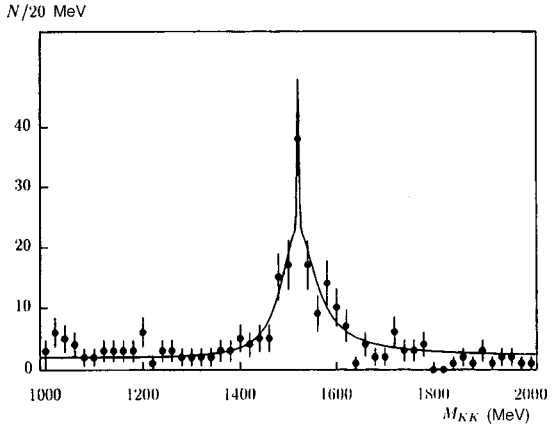

FIG. 2. Same as in Fig. 1b but with a 20 MeV step.

was described by a quadratic polynomial. In the case of $K^- p$ interactions the background for the resonance under discussion consists of $f_2'(1525)$ meson events plus a constant component. The mass distribution (Fig. 2) with a 20 MeV step demonstrates the presence of the f_2' meson in the experimental data under discussion. A relativistic Breit–Wigner function for $J=2$ was used to describe the $f_2'(1525)$ meson:

$$\frac{M_0^2\Gamma^2}{(M^2-M_0^2)^2+M_0^2\Gamma^2},$$

where

$$\Gamma=\Gamma_0(q/q_0)^{2J+1}D_2(q_0R)/D_2(qR), \quad D_2(x)=9+3x^2+x^4.$$

Here q is the momentum of the K_S mesons in the center of momentum frame of the f_2' meson, and $R=5$ GeV^{-1}. The fit was made by the maximum-likelihood method; the results are given in Table I. The fitting procedure is described in detail in Refs. 7 and 8. The new narrow resonance is designated by the symbol $X(1520)$. Table I gives the values of the decrease of χ^2 for the fit when the new narrow resonance is taken into account (after subtraction of the number of added parameters, of which there are three: intensity, mass, and width). The mass, the estimated width of the X resonance, the number of events occurring at it, and the numbers of f_2' meson and background events are also given. In the figures, the curves show the results of the fitting.

TABLE I.

Beam	$\Delta\chi^2-3$	M_X, MeV	δ_X, MeV	N_X	$N_{f_2'}$	N_{BG}
K^-	18.3	1520.3±1.8	<5.0	19	90	73
π^-	37.4	1522.6±1.6	<5.0	28	–	480

As one can see from Table I, the masses of the narrow resonance coincide to within the experimental errors. The errors given are the statistical errors. The systematic errors are two to three times smaller than the statistical errors. A naive estimate of the statistical significance, made on the basis of an analysis of the data presented in Fig. 1, gives at least 3.7 standard deviations in both cases. The estimate is made as follows: the error was determined as the square root of the number of events in the channel in which the effect is observed (57 in the first case and 28 in the second one). The background level was taken from the results of the fitting (29 and 8 events, respectively). The total statistical significance of the peak is not less than 5 standard deviations. An estimate based on analysis of the change in χ^2 gives a much higher confidence level.

The values obtained for the parameters of the resonance $f_2'(1525)$, which were free parameters in the fitting procedure, turned out to be close to the values given in the PDG tables:[9] mass $M_0 = 1513 \pm 10$ MeV, width $\Gamma_0 = 75 \pm 20$ MeV.

Since the resonance $X(1520)$ is observed in a system of two identical bosons, its angular momentum and parity must belong to the series $J^P = 0^+,\ 2^+,\ \ldots$.

The product $\sigma \cdot \mathrm{BR}(K_S K_S)$ for $X(1520)$ production is estimated to be ~ 5 nb for the π^- beam and ~ 250 nb for the K^- beam. It is natural to attribute such suppression of the production cross section in $\pi^- p$ interactions to the Okubo–Zweig–Iizuki selection rule. According to the data in the present letter and our earlier work,[3] the f_2' resonance in $\pi^- p$ interactions shows approximately the same suppression of the cross section. Therefore it can be asserted that the new resonance, just like f_2', belongs to a system of mesons with hidden strangeness. It follows from the distribution of the missing mass squared for events from the X resonance band in the case of $\pi^- p$ interactions that this resonance is produced primarily in the reaction (2). But the trigger used for the π^- beam suppresses this reaction severalfold. This circumstance was taken into account in the estimate of the production cross section of the X meson in the π^- beam, but this is impossible to do with sufficient accuracy.

Let us sum up the results of this work. A previously unknown resonance with mass 1521.5 ± 2.5 MeV and width < 5 MeV was discovered in $\pi^- p$ and $K^- p$ interactions in a system of two K_S mesons. The ratio of the cross sections of these two processes most likely indicates that this narrow resonance $X(1520)$ is due to mesons with hidden strangeness.

This work was supported by the Russian Fund for Fundamental Research (Grant No. 99–02–18540).

*)e-mail: sokolovsky@vitep5.itep.ru

[1] B. V. Bolonkin, O. N. Baloshin, A. M. Blagorodov *et al.*, ITÉF Preprint No. 86 [in Russian], Institute of Theoretical and Experimental Physics, Moscow (1973).
[2] B. V. Bolonkin, V. V. Vladimirskiĭ, A. P. Grishin *et al.*, ITÉF Preprint No. 154 [in Russian], Institute of Theoretical and Experimental Physics, Moscow (1973).
[3] B. V. Bolonkin, S. K. Bloshenko, V. V. Vladimirskiĭ *et al.*, Yad. Fiz. **43**, 1211 (1986) [Sov. J. Nucl. Phys. **43**, 776 (1986)].
[4] B. V. Bolonkin, S. K. Bloshenko, V. V. Vladimirskiĭ *et al.*, Yad. Fiz. **46**, 799 (1987) [Sov. J. Nucl. Phys. **46**, 451 (1987)].
[5] B. V. Bolonkin, S. K. Bloshenko, V. V. Vladimirsky *et al.*, Nucl. Phys. B **309**, 426 (1988).

[6] V. K. Grigor'ev, O. N. Baloshin, B. P. Barkov *et al.*, Yad. Fiz. **59**, 2187 (1996) [Phys. At. Nucl. **59**, 2105 (1996)].
[7] B. P. Barkov, N. V. Batalova, V. V. Vladimirskiĭ *et al.*, JETP Lett. **68**, 764 (1998).
[8] V. K. Grigor'ev, O. N. Baloshin, B. P. Barkov *et al.*, Yad. Fiz. **62**, 513 (1999) [Phys. At. Nucl. **62**, 471 (1999)].
[9] Particle Data Group, Eur. Phys. J. C **3** (1998).

Translated by M. E. Alferieff

Total conversion of the polarization of electromagnetic waves during excitation of cyclotron polaritons in a two-dimensional electron system

V. V. Popov*) and T. V. Teperik
Saratov Division of the Institute of Radio Engineering and Electronics, Russian Academy of Sciences, 4010019 Saratov, Russia

(Submitted 1 July 1999)
Pis'ma Zh. Éksp. Teor. Fiz. **70**, No. 4, 247–252 (25 August 1999)

The reflection of an electromagnetic wave from a two-dimensional (2D) electron system in a magnetic field is studied. It is predicted that a p (s) polarized incident wave will be totally converted into a reflected wave with the orthogonal polarization when cyclotron polaritons are excited in the 2D system. For a high electron density in the 2D system, the effect remains very substantial in magnitude even in the presence of electron scattering. © *1999 American Institute of Physics.* [S0021-3640(99)00416-8]

PACS numbers: 41.20.Jb, 52.40.Db

The conversion of the polarization of an electromagnetic wave transmitted through a magnetoactive two-dimensional (2D) electron system is, as a rule, small,[1–3] because in this case the region of interaction of the wave with the polarization-active medium is small. However, polarization conversion can increase substantially (resonantly) when the external electromagnetic wave excites characteristic oscillations in the 2D system.

The resonant Faraday effect arising in a system of 2D electron disks as result of the excitation of edge magnetoplasmons was observed in Ref. 4. The results obtained in Ref. 4 show that the effect is several times stronger under magnetoplasma resonance conditions. At the same time, the power of the polarization-converted wave in the experiments of Ref. 4 remains comparatively low (less than 10% of the power of the incident wave). The smallness of the resonance effect in this case is most likely due to the mismatch of the distributions of the field of the external (uniform in the plane of the 2D system) electromagnetic wave and the field of nonuniform edge magnetoplasmons, as a result of which the excitation efficiency of the latter decreases substantially.

The resonant polarization conversion of an electromagnetic wave accompanying the excitation of uniform transverse plasma oscillations of electrons in a thin semiconductor film has been studied in Ref. 5. The magnitude of the effect is proportional to the small parameter d/λ, where d is the film thickness and λ is the wavelength of the electromagnetic wave. Naturally, this decreases the efficiency of resonant polarization conversion in thin layers.

The limitations due to the thickness of the electron layer, in principle, do not arise if the external electromagnetic wave excites characteristic oscillations due to the motion of

electrons in the plane of a uniform electron system. In Ref. 6 it is shown theoretically that when magnetoplasma polaritons are excited in a 2D electron system by an external electromagnetic wave in a frustrated total internal reflection (FTIR) geometry, almost complete conversion of the incident $p(s)$ polarized wave into a wave with $s(p)$ polarization is possible. However, according to Ref. 6, total polarization conversion occurs only in the limit of weak coupling of the field of the external wave with the 2D electron system. In this case, two resonance conditions, corresponding, respectively, to excitation of magnetoplasma polaritons and cyclotron oscillations in the 2D electron layer, must be satisfied at the same time. It is obvious that these conditions together lead to very stringent requirements on the parameters of a possible experiment on the observation of total polarization conversion. Moreover, dissipation of the energy of an electromagnetic wave due to electron scattering in a real 2D system can lead to virtually complete destruction of the weak coupling of the external wave with the oscillations of a 2D electronic plasma in the FTIR geometry.

In the present letter the phenomenon of resonant polarization conversion of an electromagnetic wave which excites cyclotron polaritons[7] in a 2D electron system is investigated theoretically. Since cyclotron polaritons are radiating oscillations, they can be excited by the incidence of an external electromagnetic wave directly on the surface of a 2D system without the use of any additional devices (for example, structures with FTIR). In contrast to the FTIR geometry, cyclotron polaritons in a 2D system are strongly coupled with the external incident wave, greatly expanding the possibilities of observing the effects considered below.

In the structure considered here, the 2D electron layer lies in the $x-y$ plane at the interface of two media with permittivities ε_1 and ε_2. We shall assume that a static magnetic field $\mathbf{H}_0$ is directed along the z axis from medium 2 into medium 1. Let an external uniform p-polarized electromagnetic plane wave, so that the electric field vector of the wave lies in the plane of incidence ($x-z$ plane), be incident from medium 1 on the interface between media 1 and 2 at an angle θ to the z axis.

We introduce the coefficients of conversion of the power of the incident wave as ratios of the components of the energy flux vectors normal to the plane of the 2D system:

$$R_{pp}=\frac{P_{1z}^{(p)}}{P_{0z}^{(p)}}, \quad R_{sp}=\frac{P_{1z}^{(s)}}{P_{0z}^{(p)}}, \quad T_{pp}=\frac{P_{2z}^{(p)}}{P_{0z}^{(p)}}, \quad T_{sp}=\frac{P_{2z}^{(s)}}{P_{0z}^{(p)}}, \tag{1}$$

where the subscripts 0, 1, and 2 refer to the incident, reflected, and transmitted waves, respectively, and the superscripts p and s correspond to waves with p and s polarization (in the latter case the electric field vector of the wave is perpendicular to the plane of incidence). It is obvious that the quantities R_{sp} and T_{sp} are the polarization conversion coefficients for the wave.

To calculate the energy fluxes in the transmitted and reflected waves it is necessary to solve Maxwell's equation in media 1 and 2 with boundary conditions at the interface of the media that take into account the response of the magnetoactive 2D electronic plasma. Since this procedure is very cumbersome and at the same time quite standard, we present immediately the final result:

$$R_{pp}=\frac{1}{A^2}\left|(K_{0z}+K_{2z}+4\pi\sigma_\perp/c)(K_{0z}\varepsilon_2-K_{2z}\varepsilon_1+K_{0z}K_{2z}4\pi\sigma_\perp/c)\right.$$
$$\left.+K_{0z}K_{2z}(4\pi\sigma_\times/c)^2\right|^2,$$
$$R_{sp}=\frac{4\varepsilon_2K_{z0}^2}{A^2}\left|K_{2z}4\pi\sigma_\times/c\right|^2,$$
$$T_{pp}=\frac{4\varepsilon_1\varepsilon_2K_{z0}}{A^2}\,\mathrm{Re}(K_{2z})\left|K_{2z}+K_{0z}+4\pi\sigma_\perp/c\right|^2,$$
$$T_{sp}=\frac{4\varepsilon_1K_{z0}}{A^2}\,\mathrm{Re}(K_{2z})\left|K_{2z}4\pi\sigma_\times/c\right|^2, \tag{2}$$

where $A=\left|(K_{0z}+K_{2z}+4\pi\sigma_\perp/c)(K_{0z}\varepsilon_2+K_{2z}\varepsilon_1+K_{0z}K_{2z}4\pi\sigma_\perp/c)+K_{0z}K_{2z}\times(4\pi\sigma_\times/c)^2\right|$, c is the speed of light, and K_{0z} and K_{2z} are the components of the dimensionless wave vector normal to the plane of the 2D system for the incident and transmitted waves, respectively; they are given by the expressions

$$K_{0z}=\sqrt{\varepsilon_1}\,\cos\theta,\quad K_{2z}=\sqrt{\varepsilon_2-\varepsilon_1\sin^2\theta}. \tag{3}$$

The normal component K_{1z} of the wave vector of the reflected wave does not appear explicitly in the final expressions (2) because the equality $K_{1z}=-K_{0z}$ is used. The components of the conductivity tensor of a 2D electronic plasma in a magnetic field in the Drude model are given by the expressions

$$\sigma_\perp=\sigma_0\frac{1-i\omega\tau}{(\omega_c\tau)^2+(1-i\omega\tau)^2},\quad \sigma_\times=-\sigma_0\frac{\omega_c\tau}{(\omega_c\tau)^2+(1-i\omega\tau)^2}, \tag{4}$$

where ω is the angular frequency of the wave, $\omega_c=|e|H_0/m^*c$ is the cyclotron frequency, $\sigma_0=e^2N_s\tau/m^*$ is the dc conductivity of the 2D electron system in the absence of an external magnetic field, and e, m^*, N_s, and τ are, respectively, the charge, effective mass, surface density, and phenomenological relaxation time of the electron momentum in the 2D system.

As is well known,[7] the magnitudes of the wave vector of cyclotron polaritons in the plane of a 2D system lie in the range $0<K_x<\sqrt{\max(\varepsilon_1,\varepsilon_2)}$. An external electromagnetic wave incident at an angle θ from medium 1 excites in the 2D system forced oscillations with longitudinal wave numbers $K_x=\sqrt{\varepsilon_1}\sin\theta$. In order to be able to investigate the entire range of variation of the wave vector of cyclotron polaritons, we assume $\varepsilon_1>\varepsilon_2$. It is obvious that for $\theta\geqslant\theta_R$, where $\theta_R=\sin^{-1}\sqrt{\varepsilon_2/\varepsilon_1}$, the regime of total internal reflection of the wave from the interface obtains. As follows from Ref. 3, in this case the quantity K_{2z} assumes imaginary values.

Most interesting is the behavior of the polarization conversion coefficient R_{sp} of the wave. The corresponding curves for the case where there is no electron scattering in the 2D system $(1/\tau=0)$are presented in Fig. 1. The remaining parameters used in the calculations are characteristic for GaAs/AlGaAs heterostructures with a 2D electron gas. The choice of values of the static magnetic field that correspond to the results presented is dictated by the condition of resonant excitation of cyclotron polaritons $\omega\simeq\omega_c$.[7] It follows from Fig. 1 that R_{sp} increases substantially in the total internal reflection regime and

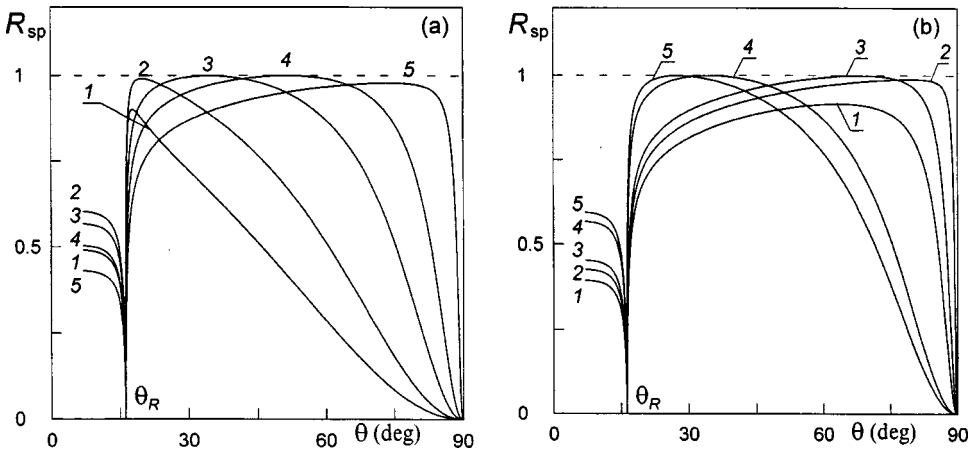

FIG. 1. Coefficient of conversion of the polarization in the reflected wave versus the angle of incidence: a) $N_s=2\times10^{12}$ cm^{-2}; H_0 (kG): 44 (*1*), 45 (*2*), 46 (*3*), 46.5 (*4*), 47 (*5*), b) $H_0=46$ kG; $N_s(10^{12}$ cm$^{-2})$: 0.8 (*1*), 0.9 (*2*), 1 (*3*), 2 (*4*), 3 (*5*); $\omega/2\pi c=60$ cm^{-1}, $\varepsilon_1=12.8$, $\varepsilon_2=1$, $m^*=0.07m_0$, where m_0 is the free-electron mass.

reaches 1 at a certain angle of incidence $\theta>\theta_R$. For comparison, we indicate that far from resonant values of the static magnetic field the calculations give a polarization conversion coefficient less than 10^{-3} for any angle of incidence of the wave. At resonance (Fig. 1) the extremely high polarization conversion coefficient remains in a quite wide range of variation of the angle of incidence of the wave. This is explained by the comparatively weak dependence of frequency of the cyclotron polaritons on the longitudinal wave number $K_x=\sqrt{\varepsilon_1}\sin\theta$.[7] It is obvious that for total conversion of the polarization one has $R_{pp}=0$. Calculations show that at the point $R_{pp}=0$ ($R_{sp}=1$) the amplitudes of the components of the field of the reflected wave with p polarization pass through zero with their phase changing by π.

As is evident from Fig. 1, polarization conversion is absent for $\theta=\theta_R$. Formally, this is because for $\theta=\theta_R$ the transverse component K_{2z} of the wave vector vanishes [see expression (3)] and therefore Eqs. (2) give $R_{sp}=T_{sp}=0$. The physical explanation of this fact is that for $K_{2z}=0$ the electromagnetic field in medium 2 is a uniform (p-polarized) plane wave propagating in the x direction with wave number $K_x=\sqrt{\varepsilon_2}$. It is obvious that the electric field vector of this wave does not have a component that is parallel to the plane of the 2D system. Hence it follows that for $\theta=\theta_R$ the total electric field and currents in the plane of the 2D system are zero and therefore the 2D system does not affect the wave reflection process.

In Fig. 2 the dark tone indicates $\omega-\theta$ regions win which the polarization conversion coefficient $R_{sp}>0.99$ for various values of the surface electron density in the 2D system. The figure also shows the dispersion curves $\omega[K_x(\theta)]$ of the cyclotron polaritons for the same values of the surface density. For a low electron density efficient polarization conversion occurs near the cyclotron polariton frequency ($\omega\simeq\omega_c$) for any angle of incidence of the wave. This corresponds to the case of weak coupling, when the external wave induces comparatively low currents in the 2D system. As the electron density increases, the coupling of the external wave with the 2D system increases, and the

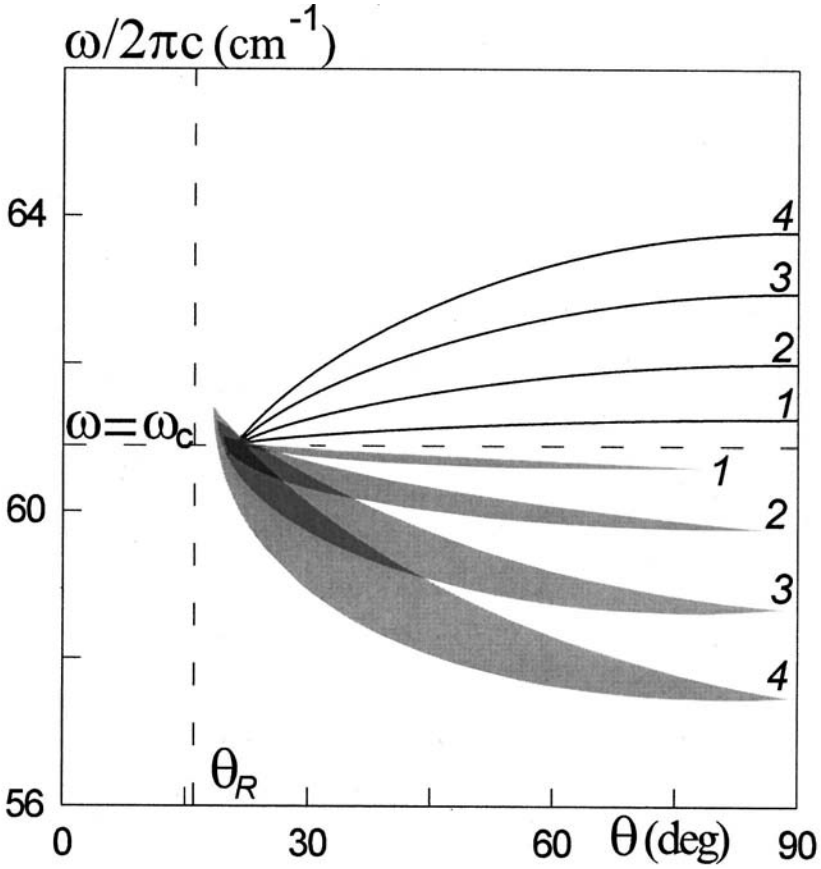

FIG. 2. Regions of the parameters $\omega-\theta$ with the highest polarization conversion efficiency and dispersion curves for cyclotron polaritons for $\varepsilon_1=12.8$, $\varepsilon_2=1$, $H_0=46$ kG, and N_s (10^{12} cm^{-2}): 0.2 (*1*), 1 (*2*), 2 (*3*), 3 (*4*).

frequency range in which efficient polarization conversion occurs increases. In this case, complete polarization conversion occurs at frequencies different from the characteristic oscillation frequencies of the 2D system.

The effect of electron scattering in the 2D system on the polarization conversion efficiency is demonstrated in Fig. 3. It is evident that a high conversion efficiency remains even in the presence of electron scattering if the electron density in the 2D system is high. At the same time, if the coupling of the external wave with the cyclotron oscillations in the 2D system is weak (low electron density), electron scattering suppresses the polarization conversion effect almost completely.

In conclusion, we note that the solution of the problem of the incidence of an *s*-polarized wave on a 2D electron system gives the same values for the polarization conversion coefficients ($R_{ps}=R_{sp}$) in the total internal reflection regime. This attests to a reciprocal character of the polarization conversion process for $\theta\geqslant\theta_R$.

We thank Yu. A. Kosevich for calling our attention to the problem of resonant

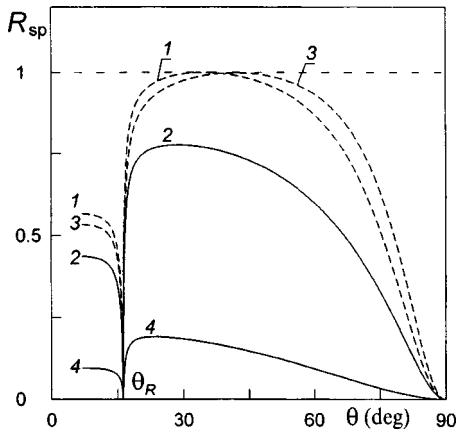

FIG. 3. Curves *1* and *3* correspond to the case when there is no electron scattering in the 2D system ($1/\tau = 0$); curves *2* and *4* correspond to $1/\tau = 10^{11}$ s^{-1}. Curves *1* and *2*: $N_s = 2\times10^{12}$ cm^{-2}, $H_0 = 46$ kG; curves *3* and *4*: $N_s = 2\times10^{11}$ cm^{-2}, $H_0 = 45.3$ kG. All other parameters are the same as in Fig. 1.

conversion of the polarization of electromagnetic radiation in 2D electron systems. This work was supported by the Federal Target Program ''State Support of Integration of Higher Education and Fundamental Science in the Years 1997–2000,'' Project 696.3.

*)e-mail: popov@ire.san.ru

[1] R. F. O'Connell and G. Wallace, Phys. Rev. B **26**, 2231 (1982).
[2] V. A. Volkov and S. A. Mikhalov, JETP Lett. **41**, 476 (1985).
[3] V. A. Volkov, D. V. Galchenko, L. A. Galchenkov *et al.* JETP Lett. **43**, 326 (1986).
[4] L. A. Galchenkov, I. M. Grodnenskiĭ, M. V. Kostovetskiĭ *et al.*, Fiz. Tekh. Poluprovodn. **22**, 1196 (1988) [Sov. Phys. Semicond. **22**, 757 (1988)].
[5] M. I. Bakunov and S. I. Zhukov, Pis'ma Zh. Tekh. Fiz. **16**, 1, 69 (1990) [Sov. Tech. Phys. Lett. **16**, 30 (1990)].
[6] Yu. A. Kosevich, Solid State Commun. **104**, 321 (1997).
[7] V. V. Popov, T. V. Teperik, and G. M. Tsymbalov, JETP Lett. **68**, 210 (1998).

Translated by M. E. Alferieff

Self-deflection of laser beams during holographic recording in photorefractive crystals

M. P. Petrov,*) A. P. Paugurt, and V. V. Bryksin
A. F. Ioffe Physicotechnical Institute, Russian Academy of Sciences, 194021 St. Petersburg, Russia

(Submitted 11 June 1999; resubmitted 12 July 1999)
Pis'ma Zh. Éksp. Teor. Fiz. **70**, No. 4, 253–256 (25 August 1999)

We have observed dynamic deflection of laser beams reflected from a crystal surface during recording of dynamic holograms in a photorefractive crystal. A theory describing the principal experimental facts is presented. The model takes into account the nonlinear interaction of space-charge waves. © *1999 American Institute of Physics.* [S0021-3640(99)00516-2]

PACS numbers: 42.70.Ln, 42.70.Nq, 42.40.Ht, 42.65.Hw

In photorefractive crystals,[1] an electric-field grating is formed when holograms are recorded, and this grating gives rise to a refractive-index grating as a result of the electrooptic effect as well as to elastic stress and strain gratings due to the piezoelectric effect. A periodic relief of the crystal surface, giving rise to diffraction of the recording (or reading) beams from the surface, can arise under certain conditions. Such diffraction has been observed in static[2] and dynamic[3] regimes. In the latter case the recording was done by an interference pattern oscillating around an average position, and the oscillations themselves arose because one of the recording beams was phase-modulated. A theoretical analysis of the surface relief during holographic recording is given in Refs. 4–6 for several specific situations. In the present letter we report a different effect: self-deflection of the writing beams from the crystal surface during the recording of a hologram in a photorefractive crystal. This effect is also due to space-charge fields of the holographic grating and the piezoelectric effect, but it is not related with the periodic relief of the surface and the diffraction of light by this relief. The self-deflection effect can be explained by the nonlinear interaction of a static grating of photoexcited carriers with the traveling wave of the space-charge field.

The experiment was performed as follows. An approximately cubic $Bi_{12}SiO_{20}$ (BSO) single crystal with 3 mm edges was chosen as the object of the investigations. The front face (parallel to the (110) crystallographic plane) was optically ground and polished, while the back face was worked with coarse emery cloth to minimize reflection from it, since preliminary experiments showed that the beams reflected from the back face give rise to additional gratings that make it difficult to interpret the experimental data. An electric field E_0 (Fig. 1) was applied to the side faces (along the [001] axis). The front face was illuminated with two beams from a Coherent DRSS-532-200 ($\lambda = 532$ nm) laser, one of which was phase-modulated (with frequency $\Omega = 2\pi f$ and amplitude

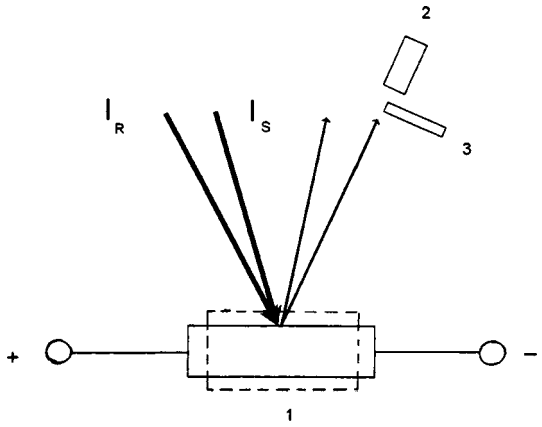

FIG. 1. Diagram of the experimental arrangement: *1* — crystal, *2* — photodetector, *3* — screen; I_S, I_R — beams recording a hologram. The dashed lines show the deformation of the crystal accompanying the application of a uniform electric field along the [001] axis.

θ). Measurements of the ac signal in the reflected beam were performed using two different variants for illumination of the photodetector. In the first case the reflected beam was incident completely on the photodetector, and the signal due to two-wave interaction as a result of diffraction by the surface relief of the sample could be detected as was done in Ref. 3. The signal due to small deflections of the beam cannot be detected here, since the aperture of the photodetector was several times greater than the beam cross section. In the second case, a screen covering approximately half the beam cross section was placed in front of the photodetector; this made it possible to detect oscillations of the position (deflection) of the beam or changes in its transverse cross section. In what follows, for simplicity we shall call the signals detected in the first case diffraction signals and those detected in the second case deflection signals. Figure 2 shows the dependence of the deflection and diffraction signals on the phase-modulation frequency for two spatial

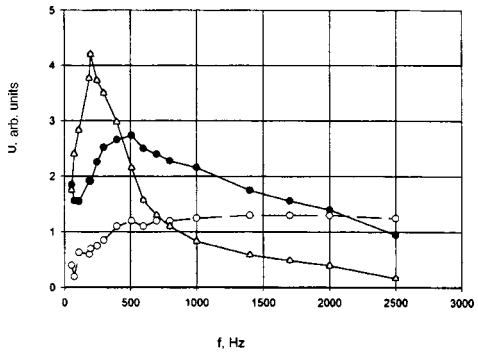

FIG. 2. Deflection and diffraction signals versus the phase-modulation frequency for two angles between the incident beams: ○ — frequency dependence of the diffraction signal for $\nu = 20\ \text{mm}^{-1}$, $E_0 = 10$ kV/cm; ● and Δ — frequency dependence of the deflection signals for $\nu = 20\ \text{mm}^{-1}$ and $\nu = 135\ \text{mm}^{-1}$, respectively ($E_0 = 10$ kV/cm).

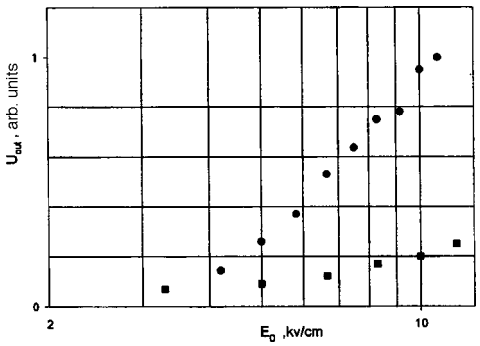

FIG. 3. Deflection signal (●, $\nu = 80$ mm^{-1}) and diffraction signal (■, $\nu = 20$ mm^{-1}) versus the external electric field. The deflection signal was measured at frequencies corresponding to resonance, and the diffraction signal was measured at $f = 1000$ Hz.

frequencies (ν) of the recorded gratings, i.e., for two angles between the incident beams. For other values of ν (120, 80, 40 mm^{-1}) the experimental data for the deflection signals have a form qualitatively similar to that presented in Fig. 2, but the position of the maximum and the absolute value of the signals depended on ν. We note that the deflection signals depend linearly on the photodetector–crystal distance, while no such dependence was observed for the diffraction signals. The diffraction signals could be observed only for comparatively low spatial frequencies, and they were not observed for $\nu = 135$ mm^{-1}.

Figure 3 shows the intensity of the detected signals versus the applied electric field. The dependence is quadratic for the deflection signal and and linear for the diffraction signal. Moreover, it was found that mechanical pressure applied along the [001] axis produces a linear shift of resonance frequencies as a function of pressure.

The theoretical interpretation is based on taking into account the nonlinearity of space-charge formation during the recording of holographic gratings in photorefractive crystals.[7] The traveling space-charge field grating, proportional to $\exp[i(kx-\Omega t)]$, interacts with the static photoexcited carrier grating, proportional to $\exp(-ikx)$, which leads (as a result of the multiplication in the expression[7] for the current density $j(x,t)$) to the appearance of a field $E_{sc} \sim \exp(-i\Omega t)$ which is uniform over the sample but oscillates in time. Here $k = 2\pi\nu$ is the wave number of the grating. The field E_{sc} gives rise via the piezoelectric effect to elastic displacement of the sample surface (in a direction normal to the surface), which is the reason for the shift (displacement) or deflection of the beam reflected from the surface. For uniform displacement of the crystal surface, the reflected beam will shift by an amount that depends on the displacement of the crystal surface and the angle of incidence. An exact calculation using the scheme of Ref. 7 but assuming that the crystal is powered by a current source and not a voltage source (as was done earlier) gives the following expression for the detected deflection signal:

$$U_{\text{out}} = c d_{14} E_{sc}, \tag{1}$$

where c is a certain coefficient that depends on the geometry of the experiment (the position of the screen, the photodetector–sample distance, the angle of incidence, and so on), $d_{14} = 40.5 \times 10^{-12}$ C/N is the piezoelectric coefficient,[8]

$$E_{sc} = E_0 m^2 d\,\theta f(\omega)\cos(\Omega t + \varphi), \tag{2}$$

m is the contrast of the interference pattern in the sample, φ is a phase that depends on the frequency, $\omega = \tau_M \Omega$ (τ_M is the Maxwellian relaxation time), $d = kL_0$ ($L_0 = \mu\tau E_0$ is the drift length of the carriers, μ is the mobility, and τ is the carrier lifetime),

$$f(\omega) = \omega\{(1+\omega^2/4)/[(1+\omega^2)(1+2\omega^2(1-d^2)+\omega^4(1+d^2)^2)]\}^{1/2}. \tag{3}$$

It follows from this expression that the frequency dependence of the output signal is of a resonant character, with the resonance frequency (for $d \gg 1$)

$$\Omega_r \approx 1/\tau_M d \approx (k\mu\tau\tau_M E_0)^{-1}. \tag{4}$$

It is well known[1] that for BSO the product $\mu\tau \approx (1-8)\times 10^{-11}$ m^2/V. Correspondingly, for $E_0 = 10^6$ V/m and $k = 2\times 10^5$ m^{-1} we have $d \approx 2-16$. The Maxwellian relaxation time τ_M depends on the illumination, and in our case $\tau_M \approx 10^{-3} - 10^{-4}$ s.

Comparing the formulas obtained and the experimental data shows good qualitative agreement between theory and experiment. The proposed theory explains, first and foremost, the fact that the beam is displaced over the aperture of the photodetector and the existence of a resonance (when the excitation frequency equals the characteristic frequency of the space-charge wave[7]). The theory agrees with the experimental dependences of the position of the resonance on the spatial frequency and with the quadratic dependence of the amplitude of the output signal on the external field ($E_0 d \sim E_0^2$). Moreover, the model proposed makes it easy to understand the reason for the shift in the resonance as a function of the pressure. The point is that when pressure is applied to the sample, an electric field appears as a result of the piezoelectric effect. This field adds to the external field, and the total field, which depends on the pressure, will appear in the expression for the resonance frequency (4). The proposed theory also explains the difference in the dependence of the magnitude of the output signal on the spatial frequency between the deflection signal [the signal increases with k) and the diffraction signal (which decreases with increasing k (Ref. 3)]. At the same time, the computed and observed values of the deflection signal amplitude differ from one another by one or two orders of magnitude and, moreover, the model of an absolute uniform field $E_{sc}(t)$ does not explain the experimentally observed dependence of the detected signal on the photodetector–crystal distance. In our opinion, this is because the field inside the crystal is nonuniform (specifically, because of near-electrode phenomena),[1] with a characteristic nonuniformity length much greater than the period of the holographic grating. In this case the induced field, which we calculated, and the deformation of the sample will also be nonuniform, and the output signal will be related not only with the displacement but also the angular deflection of the beam incident on the photodetector. In the case of angular deflection of the beam, the signal magnitude will depend on the crystal–photodetector distance, while the absolute value of the signal can be much greater than for displacement of the beam. On the whole, this agrees with experiment. For a nonuniform field, focusing and defocusing of a beam will also occur.

In conclusion, we note that in the present letter we reported the observation and give an explanation of a new effect in photorefractive crystals — dynamic deflection of beams reflected from a crystal during the recording of an oscillating interference pattern. This work was performed as part of a project of the Russian Fund for Fundamental Research (Grant No. 98-02-18254).

*)e-mail: mpetr@shuv.pti.spb.su

[1] M. P. Petrov, S. I. Stepanov, and A. V. Khomenko, *Photorefractive Crystals in Coherent Optical Systems* (Springer-Verlag, Heidelberg, 1991).
[2] A. M. Bliznetsov, M. P. Petrov, and A. V. Khomenko, Pis'ma Zh. Tekh. Fiz. **10**(9), 1094 (1984) [Sov. Tech. Phys. Lett. **10**(5), 463 (1984)].
[3] S. Stepanov, N. Korneev, A. Gerwens, and K. Buse, Appl. Phys. Lett. **72**, 879 (1998).
[4] S. M. Shandarov, Zh. Tekh. Fiz. **56**, 583 (1986) [Sov. Phys. Tech. Phys. **31**, 352 (1986)].
[5] S. M. Shandarov and B. M. Shandarov, Zh. Tekh. Fiz. **60**, 106 (1990) [Sov. Phys. Tech. Phys. **35**, 199 (1990)].
[6] S. M. Shandarov and N. I. Burimov, Izv. Vyssh. Uchebn. Zaved. Fiz. **9**, 75 (1997).
[7] V. V. Bryksin and M. P. Petrov, Fiz. Tverd. Tela (St. Petersburg) **40**, 1450 (1998) [Phys. Solid State **40**, 1317 (1998)].
[8] V. I. Chmyrev, L. A. Skorikov, and M. I. Subbotin, Neorg. Mater. **9**, 269 (1983).

Translated by M. E. Alferieff

Far-IR radiation of hot holes in germanium for mutually perpendicular directions of uniaxial pressure and electric field

V. N. Bondar and A. T. Dalakyan
Institute of Physics, Ukrainian National Academy of Sciences, 252650 Kiev, Ukraine

L. E. Vorob'ev and D. A. Firsov
St. Petersburg State University, 195251 St. Petersburg, Russia

V. N. Tulupenko*)
Donbass State Machine Building Academy, 343913 Kramatorsk, Ukraine

(Submitted 14 July 1999)
Pis'ma Zh. Éksp. Teor. Fiz. **70**, No. 4, 257–261 (25 August 1999)

The advantages of crossed directions of an electric field and uniaxial pressure over a parallel configuration for obtaining lasing ($\lambda \cong 100$ μm) in *p*-type germanium are substantiated. The results of the first experiments investigating far-IR emission for mutually perpendicular directions of the field and pressure are reported. The pressure dependences of the radiation intensity in various electric fields are explained by the different hole occupation of the states of an impurity center which are split by uniaxial pressure. © *1999 American Institute of Physics.* [S0021-3640(99)00616-7]

PACS numbers: 42.55.Px, 78.40.Fy, 42.72.Ai

ON THE POSSIBILITIES OF DEVELOPINGA GERMANIUM LASER FOR THE FAR-IR RANGE AT $T=77$ K

In the 1980s a series of active devices for the far-IR (FIR) range based on *p*-type germanium was developed.[1] The most powerful device was a laser operating on intersubband hole transitions in crossed electric (**E**) and magnetic (**B**) fields.[2] Unfortunately, these devices can operate efficiently only at liquid-helium and liquid-hydrogen temperatures, which limits their applications. For this reason, the development of FIR-range lasers operating at liquid-nitrogen and higher temperatures is a central problem in semiconductor physics. Lasing ($\lambda \approx 100$ μm) which was observed in Ref. 3 to arise in *p*-type germanium (!) for a parallel configuration of the electric field (EF, $E=1.5$–3 kV/cm) and uniaxial pressure (UP, $X \approx 7$–8 kbar for $\mathbf{E} \parallel \mathbf{X} \parallel [111]$) offers some hope for solving this problem. This conclusion can be drawn on the basis of a comparison of the single-pass optical path lengths in the active medium that are required for compensating the losses and for onset of lasing in a cavity, based on total internal reflection, for a laser operating on intersubband transitions in crossed electric and magnetic fields (l_{EB}) and for a laser under uniaxial compression[3] (l_{EX}): in the first case $l_{EB} \geqslant 80$–100 mm,[1] while in the second case $l_{EX} \leqslant 4$ mm.[3]

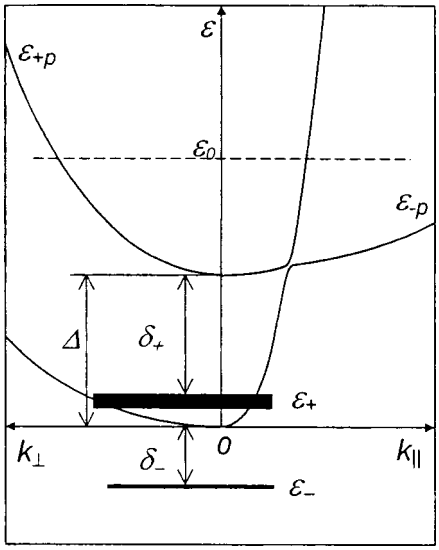

FIG. 1. Schematic representation of the structure of the valence band of uniaxially strained Ge (schematically) for pressures $X>X_{\rm res}$, where a resonance state ϵ_+ appears.

If it is assumed that the main losses are due to diffraction radiation, then for the values of l_{EB} and l_{EX} indicated above, the gain of the active medium for lasing[3] is at least an order of magnitude greater than for a laser operating on intersubband transitions. At the same time, it should be noted that the geometry with a parallel arrangement of the EF and the UP is suboptimal from the standpoint of device applications, and in this respect it loses to the crossed-configuration geometry for a number of reasons. In the first place, a static domain with a strong EF, the existence of which leads to high threshold pressures, has a negative effect on stimulated emission.[4,5] A domain arises as a result of a change in the hole mass at the inflection point of the dispersion curve $\epsilon(k)$ for $\mathbf{E}\|\mathbf{X}$.[6] We note that there is no such feature for $\mathbf{E}\perp\mathbf{X}$ (see Fig. 1). In the second place, the single-pass optical path length in the active medium for parallel $\mathbf{E}$ and $\mathbf{X}$ is several times smaller than for crossed orientations. Finally, in the latter case exterior mirrors can be used as cavities, which is technically difficult to implement for parallel directions.

The physical reason for the appearance of stimulated emission is inversion in the hole distribution on UP-split impurity states.[7] It is known that UP lifts the degeneracy of hole subbands for $\mathbf{k}=0$ and for impurity states,[8] and as the pressure changes, each of the split impurity levels follows its own subband. For $X>X_{\rm res}$ ($X_{\rm res}\cong 2.8$ kbar for $\mathbf{X}\|[100]$ and $X_{\rm res}\cong 4$ kbar for $\mathbf{X}\|[111]$) the upper split level ϵ_+ (ground state) lies in the continuous spectrum of the bottom subband ϵ_- and becomes resonant. As a result of the effective resonance scattering (trapping) of holes,[9] it is partially filled. At the same time, the lower impurity level ϵ_- in the gap is emptied as a result of breakdown in a strong EF. It turns out that the fact that the depth δ_+ of the upper impurity level relative to its subband ϵ_{+p} is much greater than the corresponding value of δ_- is favorable for inversion.

The results of an investigation of the effect of resonance states on electric current

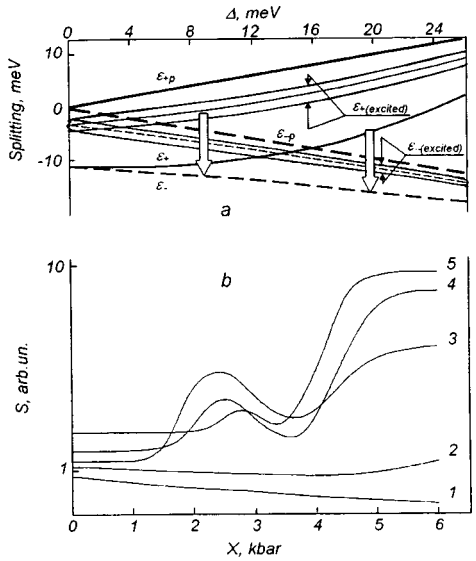

FIG. 2. a) Splitting of the valence subbands of the ground and excited states of impurity levels as a function of the pressure (ϵ_{+p} and ϵ_{-p} are the energies at the bottoms of the corresponding bands). The wide arrows show the transitions corresponding to the a maximum spectral sensitivity of the photodetector Ge(Ga) ($\lambda \approx 100$ μm). b) Radiation intensity versus the uniaxial pressure: $N_A - N_D \approx 7 \times 10^{14}$ cm^{-3}, $T = 4.2$ K, $\mathbf{X} \| [111]$, E, kV/cm: *1* — 0.5, *2* — 1.0; *3* — 1.4; *4* — 1.7; *5* — 1.8.

flow with $\mathbf{E} \perp \mathbf{X}$ for Ge samples cut in various crystallographic directions so that $\mathbf{X} \| [111]$ and $\mathbf{X} \| [100]$ were presented in Ref. 10. In the present letter we report the results of investigations of radiation in the range $\lambda \approx 100$ μm (the maximum of the spectral sensitivity of a Ge:Ga photodetector with quartz and black polyethylene filters) for similar rectangular samples with orthogonal directions of the EF and UP with $R = 4.2$ K. The optical signal was recorded with a recorded with pressure scanning and electric field pulses with a constant amplitude. The pulse repetition frequency was about 70 Hz, and the pulse duration was 0.4 μs.

EXPERIMENTAL RESULTS

Figure 2 shows the computed dependences of the positions of the valence subbands of Ge (Ref. 8) and the levels of the ground and excited states of a shallow Ga impurity (concerning the construction of these curves, see below) on the splitting Δ between the subbands and the experimentally determined pressure dependences of the spontaneous radiation intensity for one of the experimental samples ($\mathbf{X} \| [111]$). We note the correspondence between the abscissas: $\Delta = \alpha X$, $\alpha \cong 4$ meV/kbar.

The nonmonotonic behavior of the radiation intensity is interesting. We attribute the increase in the optical signal near 2.5 kbar to optical transitions from a group of the first excited states $\epsilon_{+\text{excited}}$ (which become resonant for $X > 1$ kbar) to the ground state level ϵ_-. The subsequent decrease of the signal with increasing pressure seems to be due to broadening of these states and a decrease of their depth below the bottom of the upper subband, which results in their being emptied in a strong EF. The maximum near 5 kbar

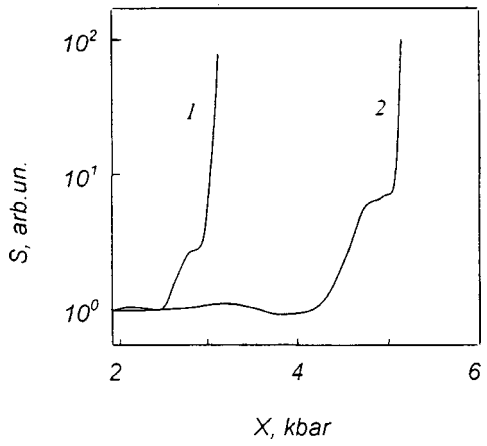

FIG. 3. Radiation intensity versus the UP at $T=4.2$ K: *1* — $\mathbf{X}\|[100]$, $N_A-N_D\approx 2\times 10^{14}$ cm^{-3}, $E=2.2$ kV/cm; *2* — $\mathbf{X}\|[111]$, $N_A-N_D\approx 7\times 10^{14}$ cm^{-3}, $E=2.0$ kV/cm.

could be due to transitions between the ground states ϵ_+ and ϵ_-. We note that in this case the parity forbiddenness of the states is lifted by the presence of a strong EF. Similar transitions have been observed for parallel orientations of EF and UP.[3] In Fig. 2 the wide arrows show the repective optical transitions with the same photon energy, corresponding to the sensitivity peak of the photodetector.

The pressure dependences of the position of the level ϵ_+ were obtained by passing a smooth curve through three points. The first point is the depth of the Ga level in undeformed Ge (11.3 meV). The second one corresponds to the appearance of a resonance level (approximately 16 meV), and the third one, for the case of high pressures $\Delta\geqslant 40$ meV (this point falls outside the limits of the figure), was taken from Ref. 11. The first three excited states,[11] with their broadening taken into account, are shown by a single wide band $\epsilon_{+\text{excited}}$ and were constructed in a similar manner. To ensure a unified approach, the dependences ϵ_- and $\epsilon_{-\text{excited}}$ were found similarly, even though the positions of these levels as a function of pressure are well known from experiments[12] and calculations,[13] and they agree well with the values obtained by the indicated method.

Qualitatively, we explain the relative position of the curves at the first maximum (Fig. 2b) as follows. For appreciable spontaneous emission, the population of the lower states should not exceed that of the upper states. For a relatively weak EF (curves *1* and *2*), the level ϵ_- remains populated (the incomplete emptying of the ground state of the impurity, in approximately the same fields, can be explained by a dip in the lasing region in the range 120–160 μm for a laser working at intersubband hole transitions in Ge in crossed E and B fields[14]). As the EF increases, the hole population of the level ϵ_- decreases, and appreciable spontaneous emission (curve *3*) arises. As the EF increases further, the excited states $\epsilon_{+\text{excited}}$ are also emptied, apparently because of breakdown and transition of holes into the hole subband ϵ_{+p}. As a result, the spontaneous emission intensity decreases (curves *4* and *5*).

The conclusion concerning the transition of holes into the hole subband is confirmed by the fact that at the second maximum the alternation of curves with increasing EF does

not occur. In this case, emptying of the ϵ_+ level (ground state) does not occur because of its large depth δ_+ below the bottom of its subband. At the same time, since δ_- decreases with increasing pressure, in identical electric fields the population of the level ϵ_- will be smaller for 5 kbar than 2.5 kbar. This is reflected in the fact that the increment to the radiation intensity and the values of the maxima themselves are greater for 5 kbar than 2.5 kbar.

Results similar to those presented in Fig. 2 were also obtained for $\mathbf{X} \| [100]$ ($\alpha \approx 6$ meV/kbar). If the radiation intensity is plotted as a function of the splitting Δ rather than the pressure X, then the positions of the maxima on the abscissa will be practically the same for both directions of the pressure.

On this basis, it is not surprising that for some samples a jump in the optical signal by two orders of magnitude was observed at the maximum of the spontaneous emission (see Fig. 3). We note first that the pressures corresponding to the threshold increase in the signal make it possible to attribute the signal to the appearance of resonance states ϵ_+. Then it can be concluded, by analogy to Ref. 3, that in strong EFs lasing on total internal reflection modes arises due to intracenter inversion in the hole distribution.

This work is partially supported by the Ukrainian Fund for Fundamental Studies (Grant No. 2.4/970) and grants from MOPO of the Russian Federation.

*)e-mail: tvn@laser.donetsk.ua

[1] A. A. Andronov, *Submillimeter Lasers Based on Hot Holes in Semiconductors* [in Russian] (Institute of Applied Physics, Soviet Academy of Sciences, Gorki, 1968).
[2] L. E. Vorob'ev, F. I. Osokin, V. I. Stafeev, and V. N. Tulupenko, JETP Lett. **35**, 440 (1982).
[3] I. V. Altukhov, M. S. Kagan, and V. N. Sinis, JETP Lett. **47**, 164 (1988).
[4] I. V. Altukhov, M. S. Kagan, K. A. Korolev, and V. N. Sinis, Zh. Éksp. Teor. Fiz. **103**, 1829 (1993) [JETP **76**, 903 (1993)].
[5] V. G. Belykh, A. T. Dalakyan, V. N. Tulupenko, and D. A. Firsov, Fiz. Tekh. Poluprovodn. **29**, 1764 (1995) [Semiconductors **29**, 921 (1995)].
[6] B. K. Ridley and T. B. Watkins, Proc. Phys. Soc. **78**, 293 (1961).
[7] I. V. Altukhov, M. S. Kagan, K. A. Korolev *et al.*, JETP Lett. **59**, 476 (1994).
[8] G. L. Bir and G. E Pikus, *Symmetry and Strain-Induced Effects in Semiconductors* (Wiley, New York, 1975) [Russian original, Nauka, Moscow, 1972].
[9] I. V. Altukhov, M. S. Kagan, K. A. Korolev *et al.*, Zh. Éksp. Teor. Fiz. **115**, 89 (1999) [JETP **88**, 51 (1999)].
[10] V. M. Bondar, A. T. Dalakyan, V. N. Tulupenko, and D. A. Firsov, JETP Lett. **69**, 676 (1999).
[11] M. A. Odnoblyudov, A. A. Pakhomov, I. N. Uassievich *et al.*, Fiz. Tekh. Poluprovodn. **31**, 1180 (1997) [Semiconductors **31**, 1014 (1997)].
[12] E. I. Voevodin, E. M. Gershenzon, G. N. Gol'tsman *et al.*, Fiz. Tekh. Poluprovodn. **8**, 1356 (1986) [*sic*].
[13] J. Broeckx and J. Vennik, Phys. Rev. B **35**, 6165 (1987).
[14] C. Kremser, W. Heiss, and K. Unterrainer, Appl. Phys. Lett. **60**, 1785 (1992).

Translated by M. E. Alferieff

Observation of MeV ions in long-pulse, large-scale laser-produced plasmas

F. B. Rosmej, D. H. H. Hoffmann, and W. Suess
Technische Universitaet Darmstadt, Institut für Kernphysik, D-64289 Darmstadt, Germany

M. Geissel, P. Pirzadeh, M. Roth, and W. Seelig
Technishe Universität Darmstadt, Institut für Angewandte Physik, D-64289 Darmstadt, Germany

A. Ya. Faenov, I. Yu. Skobelev, and A. I. Magunov
Multicharged Ions Spectra Data Center of VNIIFTRI, 141570 Mendeleevo, Russia

T. A. Pikuz
Multicharged Ions Spectra Data Center of VNIIFTRI, 141570 Mendeleevo, Russia; Bauman Moscow State Technical University, 107005 Moscow, Russia

R. Bock, U. N. Funk, U. Neuner, S. Udrea, A. Tauschwitz, and N. A. Tahir
Gesellschaft für Schwerionenforschung, Institute for Plasmaphysics, D-64291 Darmstadt, Germany

B. Yu. Sharkov
Institute of Experimental and Theoretical Physics, 117257 Moscow, Russia

N. E. Andreev
High Energy Density Research Center, Insitute of High Temperatures, Russian Academy of Sciences, 127412 Moscow, Russia

(Submitted 15 March 1999; resubmitted 16 June 1999)
Pis'ma Zh. Éksp. Teor. Fiz. **70**, No. 4, 262–267 (25 August 1999)

A new approach for investigation of the generation of fast ions and hot electrons inside the same plasma volume in laser-produced plasmas is proposed. It is based on the spectroscopic observation of line radiation from singly and doubly excited levels with simultaneous high spectral and spatial resolution. The experimental results demonstrate the observation of fast ions from highly charged target material inside the plasma volume and suggest that the generally accepted scaling relations are seriously invalid under certain conditions. Even at rather modest intensities ions with energies of several MeV are observed. © *1999 American Institute of Physics*. [S0021-3640(99)00716-1]

PACS numbers: 52.50.Jm, 52.25.Jm

When laser radiation interacts with solids a large number of particles, both light (electrons) and heavy (ions), can be accelerated to velocities of directed motion substantially exceeding thermal ones. This effect was found at the beginning of the 1960s.[1] At the present time such acceleration has been observed in plasmas created by laser pulses of

various duration, wavelengths, and intensities. The analysis of quite a number of different experiments carried out on 25 laser installations has yielded the empirical dependence of the mean energy of fast particles on the parameter $q\lambda^2$ (q is the laser flux density and λ is laser wavelength) over a wide range: $q\lambda^2=(10^{10}-10^{18})\ \mathrm{W}\cdot\mu\,\mathrm{m}^2/\mathrm{cm}^2$ (Ref. 2). For parameters $q\lambda^2<10^{13}\ \mathrm{W}\cdot\mu\,\mathrm{m}^2/\mathrm{cm}^2$ this dependence was determined from the results of experiments:[3–13] at $q\lambda^2=10^{13}\ \mathrm{W}\cdot\mu\,\mathrm{m}^2/\mathrm{cm}^2$ the mean energy of fast ions does not exceed values of about 1 keV/amu. This empirical estimate agrees quite well with known theoretical mechanisms of fast ion generation.[14–16] However there are known also experimental results[17,18] which do not fit into the generally accepted scaling relations: at $q\lambda^2=10^{13}\ \mathrm{W}\cdot\mu\,\mathrm{m}^2/\mathrm{cm}^2$ a mean energy of fast ions of about 10 keV/amu was observed. At present there is no comprehensive theory available which can account for the presence of fast particles outside the scaling relations.[2]

In all these previous experiments the mean energy of the fast ions was determined through time-of-flight measurements with Faraday cups, from the arrival of the peak signal of the fast ions. It is not obvious, however, that energy measurements outside the plasma correspond directly to the energy of the fast particles inside the plasma volume where the laser interaction takes place. The same drawback pertains to measurements of hot electrons.

The present paper reports experiments employing a quite different approach for the measurement of fast particles: registration of the emission lines from the target ions by means of spherically bent mica crystals,[19] a technique which provides simultaneous high spectral and spatial resolution and non-Maxwellian spectrum analysis.[20–22] The experimental results obtained show that even for rather modest intensities it is possible to accelerate ions to energies of directed motion of up to 100 keV/amu inside the plasma volume.

Experiments were carried out at the ''nhelix-laser'' installation (nanosecond high-energy laser for heavy ion experiments) at GSI in Darmstadt, Germany. The ''nhelix'' is a Nd-glass/Nd-YAG laser ($\lambda_{las}=1.06\mu\mathrm{m}$) with a pulse duration of 15 ns and an energy up to 100 J. The present experiments, however, were performed with an energy of 17 J. The laser radiation is focused with a planoconvex lens (diameter 100 mm, focal length $f=130$ mm) onto a solid Teflon (CF_2) target. In order to obtain different laser intensities at the target, the distance between the lens and the target was changed (by moving the lens). Investigation of the intensity inside the focus showed that no hot spots appeared.

Soft x-ray line radiation was recorded simultaneously by two spectrographs with spherically bent mica crystals. The mutual arrangement of laser beam, targets and spectrographs is shown schematically in Fig. 1a. The radii of curvature of the two crystals were 150 mm (No. 1 in Fig. 1b) and 100 mm (No. 2 in Fig. 1b). Both spectrographs were installed in the FSSR-2D scheme.[19,23] This allowed the recording of spectra with spectral resolution of $\lambda/\Delta\lambda=3000-5000$ and spatial resolution (with one-dimension) of $\delta x=25-45\mu\mathrm{m}$. The first spectrograph recorded the plasma radiation in the direction parallel to the target surface, and the second one at an angle of 55°. Spectrographs were tuned on the spectral range $\lambda=(14-15)$ Å, containing the resonance line Ly_α (the transition $2p-1s$) of the H-like ion FIX and the He_β line (transition $1s3p\,^1P_1-1s^2$) of He-like FVIII. Examples of the spectrograms are shown in Fig. 1b. The diameter of the emission area parallel to the target surface (x coordinate) was 540 μm (FWHM) for the Ly_α line and 810 μm for the He_β line. Investigations with a pinhole camera show that the

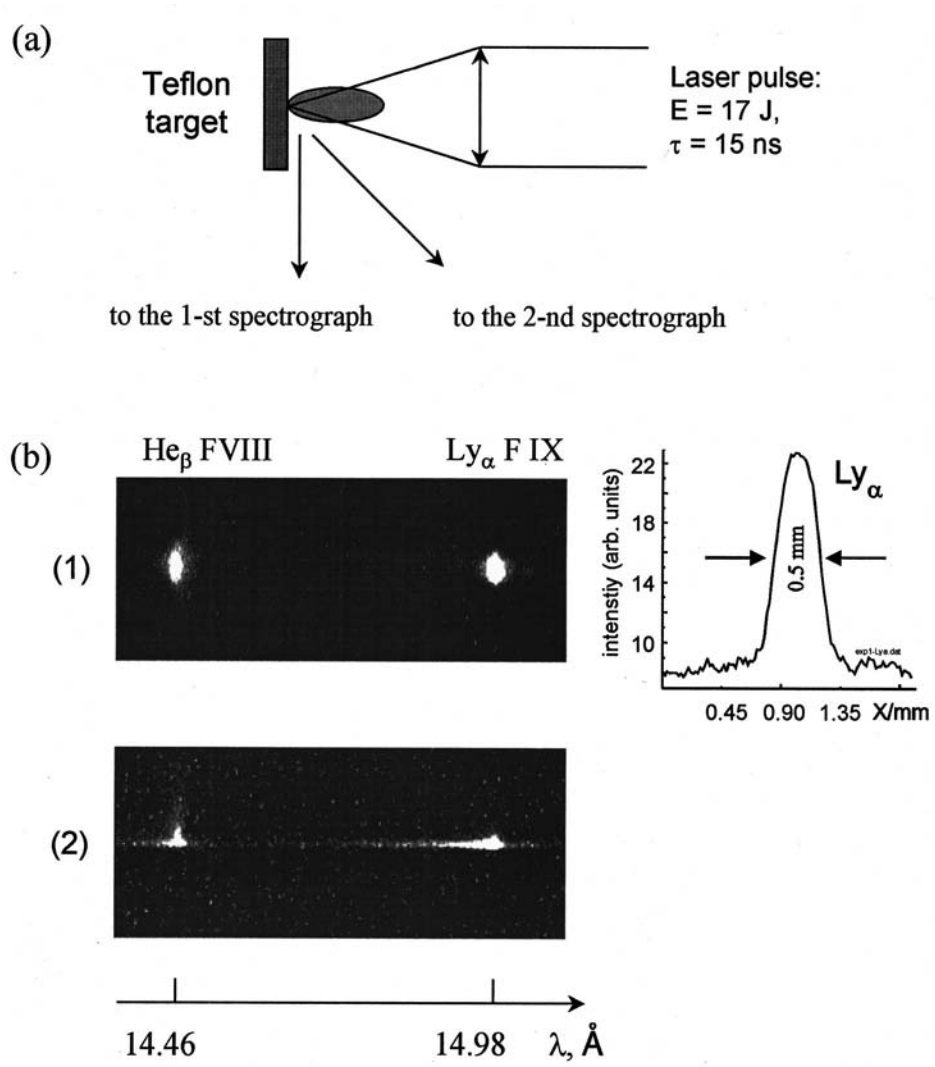

FIG. 1. Scheme of the experiment (a) and examples of spectrograms (b) obtained for different directions of observation: *1* — parallel to the target surface, *2* — at an angle of 55° to the target surface.

Ly_α emission region is about a factor of 2 smaller than those measured with the pinhole. Moreover, the observed long extended halo (up to about 1 cm) was identified as the emission of the He-like resonance and intercombination line ($He_\alpha = 1s2p\,^1P_1 - 1s^2$ and $Y_\alpha = 1s2p\,^3P_1 - 1s^2$, respectively). We note that for a spot size of 540 μm we obtain an averaged intensity of 5×10^{11} W/cm^2 at the target.

From Fig. 1b we can see the anisotropy of the spectral characteristics of the plasma radiation. Spectral lines recorded by the first spectrograph and, consequently, radiated in direction parallel to the target surface (i.e., in direction perpendicular to the direction of the predominant plasma expansion), are rather narrow and have the symmetrical line

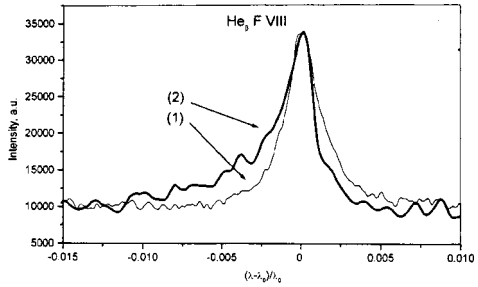

FIG. 2. Profile of the He_β line of the ion FVIII, radiated by a laser-produced plasma in the direction parallel to the target surface (1) and at an angle of 55° from the target surface (2).

shape (see also Figs. 2 and 3). Contrary to this, spectral lines recorded by the second spectrograph have strongly asymmetric profiles with enhanced short-wavelength wings.

It is possible to show that observed line profiles can not be explained by Stark effect in a dense plasma. For example, the theoretical results obtained for Ly_α- line of FIX are presented in Fig. 4. The line profiles were calculated taking into account the quasistatic ion microfield Stark broadening, the broadening due to elastic collisions with electrons, and the Doppler shifts, in the form

$$S_{21}(\omega)=\frac{1}{\pi^{1/2}\gamma_D A_{21}}\sum_\alpha A_{\alpha 1}\int_0^\infty V\left(\frac{\omega-\omega_{21}-\Delta\omega_\alpha\beta}{\gamma_D},\frac{\gamma_\alpha}{\gamma_D}\right)P_\alpha(Z_i,\beta)d\beta;$$

here $A_{\alpha 1}$ is the transition probability for the sublevel with the parabolic quantum numbers $\alpha\equiv(n_1,n_2,m)$, $V(x,y)$ is the Voigt function with the Doppler width γ_D and the collision width γ_α for each sublevel (according to Ref. 24), $\Delta\omega_\alpha$ is the linear Stark shift of the sublevel in the field $F_0=Z_i e/r_0^2$, $r_0=0.62N_i^{-1/3}$ is the mean separation between ions, Z_i and N_i are the mean ion charge and density, $P_a(Z_i,\beta)$ is the distribution function of the ionic field $F=F_0\beta$, which takes into account the Debye screening and ion correlation effects.[25] The parameter $a=r_0/r_D$, and r_D is the Debye length.

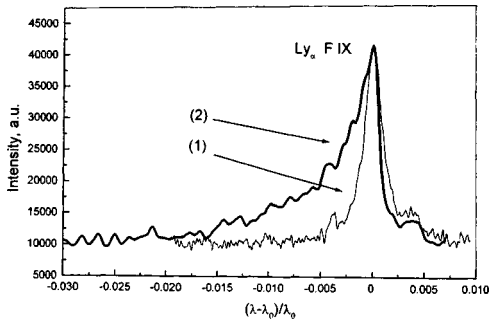

FIG. 3. Profile of the $2p-1s$ line of the ion FIX, radiated by laser-produced plasma in the direction parallel to the target surface (1) and at an angle of 55° from the target surface (2).

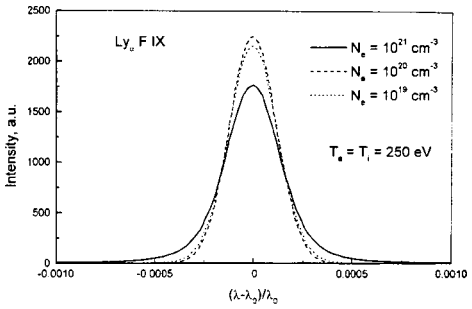

FIG. 4. The profiles of the $2p-1s$ line of the ion FIX, calculated with allowance for the quasistatic ion microfield Stark broadening, broadening due to the elastic collisions with electrons, and the Doppler broadening for a plasma with $T_e = T_i = 250$ eV.

It can be seen from Fig. 4 that even at a plasma density $N_e = 10^{21}\,\mathrm{cm}^{-3}$ the Stark effect has no substantial effect on either linewidth or line shift, and it cannot explain the experimental results.

The only, and very obvious, reason for such a difference of the spectra is the Doppler upshift of the frequencies of photons radiated in the direction of the predominant motion of ions. In this case the photons recorded by the first spectrograph experience practically no frequency shift (the transverse Doppler effect is negligible). The asymmetry of the lines recorded by the second spectrograph is connected with anisotropy of the microscopic movements of plasma from the flat massive target (the plasma can expand only away from the target, i.e., in direction toward the spectrograph). From the densitograms presented in Figs. 2 and 3 it is seen that a significant number of photons show a relative frequency shift of $(\lambda-\lambda_0)/\lambda_0 = (0.5-1.5)\times 10^{-2}$. These values corresponds to ion velocities in the direction of observation of $V_{\mathrm{obs}} = (1.5-4.5)\times 10^8$ cm/s. From these figures we can also see, that the velocities of fast H-like ions FIX and their concentration is higher than for He-like ions FVIII. The symmetrical shape of the profiles of lines recorded by the first spectrograph means that the motion of fast ions occurs normal to the target surface. It means that the perpendicular velocity component of their motion is $1/\cos 55° = 1.74$ times greater than V_{obs}. Hence, the energy of fast ions FIX in our experiments was about 2.5 MeV.

Figure 5 shows the space resolved He$_\alpha$ line, the intercombination line Y$_\alpha$ and the Li-like dielectronic satellite spectra $1s2lnl' - 1s^2 2l$ (registration with a third spherically bent mica crystal, $R = 100$ mm, same shot as in Fig. 1b, No. 1). Even for distances $x \approx 0.8$ mm, strong Doppler-shifted wings of the He$_\alpha$ line are observed, and closer to the target the wing structure is even more pronounced (we note that the so-called ''blue satellites''[26] cannot be the cause of the observed line wing asymmetry in our case). The spectral distribution of the dielectronic $1s2l2l'$ satellites (indicated as qr, a–d, jkl; for satellite designations see Ref. 27) is sensitive to hot electrons. Figure 6 shows the non-Maxwellian collisional–radiative calculations for an optically thick plasma carried out with the MARIA codes.[20] It can clearly be seen that with an increasing fraction f_{hot} (relative to the bulk electrons with density n_e(bulk)) of hot electrons (with density n_e(hot))

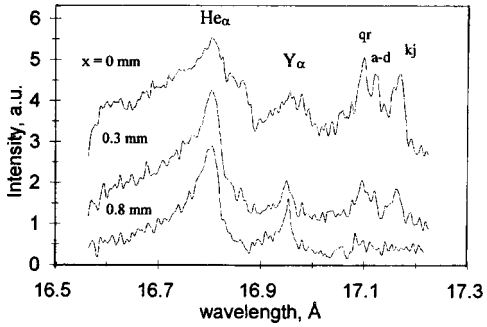

FIG. 5. Space-resolved He_α emission. The laser beam was perpendicular to the target, the angle between target and spectrometer was 45°; x is the distance from the target surface.

$$f_{\rm hot}=\frac{n_e({\rm hot})}{n_e({\rm hot})+n_e({\rm bulk})}$$

the intensity of the qr satellites increases relative to the jk satellites. This effect is based on the increased collisional inner-shell excitation of the qr satellites from the Li-like $1s^22l$ states by hot electrons, whereas for the jk satellites the dielectronic capture channels still dominate. Note that ion abundances are simultaneously calculated for non-Maxwellian electrons to take into account the shifted ionic populations for different charge states. As can be seen from Fig. 6 the shift to higher ionization states (caused by

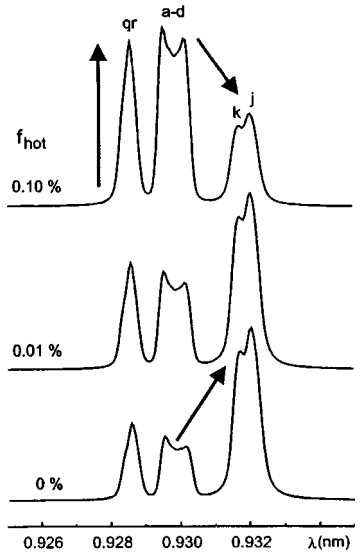

FIG. 6. Hot electron diagnostic based on the relative intensities of the Li-like dielectronic satellites qr, a–d, kj. The parameters for the non-Maxwellian collisional radiative MARIA modeling[20] are: nuclear charge $Z_n=12$, bulk electron temperature $kT_{\rm bulk}=100$ eV, electron density $n_e=10^{21}$ cm^{-3}, plasma size $L_{\rm eff}=500$ μm, beam ''temperature'' $kT_{\rm beam}=3$ keV. With increasing fraction of hot electrons, the qr satellites rise relative to the jk satellites.

increased ionization processes involving hot electrons) does not compensate the increased inner-shell excitation. Density variations showed that for our range of parameters, redistribution effects inside the $1s2l2l'$ satellite structure can not be made responsible for the qr/jk intensity interplay shown in Fig. 6.

In conclusion, we have developed a new diagnostic for the investigation of fast ion and hot electron generation by means of space-resolved high-resolution x-ray spectroscopy. Fast ions and hot electrons can be investigated inside the plasma and also inside the same plasma volume. The experimental results demonstrate that MeV ions can be generated at intensities much lower than predicted by scaling relations. According to the existing theoretical analyses based on quite a number of experimental results (see review[2]), such ion energies can arise only at much higher values (two orders of magnitude higher values of the parameter $q\lambda^2$).

This work was supported in part by INTAS Grant 97-2090.

[1] W. I. Linlor, Appl. Phys. Lett. **3**, 210 (1963).
[2] S. J. Gitomer, R. D. Jones, F. Begay *et al.*, Phys. Phys. Fluids **29**(8), 2679 (1986).
[3] E. W. Sucov, J. L. Pack, A. V. Phelps, and A. G. Engelhardt, Phys. Fluids **10**, 2035 (1967).
[4] B. C. Boland, F. E. Irons, and R. W. P. McWhirter, J. Phys. B **1**, 1180 (1968).
[5] H. Puell, H. J. Neusser, and K. Kaiser, Z. Naturforsch. A **25**, 1815 (1970).
[6] H. B. Kang, T. Yamanaka, K. Yoshida *et al.*, Jpn. J. Appl. Phys. **11**, 765 (1972).
[7] K. Dick, H. Pepin, J. Martineau *et al.*, J. Appl. Phys. **44**, 3284 (1973).
[8] R. E. Beverly, Phys. Lett. **44**, 321 (1973).
[9] P. T. Rumsby and J. W. M. Paul, Plasma Phys. **16**, 247 (1974).
[10] B. Luther-Davies and J. L. Hughes, Opt. Commun. **18**, 351 (1976).
[11] M. R. Siegrist, B. Luther-Davies, and J. L. Hughes, Opt. Commun. **18**, 603 (1976).
[12] C. Stenz, C. Popovics, E. Fabre *et al.*, J. Phys. (Paris) **38**, 761 (1977).
[13] B. Luther-Davies, Opt. Commun. **23**, 98 (1977).
[14] D. W. Forslund and J. U. Blackbill, Phys. Rev. Lett. **48**, 1614 (1982).
[15] N. E. Andreev, Yu. A. Zakharenkov, N. N. Zorev *et al.*, Zh. Éksp. Teor. Fiz. **70**, 547 (1976) [Sov. Phys. JETP **43**, 283 (1976)].
[16] N. E. Andreev, Yu. A. Andreev, N. N. Zorev *et al.*, Zh. Éksp. Teor. Fiz. **76**, 976 (1979) [Sov. Phys. JETP **49**, 492 (1979)].
[17] P. Wagli and T. P. Donaldson, Phys. Rev. Lett. **40**, 875 (1978).
[18] P. Wagli, T. P. Donaldson, and P. Ladrach, Appl. Phys. Lett. **32**, 638 (1978).
[19] I. Yu. Skobelev, A. Ya. Faenov, B. A. Briunetkin *et al.*, Zh. Éksp. Teor. Fiz. **108**, 1263 (1995) [JETP **81**, 692 (1995)].
[20] F. B. Rosmej, J. Phys. B **30**, L819 (1997).
[21] F. B. Rosmej, J. Quant. Spectrosc. Radiat. Transf. **51**, 319 (1994).
[22] F. B. Rosmej, A. Ya. Faenov, T. A. Pikuz *et al.*, J. Quant. Spectrosc. Radiat. Transf. **58**, 859 (1997).
[23] B. K. F. Young, A. L. Osterheld, D. F. Price *et al.*, Rev. Sci. Instrum. **69**, 4049 (1998).
[24] H. R. Griem, *Spectral Line Broadening by Plasmas*, Academic Press, New York, 1974.
[25] R. J. Tighe and C. F. Hooper Jr., Phys. Rev. A **14**, 1514 (1976).
[26] F. B. Rosmej and J. Abdallah, Phys. Lett. A **245**, 548 (1998).
[27] A. H. Gabriel, Mon. Not. R. Astron. Soc. **160**, 99 (1972).

Published in English in the original Russian journal. Edited by Steve Torstveit.

Ohm's law in a chiral plasma

O. G. Chkhetiani*) and S. S. Moiseev
Institute of Space Studies, 117810 Moscow, Russia

(Submitted 12 May 1999; resubmitted 7 July 1999)
Pis'ma Zh. Éksp. Teor. Fiz. **70**, No. 4, 268–273 (25 August 1999)

The motion of plasma electrons in a stochastic electromagnetic field is studied in the low-conductivity limit. It is shown that under very general conditions, in the presence of a nonzero average chirality of the small-scale electromagnetic field, the effective current depends on the curl of the applied electric field, $\mathbf{j}=\sigma\mathbf{E}+\sigma_\kappa \operatorname{curl}\mathbf{E}$, just as for similar dependences for the electric displacement and magnetic induction vectors in optically active and artificial chiral media. Under certain conditions such an Ohm's law leads to growth of the magnetic field, the structure of the growth being dependent on the conductivity of the medium. © *1999 American Institute of Physics.*
[S0021-3640(99)00816-6]

PACS numbers: 52.40.Db, 52.20.−j

In recent years investigators have been specially drawn to phenomena arising in the context of chiral electrodynamics. The generalized laws expressing the relationship between the inductions (magnetic induction and electric displacement) and field intensities (magnetic and electric fields) are used as a basis for studying such phenomena. For example, the electric displacement is represented as[1–3]

$$\mathbf{D}=\varepsilon_0\mathbf{E}+\varepsilon_\kappa \operatorname{curl}\mathbf{E}. \tag{1}$$

Here $\mathbf{E}$ is the electric field, ε_0 is the permittivity of the isotropic medium, and ε_κ is a pseudoscalar chirality parameter.

The breaking of the mirror symmetry of micromotions should also lead to a generalization of Ohm's law for the current:

$$\mathbf{j}=\sigma\mathbf{E}+\sigma_\kappa \operatorname{curl}\mathbf{E}. \tag{2}$$

Here σ and σ_κ are, respectively, the conductivity and the chirality parameter.

One possible cause of chirality is asymmetry of the structure of the substance, specifically, the right–left asymmetry of molecules. At the same time, substances with a simple structure (for example, an electron–proton plasma) do not have this possibility. For them chirality can arise either as a result of reflection-asymmetric motions or because the electromagnetic fields possess such a property. For this, for example, it is sufficient for the random electromagnetic field to possess nonzero averages $\langle \mathbf{A}\cdot\operatorname{curl}\mathbf{A}\rangle$ ($\mathbf{A}$ is the vector potential, $\langle \ldots \rangle$ is the ensemble average). Reflection-asymmetric effects in the current have also been taken into account previously in the analysis of the generation of large-scale magnetic structures (see, for example, Ref. 4 and the bibliography given

therein). However, this was not done sufficiently systematically, which, specifically, in the approximation of electronic magnetohydrodynamics (EMHD) cannot lead to the correct form of Ohm's law. We note in conclusion that the possibility of the existence of Eq. (2) also follows from the representation of Ohm's law in a plasma in terms of the correlation function of microcurrents,[5] if it is assumed that mirror symmetry of the latter is broken.

Let us consider the motion of electrons in a stochastic electromagnetic field with prescribed correlation properties. Taking into account the inertia of the electrons will enable us to prove the validity of the generalized Ohm's law (2) in a plasma with random chiral fields and to calculate directly the parameters σ and σ_κ. We consider the case where the ion motion can be neglected (EMHD approximation).

Let us assume that initially a regular large-scale nonuniform electric-field perturbation, weak enough to change substantially the correlation properties of the fluctuations of the electromagnetic fields, is imposed initially on the system. We note that in Ref. 6 the behavior of plasma in a completely isotropic electromagnetic random chiral field was investigated in the kinetic approximation, and the properties of the velocity distribution function of the charged particles were analyzed. However, in Ref. 6 there was no average electric field and Ohm's law was not studied.

Let us write for the velocity $\mathbf{v}$ of the electrons

$$\frac{d\mathbf{v}}{dt}=\frac{e}{m_e}\left(\mathbf{E}+\frac{1}{c}[\mathbf{v}\times\mathbf{B}]\right). \tag{3}$$

Decomposing the electromagnetic field into a sum of a large-scale slow component and a fast small-scale component (with zero average), we write

$$\mathbf{E}=\langle\mathbf{E}\rangle+\tilde{\mathbf{E}},\quad \mathbf{B}=\langle\mathbf{B}\rangle+\tilde{\mathbf{B}}. \tag{4}$$

As already mentioned above,

$$|\langle\mathbf{E}\rangle|\ll\langle\tilde{\mathbf{E}}^2\rangle^{1/2},\quad |\langle\mathbf{B}\rangle|\ll\langle\tilde{\mathbf{B}}^2\rangle^{1/2}.$$

Switching to the Fourier representation, we write

$$-iw\langle\hat{\mathbf{v}}(\mathbf{k},w)\rangle=\frac{e}{m_e}\left(\langle\hat{\mathbf{E}}(\mathbf{k},w)\rangle+\frac{1}{c}\int[\langle\hat{\mathbf{v}}(\mathbf{q},s)\times\hat{\mathbf{B}}(\mathbf{k}-\mathbf{q},w-s)\rangle]d\mathbf{q}ds\right). \tag{5}$$

The correlation $\langle\hat{\mathbf{v}}(\mathbf{q},s)\times\hat{\mathbf{B}}(\mathbf{k}-\mathbf{q},w-s)$ can be expressed in terms of the cumulants of the stochastic magnetic field according to the Furutsu–Novikov–Donsker formula[7]

$$\begin{aligned}\langle\hat{\mathbf{v}}(\mathbf{q},s)\times\hat{\mathbf{B}}(\mathbf{k}-\mathbf{q},w-s)\rangle_i&=\varepsilon_{ijk}\int\left\langle\frac{\delta\hat{v}_j(\mathbf{q},s)}{\delta\hat{B}_m(\mathbf{k}',w')}\right\rangle\langle\hat{B}_m(\mathbf{k}',w')\hat{B}_k(\mathbf{k}-\mathbf{q},w-s)\rangle d\mathbf{k}'dw'+\varepsilon_{ijk}\\&\times\int\left\langle\frac{\delta^2\hat{v}_j(\mathbf{q},s)}{\delta\hat{B}_m(\mathbf{k}',w')\,\delta\hat{B}_n(\mathbf{k}'',w'')}\right\rangle\langle\hat{B}_m(\mathbf{k}',w')\hat{B}_n(\mathbf{k}'',w'')\hat{B}_k\\&\times(\mathbf{k}-\mathbf{q},w-s)\rangle d\mathbf{k}'d\mathbf{k}''dw'dw''+\ldots\end{aligned} \tag{6}$$

The variational derivative $\langle \delta\hat{v}_j(\mathbf{q},s)/\delta\hat{B}_m(\mathbf{k}',w')\rangle$ satisfies the equation

$$-is\left\langle \frac{\delta\hat{v}_j(\mathbf{q},s)}{\delta\hat{B}_m(\mathbf{k}',w')}\right\rangle = -\frac{es}{m_e c}\varepsilon_{jlm}\frac{q_l}{q^2}\delta(s-w')\delta(\mathbf{q}-\mathbf{k}') + \frac{e}{m_e c}\varepsilon_{jlm}\langle \hat{v}_l(\mathbf{q}-\mathbf{k}',s-w')\rangle + \frac{e}{m_e c}\varepsilon_{jlr} \times \int \left\langle \frac{\delta\hat{v}_l(\mathbf{q}',s')}{\delta\hat{B}_m(\mathbf{k}',w')}\right\rangle \langle \hat{B}_r(\mathbf{q}-\mathbf{q}',s-s')\rangle d\mathbf{q}'ds' + \frac{e}{m_e c}\varepsilon_{jlr} \times \left\langle \frac{\delta^2\hat{v}_l(\mathbf{q}',s')}{\delta\hat{B}_m(\mathbf{k}',w')\delta\hat{B}_n(\mathbf{q}'-\mathbf{q},s'-s)}\right\rangle \hat{Q}_{nr}(\mathbf{q}-\mathbf{q}',s-s'). \quad (7)$$

Here

$$\langle \hat{B}_m(\mathbf{k}',w')\hat{B}_k(\mathbf{k}-\mathbf{q},w-s)\rangle = \hat{Q}_{mk}(\mathbf{k}-\mathbf{q},w-s)\delta(\mathbf{k}-\mathbf{q}+\mathbf{k}')\delta(w-s+w'). \quad (8)$$

For uniform isotropic gyrotropic fluctuations the correlation tensor has the form

$$\hat{Q}_{mk}(\mathbf{q},s) = \left(\delta_{mk}-\frac{q_m q_k}{q^2}\right)\frac{E_M(q,s)}{4\pi q^2} + i\frac{H_M(q,s)}{8\pi q^4}\varepsilon_{mkt}q_t. \quad (9)$$

The equation for the second variational derivative contains the third, and so on. In the general case the problem is not closed. The systematic procedure proposed in Ref. 8 can be used to take into account correlation times which are not short. In the present letter we confine our attention to the limit of fluctuations which are δ-correlated in time. Then the first term remains in Eq. (6), which is identical to the Gaussian approximation. This is a good approximation for short correlation times also. The last term in Eq. (7) is zero. Then, taking into account the nonuniformity of the average magnetic field up to second order in the perturbation theory, we obtain

$$\left\langle \frac{\delta\hat{v}_j(\mathbf{q},s)}{\delta\hat{B}_m(\mathbf{k}',w')}\right\rangle = -i\frac{e}{m_e c}\varepsilon_{jlm}\frac{q_l}{q^2}\delta(s-w')\delta(\mathbf{q}-\mathbf{k}') + i\frac{e}{sm_e c}\varepsilon_{jlm}\langle \hat{v}_l(\mathbf{q}-\mathbf{k}',s-w')\rangle + \frac{1}{s}\left(\frac{e}{m_e c}\right)^2\varepsilon_{jlr}\varepsilon_{lpm}\frac{k'_p}{k'^2}\langle \hat{B}_r(\mathbf{q}-\mathbf{k}',s-w')\rangle. \quad (10)$$

The higher orders, assuming the perturbations of the average fields and currents to be small, can be neglected. Substituting expression (10) into Eq. (5) and integrating over $\mathbf{q}$ and s, in the limit of a random process which is δ correlated in time [the temporal part of the correlation function is $2\tau_{\mathrm{cor}}\delta(t-t')$], we find that the average equation of motion of an electron in a weak nonuniform electric field against the background of uniform fluctuations of the electromagnetic background has the form

$$\left(-iw+\frac{2}{3}\left(\frac{e}{m_ec}\right)^2\langle\mathbf{B}^2\rangle\tau_{\rm cor}\right)\langle\hat{\mathbf{v}}\rangle=\frac{e}{m_e}\left(\langle\hat{\mathbf{E}}\rangle-\frac{2}{3}\frac{e}{m_e}\left(\frac{e}{m_ec}\right)^2\frac{\tau_{\rm cor}}{iw}\langle\mathbf{A}\cdot\mathbf{B}\rangle i[\mathbf{k}\times\langle\hat{\mathbf{E}}\rangle]\right.$$
$$\left.+\frac{2}{3}\frac{e}{m_e}\left(\frac{e}{m_ec}\right)^2\frac{\tau_{\rm cor}}{iw}\langle\mathbf{A}^2\rangle[\mathbf{k}\times[\mathbf{k}\times\langle\hat{\mathbf{E}}\rangle]]\right), \quad (11)$$

where the effective transport coefficients are directly related with the average energy, helicity, and squared rotational component of the vector potential of the stochastic magnetic field ($\mathrm{curl}\,\mathbf{A}=\mathbf{B}$):

$$\langle\mathbf{B}^2\rangle=\int E_M(q)dq,\quad \langle\mathbf{A}\cdot\mathbf{B}\rangle=\int\frac{H_M(q)}{q^2}dq,\quad \langle\mathbf{A}^2\rangle=\int\frac{E_M(q)}{q^2}dq. \quad (12)$$

We note that in order for the indicated averages to converge, $E_M(q)$ must decrease at infinity more rapidly than q^{-1}, and in the limit $q\to 0$ it must behave as q^m, where $m\geqslant 1$. The latter restriction also pertains to $H_M(q,s)$. In the calculations, the relationship between the fields **B** and **E** in terms of the Maxwell's equation, written in the Fourier representation as $\hat{\mathbf{B}}=c/w\,[\mathbf{k}\times\hat{\mathbf{E}}]$, and the series expansion of the tensor $\hat{Q}_{mk}(\mathbf{k}-\mathbf{q},w-s)=\hat{Q}_{km}(\mathbf{q}-\mathbf{k},s-w)$ for $k\ll q$ were used.

In the functional approach, it is not difficult to take account of non-Gaussian effects. We note that, as a rule, they lead to renormalization of the effective transport coefficients obtained in the Gaussian or short-correlated approximation.[9–11]

Determining the mean-square Larmor frequency of the magnetic-field fluctuations as $\overline{w_L^2}=\langle e\mathbf{B}/m_ec\rangle^2$, we write for the conductivity tensor $j_i(\mathbf{k},w)=\hat{\sigma}_{il}(\mathbf{k},w)E_l(\mathbf{k},w)$:

$$\hat{\sigma}_{il}(\mathbf{k},w)=\frac{ne^2}{\left(-iw+\frac{2}{3}\left(\frac{e}{m_ec}\right)^2\langle\mathbf{B}^2\rangle\tau_{\rm cor}\right)m_e}\left[\left(1-\frac{2}{3}\frac{\overline{w_L^2}\tau_{\rm cor}}{iw}\frac{\langle\mathbf{A}^2\rangle}{\langle\mathbf{B}^2\rangle}k^2\right)\delta_{il}\right.$$
$$\left.+\frac{2}{3}\frac{\overline{w_L^2}\tau_{\rm cor}}{iw}\frac{\langle\mathbf{A}^2\rangle}{\langle\mathbf{B}^2\rangle}k_ik_l-\frac{2}{3}\frac{\overline{w_L^2}\tau_{\rm cor}}{iw}\frac{\langle\mathbf{A}\cdot\mathbf{B}\rangle}{\langle\mathbf{B}^2\rangle}i\varepsilon_{irl}k_r\right]. \quad (13)$$

The particle collision frequency $\nu=1/\tau$ is taken into account via the substitution $-iw\to(-iw+\nu)$, whence

$$\mathbf{j}(k,0)=(\sigma+\sigma_*k^2)\langle\hat{\mathbf{E}}(\mathbf{k},w)\rangle-\sigma_*\mathbf{k}(\mathbf{k}\cdot\langle\hat{\mathbf{E}}(\mathbf{k},w)\rangle)+i\sigma_\kappa[\mathbf{k}\times\langle\hat{\mathbf{E}}(\mathbf{k},w)\rangle], \quad (14)$$

where

$$\sigma=\frac{ne^2\tau}{\left(1+\frac{2}{3}\left(\frac{e}{m_ec}\right)^2\langle\mathbf{B}^2\rangle\tau_{\rm cor}\tau\right)m_e},\quad \sigma_\kappa=\frac{2}{3}\frac{\langle\mathbf{A}\cdot\mathbf{B}\rangle}{\langle\mathbf{B}^2\rangle}\overline{w_L^2}\tau_{\rm cor}\tau\cdot\sigma,$$
$$\sigma_*=\frac{2}{3}\frac{\langle\mathbf{A}^2\rangle}{\langle\mathbf{B}^2\rangle}\overline{w_L^2}\tau_{\rm cor}\tau\cdot\sigma, \quad (15)$$

Performing the inverse Fourier transform we obtain for the current

$$\mathbf{j}=\sigma\langle\mathbf{E}\rangle+\sigma_\kappa\,\mathrm{curl}\langle\mathbf{E}\rangle-\sigma_*\Delta\langle\mathbf{E}\rangle+\sigma_*\nabla\mathrm{div}\langle\mathbf{E}\rangle. \quad (16)$$

Therefore the effective Ohm's law in a fluctuational electromagnetic field with nonzero average chirality (helicity) does indeed have the form (2), similar to the dependences for the induction and magnetization in optically active and chiral media.

Let us examine the evolution of the average magnetic field in a medium with a fluctuating electromagnetic field with nonzero chirality, using the obtained Ohm's law. Studying the problem in the Fourier representation, we introduce the linear operator

$$\hat{L}_{ij}=\delta_{ij}-\frac{\sigma_*}{\sigma+\sigma_* k^2}k_i k_j+i\frac{\sigma_\kappa}{\sigma+\sigma_* k^2}\varepsilon_{ilj}k_l. \tag{17}$$

For the inverse operator $\hat{L}^{-1}$ we have

$$\hat{L}^{-1}_{ij}=\frac{\delta_{ij}-i(\sigma_\kappa/(\sigma+\sigma_* k^2))(1-\sigma_* k^2/(\sigma+\sigma_* k^2))\varepsilon_{ilj}k_l}{(1-(\sigma_\kappa/(\sigma+\sigma_* k^2))^2 k^2)}$$
$$+\frac{(\sigma_*/(\sigma+\sigma_* k^2)-(\sigma_\kappa/(\sigma+\sigma_* k^2))^2)k_i k_j}{(1-\sigma_* k^2/(\sigma+\sigma_* k^2))\left(1-\left(\dfrac{\sigma_\kappa}{\sigma+\sigma_* k^2}\right)^2 k^2\right)}. \tag{18}$$

If we neglect the displacement current, the electric field $\hat{\mathbf{E}}$ is

$$\hat{\mathbf{E}}=\frac{ic}{4\pi(\sigma+\sigma_* k^2)}\hat{L}^{-1}[\mathbf{k}\times\hat{\mathbf{B}}]. \tag{19}$$

and the closed equation for $\hat{\mathbf{B}}$ assumes the form

$$\frac{\partial\hat{\mathbf{B}}}{\partial t}=-\frac{c^2k^2}{4\pi(\sigma+\sigma_* k^2)}\frac{(\hat{\mathbf{B}}-is[\mathbf{k}\times\hat{\mathbf{B}}])}{1-s^2k^2}, \tag{20}$$

where

$$s=\frac{\sigma_\kappa}{\sigma+\sigma_* k^2}.$$

The equation (20) is nonlocal. At first glance, an additional curl falls outside the scaling accuracy — it is of order k^3, and it and the next additional term in the equation for the average large-scale magnetic field could be neglected. However, considering a solution of the form

$$\hat{\mathbf{B}}(\mathbf{k},t)=\hat{\mathbf{B}}(\mathbf{k},0)\exp(\gamma t),$$

we obtain for the growth rate

$$\gamma_{1,2}=-\frac{c^2k^2}{4\pi(\sigma+\sigma_* k^2\pm\sigma_\kappa k)}. \tag{21}$$

As one can see from Eq. (21), the dependence of the growth rate on the wave number actually does not exceed k^2. Depending on the values of the coefficients σ, σ_*, and σ_κ

the following situations are possible: 1) for $|\sigma_\kappa| < 2(\sigma\sigma_*)^{1/2}$ the disturbances of the average magnetic field decay for all values of k; 2) for $|\sigma_\kappa| \geqslant 2(\sigma\sigma_*)^{1/2}$ exponential growth of the magnetic field is possible on the scales

$$\frac{|\sigma_\kappa| - (\sigma_\kappa^2 - 4\sigma\sigma_*)^{1/2}}{2\sigma_*} < k < \frac{|\sigma_\kappa| + (\sigma_\kappa^2 - 4\sigma\sigma_*)^{1/2}}{2\sigma_*}. \tag{22}$$

A characteristic feature of this instability is the existence of threshold minimal and maximal scales for the unstable modes. If we introduce the characteristic scale λ of the fluctuational magnetic field and the characteristic chiral scale λ_κ, then the characteristic scale of the unstable modes will be of order $l \sim 2\lambda^2/\lambda_\kappa$. It could turn out that the instability of the mean field will develop in a large-scale region and at the boundary of or inside the dissipation interval. We thereby see that together with the inverse cascade processes there can also be direct cascade processes — the short-wavelength generation of an average magnetic field.

The instability obtained shows that in the presence of a sufficient level of fluctuational chirality, coherent perturbations of the magnetic field can grow also in a situation that is the opposite of the high-conductivity cases (studied, for example, in Ref. 4 and also associated with chirality). The general case and the boundary where both possibilities become equal will be the subject of a further investigation.

This work was supported in part by the Russian Fund for Fundamental Research (Grant No. 98-02-17229) and INTAS (Georgia–INTAS Joint Project 504).

*)E-mail: ochkheti@mx.iki.rssi.ru

[1] F. I. Fedorov, *The Theory of Gyrotropy* [in Russian] (Nauka i tekhnika, Minsk, 1976).
[2] N. H. Kritikos and D. L. Jaggard (eds.), *Recent Advances in Electromagnetic Theory*, (Springer–Verlag, New York, 1990).
[3] H. T. Silva, P. H. Sakanaka, and N. Reggianni, J. Phys. Soc. Jpn. **67**, 850 (1998).
[4] S. I. Vaĭnshteĭn, Ya. B. Zel'dovich, and A. A. Ruzmaĭkin, *The Turbulent Dynamo in Astrophysics* [in Russian] (Nauka, Moscow, 1980).
[5] V. D. Shafranov, in *Reviews of Plasma Physics*, Vol. 3, edited by M. A. Leontovich (Consultants Bureau, New York, 1967) [Russian original, Énergoatomizdat, Moscow, 1963, p. 3].
[6] A. V. Chechkin, V. Yu. Yanovsky, and A. V. Tur, Phys. Plasmas **1**(8), 2566 (1994).
[7] E. A. Novikov, Zh. Éksp. Teor. Fiz. **47**, 1919 (1964) [Sov. Phys. JETP **20**, 1290 (1965)].
[8] V. I. Klyatskin and V. I. Tatarskiĭ, Izv. Vyssh. Uchebn. Zaved. Radiofiz. **15**, 1433 (1972).
[9] E. Knobloch, J. Fluid Mech. **83**, 129 (1977).
[10] B. Nicklaus and M. Stix, Geophys. Astrophys. Fluid Dyn. **43**, 149 (1989).
[11] A. V. Belian, O. G. Chkhetiani, and S. S. Moiseev, IKI RAN Preprint N–1957 [in Russian], Institute of Space Studies, Russian Academy of Sciences, Moscow (1996).

Translated by M. E. Alferieff

On the state of supersaturation of a 2D electron system on a liquid-helium surface

V. B. Shikin

Institute of Solid-State Physics, Russian Academy of Sciences, 142432 Chernogolovka, Moscow Region, Russia

(Submitted 9 June 1999)
Pis'ma Zh. Éksp. Teor. Fiz. **70**, No. 4, 274–278 (25 August 1999)

The reasons why supersaturated states appear for a 2D electron system on a liquid-helium surface and the possibility of stationary existence of such states are discussed. The main characteristics of a 2D electron system on helium under stationary saturation conditions are calculated. It is shown that the well-known saturation state for electrons above helium is one of a continuum of supersaturated states. The experimental possibilities for observing and identifying supersaturated states for electrons on a helium surface are noted. © *1999 American Institute of Physics.* [S0021-3640(99)00916-0]

PACS numbers: 67.55.−s, 73.20.−r, 84.32.Tt

A 2D electron system on a liquid-helium surface is conventionally prepared using a flat capacitor with a charged liquid boundary between the plates (see, for example, Ref. 1). The potential difference V on the capacitor plates leads to the appearance of electric fields E_+ and E_- above and below this boundary,

$$E_+ = -\frac{4\pi e n_s d + V}{d+h}, \quad E_- = \frac{4\pi e n_s h - V}{d+h}, \quad d+h \ll W, \tag{1}$$

that confine the 2D electron system with finite density n_s near the vapor–liquid surface. Here d and h are, respectively, the thickness of the helium film and the width of the vacuum gap between the helium and the top electrode. The dimensions of the capacitor in the horizontal plane are $2W$.

Under the conditions $E_+ = 0$ or

$$V_s = -4\pi e n_s d \tag{2}$$

the electrons are no longer confined on a liquid substrate by the external field and they ''escape'' into the interior volume of the gas phase of helium. A 2D electron system is said to be saturated in relation to Eq. (2).

Formula (2) makes it possible to determine the density n_s quite simply, and for this reason the properties of a 2D electron system in a saturation state on helium are very commonly studied. Nonetheless, the important details of a state with saturation need to be determined more accurately, as proposed in the present letter. The problem is to describe saturation as one of a continuum of supersaturated states in a system of electrons on helium, where charges are located not only on the main liquid-helium surface but can

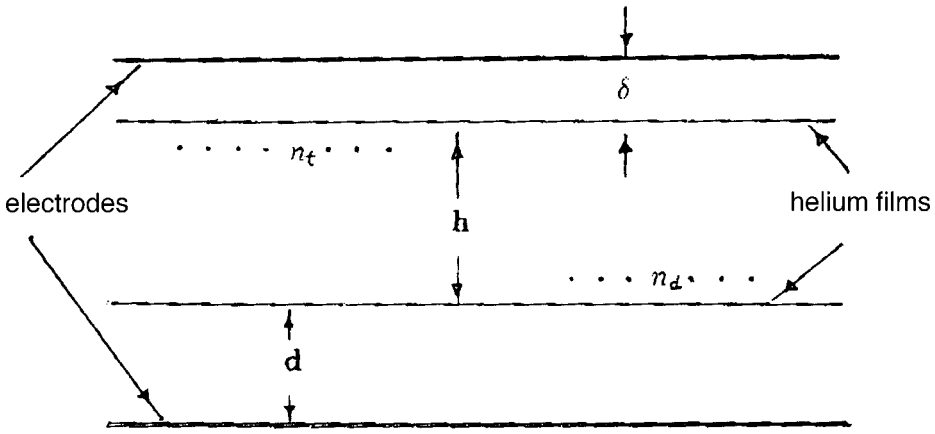

FIG. 1. Arrangement of electrons on helium films in the two-component approximation.

also be localized on other parts of the cell that are coated with a thin helium film, parts of the cell, specifically, on the top capacitor plate. The properties of the two-layer electron system arising have still not been discussed systematically.

1. We note, first of all, that for Eqs. (1) and (2) to hold, the electrons must have free access to the top capacitor plate. In reality, however, when working with superfluid helium, all inner parts of the cell, including the top capacitor plate, are coated with a thin (of the order of the natural thickness $\delta \sim 10^{-6}$ cm) helium film. Under these conditions the general picture of the filling of a vacuum gap above helium by electrons changes, because in the charging process the electrons settle with density n_d not only on the bottom film d but also with density n_t on the top film δ:

$$n_d + n_t = n_s . \tag{3}$$

In what follows, a state with two 2D electron layers is said to be supersaturated. The state of supersaturation is shown schematically in Fig. 1. To describe this state in the electrostatic approximation, the electric field between the two 2D electron layers must vanish (in addition, the definitions leading to Eq. (1) are also required). Here

$$4\pi e n_d = \frac{4\pi e n_s \delta - V}{d+\delta}, \quad n_t = n_s - n_d . \tag{4}$$

It is easy to see that in the two-layer model the electron density above the helium can be finite without having $V \neq 0$, because in the absence of voltage

$$4\pi e n_d^o = \frac{4\pi e n_s \delta}{d+\delta}, \quad 4\pi e n_t^o = \frac{4\pi e n_s d}{d+\delta}. \tag{5}$$

Here the internal Coulomb fields confine the electrons in local states on the top and bottom helium films. The total number N of electrons is limited only by the stability of the charged helium surface.

It is natural that for the critical value V_s (2) in the electrostatic approximation all electrons are on the d film, i.e., $n_d = n_s$.

Therefore, in the problem with films δ and d the existence region of 2D equilibrium electronic states above helium expands. Their presence becomes possible even under supersaturation conditions

$$0 \leqslant V \leqslant V_s, \tag{6}$$

and the saturation (2) can be interpreted as one of the supersaturated states.

We also note that according to Eq. (4), in a supersaturated state it is no longer possible to use V to monitor the charging level of the main part of the 2D electron system localized on the liquid substrate d. For this reason, the standard procedure for estimating n_s, where V is given and then the cell is charged up to saturation (i.e., up to density n_s (2)), in reality leaves n_s arbitrary. To estimate the fractions n_d and n_t, additional information is required about the behavior of the 2D electron system in a supersaturated state.

2. One of the standard channels for obtaining information on the density n_s is to measure the capacitance of a cell with 2D electrons. In the present model of an infinite 2D system, the question is the behavior of the derivative dE_-/dV, which determines the change in the charge on the bottom plate as a result of variation of V with n_s fixed. This derivative undergoes a jump at a transition from the situation (1) to the supersaturated state (4)

$$\frac{dE_-/dV_{|V>V_s}}{dE_-/dV_{|V<V_s}} = \frac{d+\delta}{d+h}. \tag{7}$$

Therefore, the capacitance of the cell changes abruptly at the point V_s (it increases in the present case), and this circumstance can be used for diagnostics of a 2D system on helium.

3. We shall now say a few words about the role of image forces in the supersaturation problem. For values of δ of the order of 10^{-6} cm, the image energy

$$U_t = -e^2/4\delta \tag{8}$$

is of the order of 500 K (together with possible correlation corrections). Under these conditions, the purely electrostatic equilibrium between the fractions n_d and n_t, which was discussed above, needs to be corrected. Instead of equipotentiality of the gap between the two electron layers, which was used above, it is natural to require that the electrochemical potentials of these fractions be equal or, equivalently,

$$U_t + e\varphi_t + T\ln n_t = U_d + e\varphi_d + T\ln n_d, \tag{9}$$

where the corresponding electric potentials φ_t and φ_d are taken from the solution of the electrostatic problem for a layered system with two densities: n_t and n_d on the films δ and d and an external potential difference V between the capacitor plates.

Taking account of the scale of the energies U_t and U_d and the typical liquid-helium temperatures $T \leqslant 1$ K, in most cases the entropy contributions in Eq. (9) can be neglected, so that

$$e\varphi_t - e\varphi_d \simeq U_d - U_t. \tag{10}$$

This relation illustrates the level of external action on the system of electrons required to maintain the fraction n_d at least in a partially filled state.

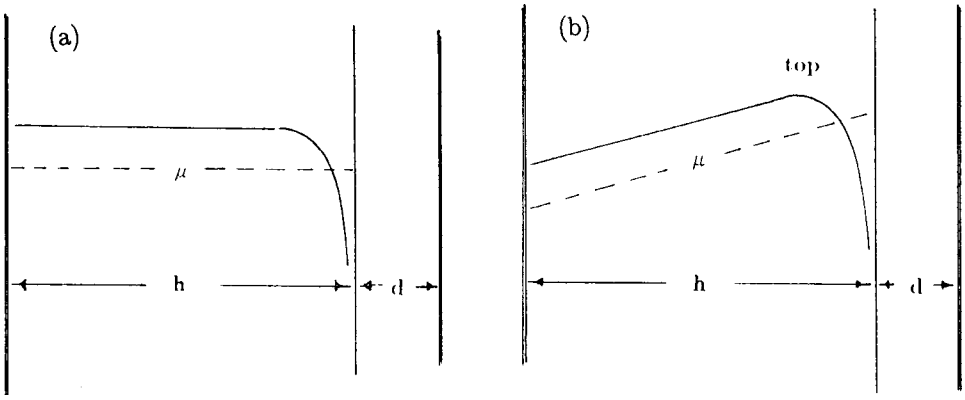

FIG. 2. Energy schemes for the one -component model: a — saturated state, being the boundary of stability for the one -component filling model; in this state it is still possible to talk about equilibrium, so that the electrochemical potential μ is represented by a constant along the cell; b — supersaturation in the one-component approximation; a small (compared with the situation *a*) slope μ leads to the appearance of a nonequilibrium supersaturated state with the top barrier *top*, arising as a result of competition between the electrostatic energy and the potential of the image forces, located near the film *d*.

But, in general, it is Eq. (9) that gives a complete representation of equilibrium between the electron subsystems in the supersaturation state. Specifically, it is now clear that the two-component nature of the system is the dominant property for electrons localized above helium.

The field distribution replacing Eq. (1) is

$$E_- = \Delta^{-1}[4\pi e(n_d h + n_s \delta) - V], \quad -d \leqslant x \leqslant 0, \tag{11}$$

$$E_+ = \Delta^{-1}[4\pi e(n_t \delta - n_d d) - V], \quad 0 \leqslant x \leqslant h, \tag{11a}$$

$$E_\delta = -\Delta^{-1}[4\pi e n_t(h+d) + 4\pi e n_d d - V], \quad h \leqslant x \leqslant h+\delta, \tag{11b}$$

$$\Delta = h + d + \delta.$$

It is easy to see that as $\delta \to 0$ and $n_d \to n_s$ Eqs. (11) transform into Eq. (1). The electric potentials corresponding to the fields (11),

$$\varphi_d = E_- d + V, \quad \varphi_t = E_\delta h + (4\pi e n_s - E_-)(h+\delta) \tag{12}$$

together with the requirement $n_s = n_t + n_d$ contain one undetermined constant (for example, n_d), whose value is found from Eq. (9) or (11) using Eq. (12).

From the experimental standpoint, the most interesting effect of image forces on the structure of supersaturated states should appear in various kinetic effects with respect to the destruction of the n_d component. The existing measurement schemes[2–6] proceed from the assumption that a saturated state (2) exists and a small perturbation of this state gives rise to an electron current from the helium surface into the vacuum. The top of the barrier overcome by the 2D electrons lies near the main vapor–liquid boundary (see Fig. 2). In the problem with two 2D systems, the maximum of the effective potential is virtually always located near the δ layer (see Fig. 3). Therefore its characteristics are determined largely by the equilibrium parameters of the corresponding supersaturated state — a

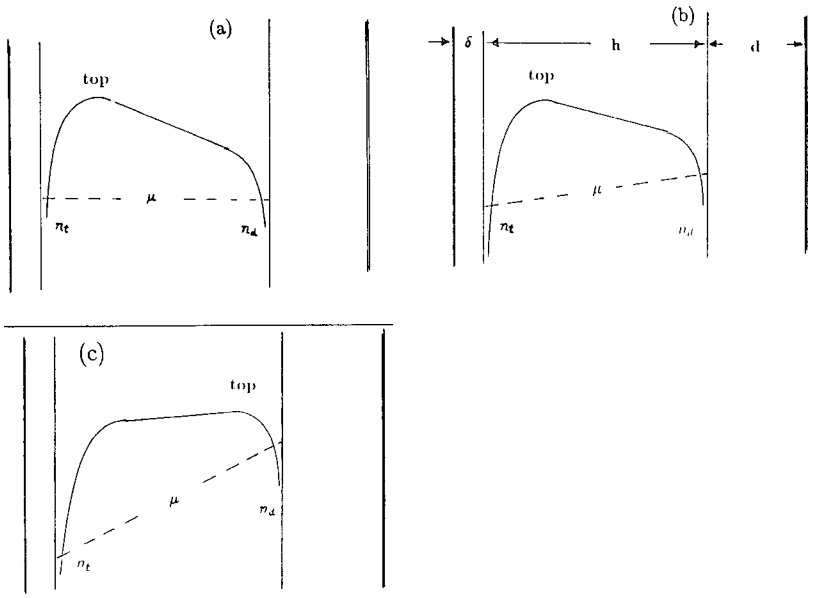

FIG. 3. Energy schemes for a two-component model: a — One of the supersaturated states with finite densities n_d and n_t; according to Eq. (10), for a two-component supersaturated equilibrium state with $\mu =$ const a nonzero electrostatic field, leading in combination with the fields of image forces to the appearance of an energy maximum *top* near the film δ, is characteristic. b — Small perturbation of the state a, stimulating the restructuring of the components n_d and n_t. The saddle point *top* is once again located near the δ layer. c — Strong perturbation of the state a, for which a saddle-point approximation to the film d is possible.

factor which thus far has been neglected in discussions of experiments on the kinetics of the evaporation of electrons from a helium surface.

In conclusion, we note that taking into account the superfluidity of helium, specifically, the capability of helium to cover with a thin film all inner surfaces of the cells used for studying the properties of surface electrons, leads to a number of unique effects in the filling of surface states by electrons. It becomes necessary to introduce a two-component 2D electron system. One of these components on the film d is active and serves as a subject of various investigations. The other one (on the film δ) is mainly passive, being strongly localized in the vertical direction and almost stationary in the horizontal direction. Nonetheless its presence appreciably influences the equilibrium characteristics of the overall 2D system.

This work was partially supported by the Russian Fund for Fundamental Research (Grant No. 98-02-16640) and INTAS (Grant Network 97-1643).

[1] V. B. Shikin and Yu. P. Monarkha, *Two-Dimensional Charged Sytems in Helium* (Nauka, Moscow, 1989).
[2] Y. Iye, K. Kono, K. Kajita, and W. Sasaki, J. Low Temp. Phys. **34**, 539 (1979).
[3] Y. Iye, K. Kono, K. Kajita, and W. Sasaki, J. Low Temp. Phys. **38**, 293 (1980).
[4] K. Kono, K. Kajita, K. Kobayashi, and W. Sasaki, Surf. Sci. **113**, 438 (1982).
[5] E. Andrei, S. Yegel, and L. Menna, Phys. Rev. Lett. **67**, 3704 (1991).
[6] L. Menna, S. Yucel, and E. Andrei, Phys. Rev. Lett. **70**, 2154 (1993).

Translated by M. E. Alferieff

Optical phonon spectrum of germanium quantum dots

A. B. Talochkin,*) V. A. Markov, A. I. Nikiforov, and S. A. Tiĭs
Institute of Semiconductor Physics, Siberian Branch of the Russian Academy of Sciences, 630090 Novosibirsk, Russia

(Submitted 1 July 1999)
Pis'ma Zh. Éksp. Teor. Fiz. **70**, No. 4, 279–283 (25 August 1999)

We have observed additional lines, shifted in both directions relative to the frequency of the bulk phonon of Ge, in the Raman scattering spectra from optical phonons in germanium quantum dots. The observed phonon modes are shown to be due to the straining of the quantum dots as a result of the lattice mismatch of the Ge and Si matrices. The observed frequency shifts, with allowance for optical-phonon localization effects, make it possible to determine the sizes of the regions with different strain states in the quantum dots. © *1999 American Institute of Physics.* [S0021-3640(99)01016-6]

PACS numbers: 78.30.Am, 73.20.Dj, 68.65.+g

The production of semiconductor quantum dots (QDs) using molecular-beam epitaxy (MBE) is based on self-matched growth by the Stranski–Krastanov mechanism.[1,2] It arises when as a result of mechanical stresses due to the lattice mismatch of the QD and substrate materials, the two-dimensional film decomposes, and self-matched growth of three-dimensional islands continues. This system of islands is usually covered over by the substrate material. The quantum dots obtained in such a process are highly strained. The strain of InAs QDs grown in GaAs reaches 7%,[2] and for Ge QDs in Si it is 4%.[1] Such high strains lead to strong shifts of the spectrum of electronic states of QDs and to changes in other parameters.[3] The theoretical calculations performed in Ref. 3 for InAs QDs in GaAs predict a nonuniform distribution of strain in QDs. As a result of the action of two force components — from the substrate side and from the matrix covering the QD — the strain depends on the distance to the base of the QD and at some height it vanishes and changes sign.[3] We know of no experiments in which the strain state of QDs are investigated. In the present work, the Raman scattering method was used to investigate the optical phonon spectrum of Ge QDs obtained by MBE in a Si matrix. Since in the present system (Ge/Si) optical phonons are strongly localized and their frequency depends linearly on the strain, it was possible to reconstruct the strain state of Ge QDs according to the observed frequency shifts.

The experimental samples consisted of Si/Ge/Si structures with Ge QDs and were obtained by MBE. KÉF-0.01 Si substrates with (001) orientation were used. The QD layer was grown on a 1000 Å thick Si buffer with substrate temperature 150–200 °C. The relatively low growth temperature of Ge gives QD sizes ~100 Å in the growth plane and an ideally sharp Ge/Si interface.[4] Two-dimensional growth occurs with effective Ge thickness $d<4$ monatomic layers (ML) (1 ML=1.3 Å). Next, for $4<d<12$ ML, Ge

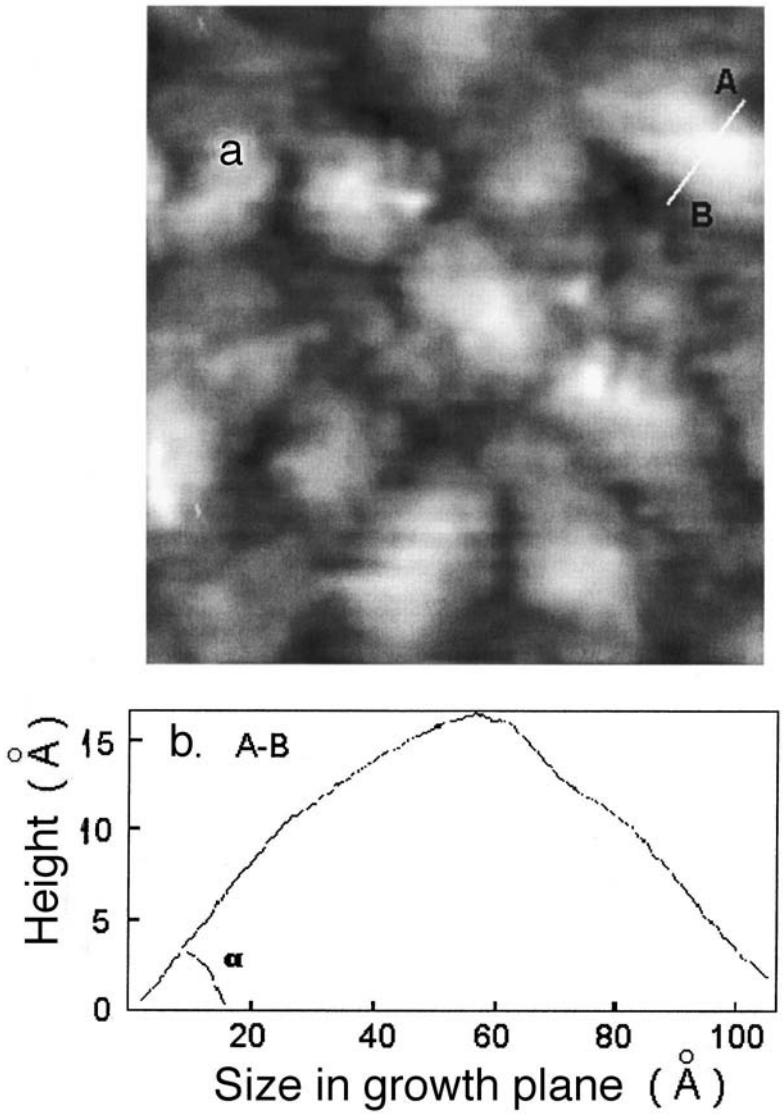

FIG. 1. Scanning tunneling microscope image of the surface (500×500 Å) of a sample with Ge quantum dots: a, b — transverse profile obtained along the line A–B.

grows in the form of isolated pyramidal islands. For $d=12$ ML the QDs join at the bases and form a continuous layer, and relaxation of mechanical stresses, which is due to the formation of a mismatch at the interface of the dislocations, starts at $d=15$ ML. See Refs. 5 and 6 for a detailed discussion of these structures. The sizes and shapes of the QDs were measured with a RIBER-OMICRON scanning tunneling microscope on samples which were not specially coated with a Si layer. Figure 1a shows an image of a 500 ×500 Å area of a sample with effective Ge thickness of 8 ML. The image was obtained using a scanning tunneling microscope with a 0.2 nA tunneling current. A profile mea-

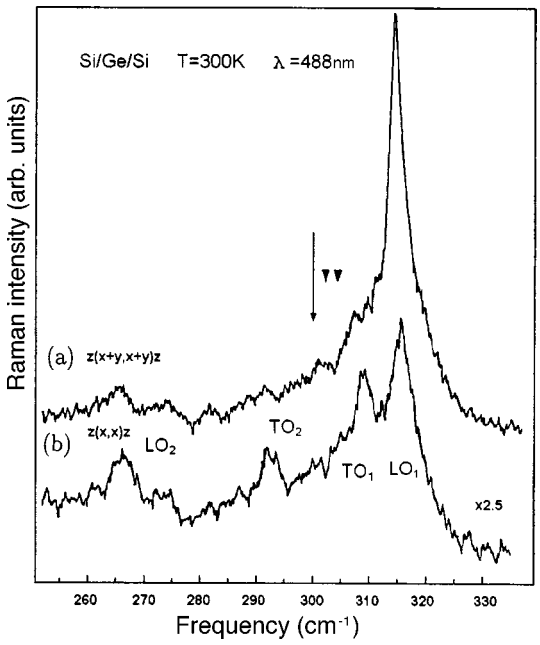

FIG. 2. Raman spectra from optical phonons of Ge QDs. The spectra were obtained at $T=300$ K using $\lambda=488$ nm in two polarization geometries. The arrow marks the position of the frequency of the bulk phonon of Ge, the triangles mark the positions of the LO and TO phonons when the strain in region *2* of the QD is taken into account.

sured along the line $A-B$ is displayed at the bottom of Fig. 1b. It is evident that the characteristic height of the Ge QDs is 15 Å , and a pyramid base in the growth plane is ~ 100 Å in size. The angle between the base and the lateral faces is $\alpha=17°$.

The Raman scattering spectra for optical phonons were excited by Ar laser lines at sample temperatures 300 and 77 K and recorded with a DFS-52 spectrometer. Figure 2 shows the spectra measured in backscattering geometry on a sample with effective Ge layer thickness 8 ML at $T=300$ K. The spectra were obtained in two polarization geometries: $z(x+y,x+y)z$ and $z(x,x)z$, where z is (001), x is (100), and y is (010). According to the polarization selection rules for scattering by Ge optical phonons, which are determined by the form of the Raman scattering tensor, for reflection from a (001) surface only LO phonons are active in the $z(x+y,x+y)z$ geometry.[7] Scattering by TO phonons is forbidden. It is evident from Fig. 2a that in the allowed geometry an intense peak due to an LO phonon of a Ge QD appears. The intensity of the peak increases when the spectrum is excited near the E_0 resonance of a QD (2.4–2.6 eV), which is due to direct optical transitions between Γ_2 and Γ_{25} states of a Ge quantum dot, and its energy is determined by the size of the QD.[6] The high intensity of the LO peak in the allowed geometry masks the weak lines of the other phonon modes, which can be observed in the forbidden geometry $z(x,x)z$ (Fig. 2b). It is evident from Fig. 2b that in this geometry the LO phonon intensity decreases by a factor of 5 and additional lines with frequencies 266, 292, and 309 cm^{-1} are observed. In Fig. 2 the arrow shows the position of the bulk phonon of Ge. The two peaks (LO_1 and TO_1) are shifted relative to it into the high-

frequency region, and the other two (LO_2 and TO_2) are shifted in the direction of low frequencies.

The series of lines found is observed in samples where the QDs are isolated from one another (4 ML $< d <$ 12 ML) or join together into a continuous layer ($d = 12$ ML) without a change in the stress state of Ge.[4] In samples where relaxation of mechanical stresses starts ($d = 15$ ML), the main phonon peak (LO_1) shifts in the direction of the bulk position and becomes wider, while the other lines are no longer present in the spectra. As a result, the observed phonon spectrum could be due to a distribution of the mechanical stresses in a Ge QD.

Let us consider the deformations of a Ge QD and their effect on the optical phonon spectrum. The mismatch of the Ge and Si lattice constants is $\Delta a/a = 0.04$. As a result, a thin Ge film obtained pseudomorphically to a Si substrate (i.e., with an ideally sharp interface without introduction of defects and intermixing of the materials) is deformed along two axes in the (001) growth plane. The components of the strain tensor are $\epsilon_{xx} = \epsilon_{yy} = -0.04$. From the boundary condition for a free film surface $\sigma_{zz} = 0$ (σ_{zz} is a component of the stress tensor) we find $\epsilon_{zz} = -(2c_{12}/c_{11}) = 0.03$, where c_{12} and c_{11} are components of the elasticity tensor of Ge. Biaxial compressive strain in the xy plane results in stretching of Ge in the z direction. Such a stressed state shifts and splits the LO and TO phonon frequencies, which in bulk Ge are degenerate at $k = 0$. The strain-induced changes in the LO and TO phonon frequencies are determined by the expressions[8]

$$\Delta\omega^L = [p\epsilon_{zz} + q(\epsilon_{xx} + \epsilon_{yy})]/2\omega_0^2, \tag{1}$$

$$\Delta\omega^T = [p\epsilon_{xx} + q(\epsilon_{zz} + \epsilon_{yy})]/2\omega_0^2, \tag{2}$$

where ω_0 is the frequency of optical phonons in Ge for $k = 0$, and p and q are the components of the tensor of anharmonic constants of Ge: $p = -0.73(2\omega_0^2)$, $q = -0.96(2\omega_0^2)$. For deformation of a pseudomorphic Ge film, expressions (1) and (2) lead to frequency shifts $\Delta\omega_1^L = 16.5$ cm^{-1} and $\Delta\omega_1^T = 11$ cm^{-1}. The observed shifts of the LO_1 and TO_1 lines relative to the bulk frequency of Ge are 16 and 9 cm^{-1} (Fig. 2b), respectively. These values are in complete agreement with the values computed taking account of the fact that the experimental position of TO_1 line is somewhat shifted into the region of low frequencies because of the presence of a strong close-lying line (LO_1). As a result, the Raman lines LO_1 and TO_1 are due to scattering by phonons localized in the region of a QD near the Si substrate, whose deformation is identical to the state of the pseudomorphic Ge film. The other two, LO_2 and TO_2, shifted into the region of low frequencies (Fig. 2b), are due to phonons localized near the apexes of the QDs.

Figure 3a shows a diagram of the cross section of a QD, which is divided by the dashed line into two regions — *1* and *2*. In the first region, the average strain determining the phonon frequencies is similar to a pseudomorphic Ge film. In region *2* of height h, the components of the strain tensor compared with region *1* change sign because the Si matrix covering the Ge compresses the QD in the z direction. As the distance from the substrate increases, this force component increases, and the compression component in the growth plane on the substrate side decreases. As a result, the strain vanishes in the plane marked in Fig. 3a by the dashed line, and in region *2* it changes sign. Figure 3b

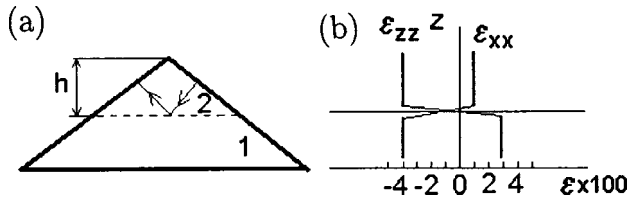

FIG. 3. Diagram of the transverse cross section of a Ge quantum dot. a, b — Average (in regions *1* and *2*) strain tensor components ϵ_{xx} and ϵ_{zz} as functions of the coordinate *z*.

shows the average values (in regions *1* and *2*) of the strain tensor components ϵ_{xx} and ϵ_{zz} as a function of the coordinate *z*. The scheme presented explains the results of the numerical calculation performed for InAs QDs in GaAs.[3]

Since in region *2* the components of the strain tensor are $\epsilon_{zz}=-0.04$, $\epsilon_{xx}=\epsilon_{yy}=-(c_{12}/[c_{11}+c_{12}])$, and $\epsilon_{zz}=0.011$, the frequency shifts of the *LO* and *TO* phonons can be found from expressions (1) and (2): $\Delta\omega_2^T=4.8$ cm^{-1} and $\Delta\omega_2^T=2.5$ cm^{-1}. The positions of the Raman lines corresponding to these shifts are shown in Fig. 2b (triangles). The difference of the optical phonon frequencies in regions *1* and *2*, which is due to the difference of the mechanical stresses in them, leads to phonon localization (i.e., phonons are elastically reflected from the interface as a result of the fact that the amplitude of the optical oscillations decays sharply in the neighboring region). It is evident from Fig. 2b that the LO_2 and TO_2 phonon lines in region *2* are shifted by 37 and 13 cm, respectively, to lower frequencies from the positions determined by the strain.

We attribute the observed low-frequency shift of the LO_2 and TO_2 lines to size quantization of the phonon spectrum in region 2 of a QD. The two faces of the pyramid and the interface of regions *1* and *2*, from which the phonons are elastically reflected, form a cavity (Fig. 3a). The minimum wave number *q* of the phonons excited in it, which are detected in Raman scattering, is determined by the condition for the existence of a standing wave $2h\cos\alpha=\pi/q$. The resonance trajectory of phonons is shown in region *2* by the arrows (Fig. 3a) that are perpendicular to the lateral faces. Using the bulk dispersion relations for phonons,[9,10] we find that the observed frequency shifts for LO_2 (37 cm) and for TO_2 (13 cm) phonons correspond to the wave number $q=0.7/a$, where *a* is the lattice constant of Ge. Hence the height of region 2 is $h=4$ Å . As a result of compression forces exerted on the Ge QDS by the Si matrix, the QDs consist of two regions, 4 and 11 Å high, with a different strain state.

We note that for InAs QDs the strain changes sign at one-half the height of the pyramid,[3] while in our case the ratio of the heights of the regions is $\sim 1:3$. This is due to the different form of the QDs: The angle at the base of an InAs QD is 45°,[3] while for a Ge QD $\alpha=17°$. As a result, in our case the compression force component exerted by the substrate maintains a larger height of Ge in the pseudomorphic state, and the components of the strain tensor change sign farther from the base of the QD than for an InAs QD.

In summary, the phonon spectrum of Ge QDs investigated is explained by the fact that the QDs consist of two regions with a different strain state. One region near the Si substrate is deformed similarly to a pseudomorphic film, while in the second region the components of the strain tensor change sign. The observed low-frequency shift of the *LO* and *TO* phonon lines in the second region, which is due to size quantization of the

phonons, made it possible to determine the characteristic dimensions of the QD regions with different strain states.

This work was supported by the Russian Fund for Fundamental Research (Grant No. 98-02-16984).

*)e-mail: tal@thermo.isp.nsc.ru

[1] Y.-W. Mo, D. E. Savage, B. S. Swartzentruber, and M. G. Lagally, Phys. Rev. Lett. **65**, 1020 (1990).
[2] H. Drexler, D. Leonard, W. Hansen *et al.*, Phys. Rev. Lett. **73**, 2252 (1994).
[3] M. Grundman, O. Stier, and D. Bimberg, Phys. Rev. B **52**, 11969 (1995).
[4] A. B. Talochkin, A. V. Efanov, V. A. Markov, S. P. Suprun, and A. I. Nikiforov, Izv. Akad. Nauk, Ser. Fiz. **63**, 290 (1999).
[5] V. A. Markov, A. I. Nikiforov, and O. P. Pchelyakov, J. Cryst. Growth **157**, 260 (1997).
[6] A. B. Talochkin, V. A. Markov, S. P. Suprun, and A. I. Nikiforov, JETP Lett. **64**, 219 (1996).
[7] M. Cardona and G. Guntherodt (eds.), *Light Scattering in Solids*, Vol. 2 (Springer-Verlag, New York, 1982) [Russian translation, Mir, Moscow, 1984, Part 2].
[8] F. Cerdeira, C. J. Buchenauer, F. H. Pollak, and M. Cardona, Phys. Rev. B **5**, 580 (1972).
[9] E. Friess, K. Eberl, U. Menczigar, and G. Abstreiter, Solid State Commun. **73**, 203 (1990).
[10] Weber, Phys. Rev. B **15**, 4789 (1977).

Translated by M. E. Alferieff

Dependence of the resistivity of nonstoichiometric titanium carbide TiC_y on the density and distribution of carbon vacancies

V. N. Lipatnikov*) and A. I. Gusev†)
Institute of Solid-State Chemistry, Urals Branch of the Russian Academy of Sciences, 620219 Ekaterinburg, Russia

(Submitted 23 June 1999; resubmitted 6 July 1999)
Pis'ma Zh. Éksp. Teor. Fiz. **70**, No. 4, 284–289 (25 August 1999)

The influence of temperature and of the density and distribution of structural vacancies in the carbon sublattice on the resistivity of nonstoichiometric titanium carbide TiC_y ($0.5 \leqslant y \leqslant 0.98$) is studied. It is shown that in titanium carbide TiC_y with $y < 0.7$ reversible disorder–order structural phase transitions occur at temperatures below 1000 K. The temperatures of order–disorder phase transformations are determined. The dependence of the residual resistivity on the composition of the disordered titanium carbide is explained by the change in the carrier density in the region of homogeneity of the carbide TiC_y, on the one hand, and the atom–vacancy interaction, on the other. © *1999 American Institute of Physics.* [S0021-3640(99)01116-0]

PACS numbers: 72.80.Sk, 61.72.Ji, 81.05.Je, 81.30.Hd

Titanium carbide TiC_y with structural basis of the type $B1$ (NaCl) is a highly nonstoichiometric compound.[1–3] Disordered titanium carbide TiC_y ($TiC_y\square_{1-y}$) possesses an exceedingly wide region of homogeneity — from $TiC_{0.48}$ to $TiC_{1.00}$ (Ref. 1), where the carbon atoms C and the structural vacancies $\square$ form a solution of substitution in the nonmetallic sublattice. The high density of structural vacancies creates the prerequisites for ordering of TiC_y carbide. The atom–vacancy ordering appreciably influences the structure and the properties of highly nonstoichiometric carbides MC_y (Refs. 1 and 4).

The effect of nonstoichiometry on the electrokinetic properties of disordered titanium carbide has been investigated repeatedly,[5–8] but the effects due to ordering have been little studied. We mention Refs. 9 and 10, where in a narrow range of compositions of TiC_y ($0.51 < y < 0.65$), a jump-like change in ρ, tentatively attributed to order–disorder transitions, was observed in the temperature dependences of the resistivity $\rho(T)$ in the temperature range 800–1000 K. However, the crystal structure of the titanium carbide was not studied in Refs. 9 and 10, so that the results obtained there give only an indirect indication of the structural transformations occurring in the nonstoichiometric carbide TiC_y.

At the same time, calculations performed by the order parameter functional method[1,11] and by the Monte Carlo method[12] show that on ordering of the TiC_y carbide in the range $TiC_{0.50}$– $TiC_{0.70}$ the superstructures Ti_2C and Ti_3C_2, with transition tem-

peratures not exceeding 1000 K can arise. In this connection, in the present work the resistivity of titanium carbide TiC_y, which is very sensitive to structural phase transformations, is studied in a wide temperature range in the entire homogeneity region of TiC_y.

The samples of nonstoichiometric titanium carbide TiC_y ($0.50 \leqslant y \leqslant 0.98$) were synthesized by hot pressing of powder mixtures of $TiC_{0.98}$ and metallic titanium in highly pure argon gas at temperatures 1800–2000 K and pressing pressures 23–25 MPa. The composition of the samples obtained and the impurity content were determined by chemical and spectral analyses; the oxygen and nitrogen impurity contents did not exceed 0.14 and 0.07 mass %, respectively, and the total content of metallic impurities did not exceed 0.02 mass %. The phase composition and crystal structure of the synthesized TiC_y samples and the same samples after annealing or measurements of the resistivity were studied by x-ray diffraction in CuK_α radiation in a stepped scanning mode with $\Delta 2\theta = 0.02°$ for angles 2θ ranging from 14° to 130°; for measurements on annealed carbides, the exposure time at each point was 5 s. All synthesized samples were homogeneous and contained only a disordered TiC_y phase with $B1$ (NaCl) structure.

To achieve a disordered state, the synthesized samples were annealed for 340 h with the temperature lowered gradually from 1070 to 770 K; cooling from 770 to 300 K was done at a rate of 1 $K \cdot min^{-1}$. Annealing resulted in the appearance of superstructural reflections in the x-ray diffraction patterns of the carbides TiC_y with a relative carbon content y from 0.50 to 0.67. Analysis of the diffraction data, which we described earlier,[13,14] showed that as a result of annealing, cubic (space group $Fd3m$) and trigonal (space group $R\bar{3}m$) superstructures of the type Ti_2C and the orthorhombic (space group $C222_1$) superstructure Ti_3C_2, respectively, form in the concentration intervals $TiC_{0.49-0.51}-TiC_{0.54-0.55}$, $TiC_{0.55}-TiC_{0.59}$, and $TiC_{0.63}-TiC_{0.67}$. In the interval $TiC_{0.59}-TiC_{0.63}$, a mixture of two ordered phases Ti_2C (space group $R\bar{3}m$) + Ti_3C_2 (space group $C222_1$) forms as a result of annealing.

The resistivity measurements were performed by the four-contact method in vacuum not worse than 0.0013 Pa (1×10^{-5} torr). The resistance was measured in the temperature range 300–1200 K with a 1 K step, and the current passed through the sample was 20 and 100 mA. The relative error in measuring ρ did not exceed 0.5%, and the sample temperature during the measurements was maintained to within 0.2 K. The average rates of heating and cooling were 1 $K \cdot min^{-1}$. The porosity P of the samples was not less than 1%, so that corrections for P were not made in the resistivity measurements. The resistance was measured on TiC_y carbide samples in a quenched disordered state and in an ordered state obtained by annealing.

The temperature dependences of the resistivity $\rho(T)$ of the experimental samples of nonstoichiometric titanium carbide TiC_y are shown, in part, in Figs. 1 and 2.

Measurements of the resistivity ρ of the quenched disordered carbide $TiC_{0.52}$ revealed that an increase in temperature to $\sim$500 K is accompanied by the standard increase in ρ as a result of scattering of carriers by phonons. An anomalous decrease of ρ due to an irreversible transition from a nonequilibrium disordered state into an equilibrium ordered state is observed at $T \approx 815$ K (Fig. 1, curve *1*). A further increase of temperature to 960 K is accompanied by a jump in ρ in the range 960–1030 K as a result of a transition from an equilibrium ordered state into an equilibrium disordered state and then slow growth of the resistivity (Fig. 1, curve *1*). On cooling the resistivity decreases

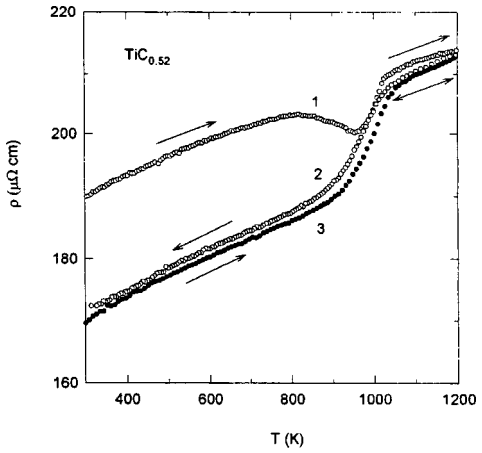

FIG. 1. Effect of ordering on the resistivity ρ of the nonstoichiometric carbide $TiC_{0.52}$: *1* — $\rho(T)$ of the disordered carbide $TiC_{0.52}$ on heating and the nonequilibrium disorder → order transition; *2* — change in ρ on cooling and the equilibrium disorder ↔ order transition; *3* — change in ρ on heating of the ordered carbide $TiC_{0.52}$.

(Fig. 1, curve *2*), the decrease being abrupt in the range 900–1020 K. Upon subsequent heating of the ordered carbide $TiC_{0.52}$, the resistivity ρ varies along the curve *3*, which is similar to the curve *2* (Fig. 1).

The $\rho(T)$ curves (Fig. 1, curves *2* and *3*) are characteristic for an equilibrium reversible disordered–ordered transition. Hysteresis of the resistivity is observed near the transition. The formation of an ordered phase of the type Ti_2C in the $TiC_{0.52}$ sample accompanying a change in ρ is confirmed by the presence of the same superstructural reflections in its diffraction spectrum as after prolonged annealing of the $TiC_{0.52}$ sample.

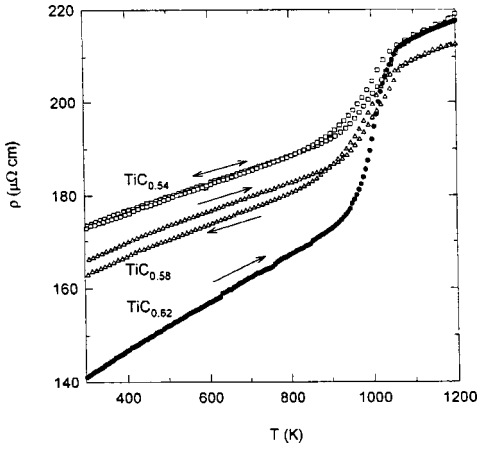

FIG. 2. Reversible variation of the resistivity of the ordered carbides $TiC_{0.54}$, $TiC_{0.58}$, and $TiC_{0.62}$ on heating, the order ↔ disorder transition and cooling.

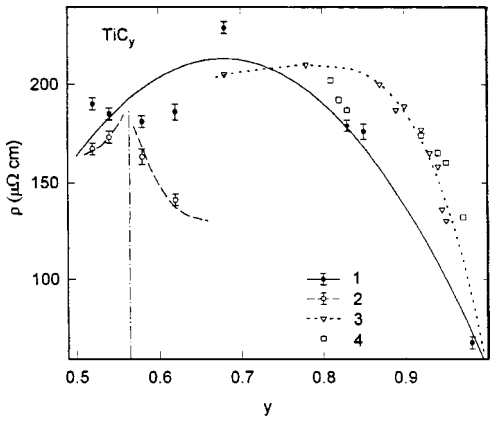

FIG. 3. Resistivity ρ versus the composition of titanium carbide TiC_y at 300 K in the disordered (*1*) and ordered (*2*) states; *3* and *4* — resistivity of the disordered carbide TiC_y at 300 K according to the data of Refs. 8 and 5, respectively. The dot-dashed line shows the position of the boundary between the ordered phases Ti_2C and Ti_3C_2.

Figure 2 shows $\rho(T)$ measured in the carbides $TiC_{0.54}$, $TiC_{0.58}$, and $TiC_{0.62}$ ordered by means of annealing. At temperatures $940<T<1060$ K jump-like change and hysteresis of the resistivity, which are associated with a reversible order–disorder transition, are observed in the dependences $\rho(T)$. The additional resistivity $\Delta\rho$ due to disordering is 15–20 $\mu\Omega\cdot$cm for the transition $TiC_y \leftrightarrow Ti_2C$ and 25–40 $\mu\Omega\cdot$cm for the transition $TiC_y \leftrightarrow Ti_3C_2$. The presence of hysteresis indicates that the transitions TiC_y $(0.52 \leqslant y \leqslant 0.57) \leftrightarrow Ti_2C$ and TiC_y $(0.58 \leqslant y \leqslant 0.68) \leftrightarrow Ti_3C_2$ are close to first-order transitions. The conclusion that the transition is of first order was also made in Ref. 9, though on the basis of symmetry considerations[14,15] this transformation satisfies Landau's criterion for second-order phase transitions. All this, together with the data in Ref. 14 on the variation of the specific heat near the transition temperature T_{trans}, suggests that the reversible order–disorder transformation $TiC_y \leftrightarrow Ti_2C$ can be regarded as a weak first-order phase transition with a low latent heat of transformation.

Only very weak hysteresis of ρ in the range 770–880 K and a clear increase of $\partial\rho/\partial T$ at $T \approx 940$ K are observed in $\rho(T)$ of the annealed carbide $TiC_{0.68}$. It can be inferred that prolonged annealing made it possible to obtain in the carbide $TiC_{0.68}$ a very low degree of ordering, since according to composition this carbide lies near or on the boundary of the region of homogeneity of the ordered phase Ti_3C_2. A kink due to the abrupt growth of $\partial\rho/\partial T$ from 0.024 to 4 to 0.030 $\mu\Omega\cdot$ cm$\cdot$K^{-1} is observed in $\rho(T)$ of the annealed carbide $TiC_{0.83}$ at $T \approx 1040$ K. This weak effect seems to be due to the initial stage of formation of order as a result of annealing of the carbide $TiC_{0.83}$. The resistivity of the annealed carbides $TiC_{0.85}$ and $TiC_{0.98}$ on heating and cooling changes without any characteristic features.

Figure 3 shows the resistivity as a function of the composition of the carbide TiC_y at 300 K. As the concentration of structural vacancies decreases and the carbon content y increases from 0.52 to 0.98, the resistivity of the disordered carbide TiC_y at first increases, passes through a maximum at $y=0.68$, and then decreases.

Ordered carbides have a lower resistivity than disordered carbides with the same composition. The decrease found in resistivity $\Delta\rho(y,300)$ of the carbide $TiC_{0.62}$ on ordering is ~ 40 $\mu\Omega\cdot$cm ($\sim 24\%$); according to Ref. 16, for $TiC_{0.625}$ $\Delta\rho(300)\approx 20$ $\mu\Omega\cdot$cm ($\sim 10\%$), indicating that in Ref. 16 the degree of ordering achieved was lower. Two sections corresponding to the regions of existence of the ordered phases Ti_2C and Ti_3C can be distinguished in the dependence $\rho(y,300)$ for the ordered carbide TiC_y. On each section, as y varies, the resistivity $\rho(y,300)$ approaches a minimum value corresponding to the stoichiometric composition of the ordered phase. Thus, in the region of homogeneity of the phase Ti_2C the resistivity $\rho(y,300)$ decreases as $y\rightarrow 0.5$, and in the region of homogeneity of the phase Ti_3C_2 the resistivity $\rho(y,300)$ decreases as y changes from a value corresponding to the lower limit of the region of homogeneity ($y\approx 0.58$) to $y=2/3$ (Fig. 3). Judging from the dependences $\rho(y,300)$ for ordered phases of titanium carbide, the boundary between the region of homogeneity of the phase Ti_2C and the two-phase region ($Ti_2C+Ti_3C_2$) corresponds to $y\approx 0.58-0.59$.

The dependence $\rho(y,300)$ found for the disordered carbide TiC_y agrees fairly well with published data. For comparison, the dependences $\rho(y,300)$ measured in Refs. 5 and 8 on disordered titanium carbide single crystals with different composition are shown in Fig. 3. All measurements show that any deviation of the titanium carbide composition from stoichiometry is accompanied by rapid growth of the resistivity: According to Refs. 5 and 8, in the region $TiC_{0.95}-TiC_{1.00}$ $\partial\rho/\partial y\sim 24$ $\mu\Omega\cdot$cmper 1 at.% vacancies and according to the results of the present work approximately $\partial\rho/\partial y\sim 14$ $\mu\Omega\cdot$cm per 1 at.% vacancies. Since the residual resistivity $\rho(0)$ of stoichiometric carbide $TiC_{1.00}$ is close to zero, this means that scattering in titanium carbide occurs mainly by structural vacancies.

The temperature coefficient of resistivity $\partial\rho/\partial T$ is small and changes very little from 0.05 to 0.03 $\mu\Omega\cdot\text{cm}\cdot\text{K}^{-1}$ from $TiC_{0.52}$ to $TiC_{0.62}$ and then it increases to 0.06 $\mu\Omega\cdot\text{cm}\cdot\text{K}^{-1}$ for $TiC_{0.98}$. This is quite close to the data of Ref. 8, according to which $\partial\rho/\partial T$ changes from 0.05 $\mu\Omega\cdot\text{cm}\cdot\text{K}^{-1}$ for $TiC_{0.95}$ to 0.15 $\mu\Omega\cdot\text{cm}\cdot\text{K}^{-1}$ for $TiC_{0.78}$ and then increases to 0.03 $\mu\Omega\cdot\text{cm}\cdot\text{K}^{-1}$ for $TiC_{0.68}$. When the value of $\partial\rho/\partial T$ is taken into account, the concentration dependence of the residual (at $T=4.2$ K) resistivity $\rho_{res}(y)$ of the disordered carbide TiC_y (Fig. 4, curve *1*) is similar to $\rho(y,300)$. The conductivity in nonstoichiometric titanium carbide is predominantly of an electronic character, and the character of its variation with the content of the structural vacancies in the carbon sublattice indicates that the carrier density depends on the content of structural vacancies. In this case, the residual resistivity of the disordered carbide TiC_y can be described using Nordheim's rule, which takes the atom–vacancy and electron–vacancy interactions into account, in the form $\rho_{res}(y)=Ay(1-y)/n(y)$, where A is a proportionality constant and n is the carrier (conduction electron) density. To a first approximation, the carrier density n is proportional to $[N(E_F)]^3$, where $N(E_F)$ is the electronic density of states at the Fermi level. Hence it follows that the dependence of the residual resistivity on the composition of the disordered carbide TiC_y has the form

$$\rho_{res}(y)\sim Ay(1-y)/[N(E_F)(y)]^3. \quad (1)$$

A calculation of the electronic structure of nonstoichiometric titanium carbide, performed by the Korringa–Kohn–Rostoker method in the coherent potential approximation (KKR–CPA),[17] showed that as the vacancy concentration $(1-y)$ increases from 0 to 0.5,

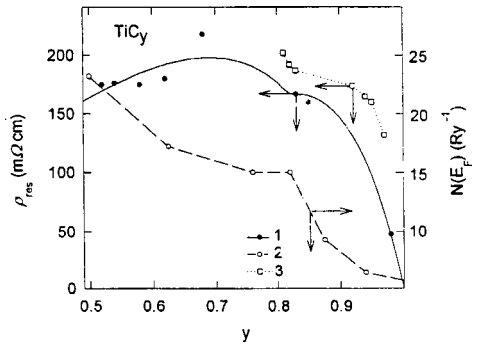

FIG. 4. Residual resistivity $\rho_{\text{res}}(y)$ (1) at 4.2 K and the electron density of states at the Fermi level $N(E_F)$ (2) as functions of the composition of the disordered titanium carbide TiC_y. Curve *1* was calculated by the least-squares method based on the experimental data using the functions (1) and (2); curve *2* was constructed according to the data of Ref. 15.

the Fermi energy E_F decreases from 0.69 to 0.66 Ry (from 9.4 to 9.0 eV), and the electronic density of states at the Fermi level $N(E_F)$ per unit cell increases from 5.7 to 23.2 Ry^{-1} (or per formula unit from 0.105 to 0.426 eV^{-1}). A feature due to the presence of an essentially linear section (Fig. 4, curve *2*) is observed in the dependence of $N(E_F)$ on the relative carbon content y in the carbide TiC_y at the point $y=0.82$. This section with $N(E_F)\approx 15-17$ Ry^{-1} (0.276–0.313 eV^{-1} per formula unit) corresponds to the region of compositions $TiC_{0.625}$–$TiC_{0.82}$. An increase in the vacancy concentration is accompanied by smoothing of all sharp peaks in the density of states (especially below E_F), by a decrease in the degree of filling of the low-energy subband of Ti–C interactions, and by an increase in the degree of filling of the high-energy conduction subband, being predominantly metallic in character. The dependence of $N(E_F)$ for TiC_y on y, with allowance for the feature at $y=0.82$, can be described by the simple expression

$$N(E_F)=c+\alpha y+\beta(y-0.82)^{2/3}, \tag{2}$$

where c, α, and β are adjustable parameters.

Minimizing the residual resistivity $\rho_{\text{res}}(y)$ by the function (1), taking account of the dependence (2) and $N(E_F)=0.105$ eV^{-1} per formula unit gave for the stoichiometric carbide $TiC_{1.0}$ $A=3.006$, $c=0.248$, $\alpha=-0.132$, and $\beta=-0.033$. The solid curve *1* in Fig. 4 shows the y dependence constructed for the residual resistivity of the disordered carbide TiC_y by the least-squares method on the basis of the experimental data. At $y=0.82$ a kink due to a similar feature in the electronic density of states is observed in the dependence $\rho_{\text{res}}(y)$. Previously, this kink in $\rho(y,300)$ at $y\approx 0.82$–0.83 had been observed in Ref. 5, where the resistivity of the disordered single-crystalline carbide TiC_y was measured. In Ref. 5 the kink was not explained, since the form and character of the variation of the electron-energy spectrum of titanium carbide TiC_y as a function of the content of carbon vacancies were unknown.

On the whole, our study of the structure and resistivity of the carbides TiC_y ($0.5<y<0.98$) showed that ordering of TiC_y with the formation of cubic (space group $Fd3m$) and trigonal ($R\bar{3}m$) superstructures Ti_2C and an orthorhombic ($C222_1$) superstructure Ti_3C_2 occurs at 970–1000 K and is accompanied by a decrease of resistivity.

The results obtained agree with the phase diagram proposed in Ref. 11 for the system Ti–C, which takes into account the ordering of the nonstoichiometric titanium carbide TiC_y. It was shown that the dependence of the resistivity on the composition of the disordered titanium carbide TiC_y is due to scattering of electrons by structural vacancies in the carbon sublattice and by the dependence of the carrier density on the vacancy content in the carbide.

This work was supported by the Russian Fund for Fundamental Research (Project 98-03-32890a).

*)e-mail: lipatnik@chem.ural.ru
†)e-mail: gusev@chem.ural.re; gusev@ihim.uran.ru

[1] A. I. Gusev, *The Physical Chemistry of Nonstoichiometric Refractory Compounds* [in Russian] (Nauka, Moscow, 1991).
[2] A. I. Gusev and A. A. Rempel, Phys. Status Solidi A **163**, 273 (1997).
[3] A. I. Gusev and A. A. Rempel, in *Materials Science of Carbides, Nitrides and Borides*, edited by Y. G. Gogotsi and R. A. Andrievski (Kluwer Acad. Publishers, Netherlands, 1999), p. 47.
[4] A. A. Rempel', Usp. Fiz. Nauk **166**, 33 (1996).
[5] W. S. Williams, Phys. Rev. A **135**, 505 (1964).
[6] J. Morillo, C. H. de Novion, and J. Dural, Radiat. Eff. **55**, 67 (1981).
[7] S. Otani, T. Tanaka, and Y. Ishizawa, Science **21**, 1011 (1986).
[8] Y. Ishizawa, S. Otani, H. Nozaki, and T. Tanaka, J. Phys.: Condens. Matter **4**, 8593 (1992).
[9] V. A. Vlasov, I. A. Karimov, and L. V. Kustova, Izv. Akad. Nauk SSSR, Neorg. Mater. **22**, 231 (1986).
[10] A. N. Emel'yanov, Fiz. Tverd. Tela (St. Petersburg) **38**, 3678 (1996) [Phys. Solid State **38**, 2003 (1996)].
[11] A. I. Gusev, Philos. Mag. B **60**, 307 (1989).
[12] C. H. de Novion, B. Beuneu, T. Priem *et al.*, in *The Physics and Chemistry of Carbides, Nitrides and Borides*, edited by R. Freer (Kluwer Acad. Publihses, Netherlands, 1990), p. 329.
[13] V. N. Lipatnikov, A. Kottar, L. V. Zueva, and A. I. Gusev, Fiz. Tverd. Tela (St. Petersburg) **40**, 1332 (1998) [Phys. Solid State **40**, 1211 (1998)].
[14] V. N. Lipatnikov and A. I. Gusev, JETP Lett. **69**, 669 (1999).
[15] A. I. Gusev and A. A. Rempel, Phys. Status Solidi A **135**, 15 (1993).
[16] N. Lorenzelli, R. Caudron, J. P. Landesman, and C. H. de Novion, Solid State Commun. **59**, 765 (1986).
[17] P. Marksteiner, P. Weinberger, A. Neckel *et al.*, Phys. Rev. B **33**, 812 (1986).

Translated by M. E. Alferieff

Bistability of quantum magnetotransport in a multilayer Ge/p-$Ge_{1-x}Si_x$ heterostructure with wide potential wells

M. V. Yakunin,*) Yu. G. Arapov, and V. N. Neverov
Institute of Metal Physics, Ural Branch of the Russian Academy of Sciences, 620219 Ekaterinburg, Russia

O. A. Kuznetsov
Scientific-Research Physicotechnical Institute at Nizhniĭ Novgorod State University, 603600 Nizhniĭ Novgorod, Russia

(Submitted 2 April 1999; resubmitted 7 July 1999)
Pis'ma Zh. Éksp. Teor. Fiz. **70**, No. 4, 290–297 (25 August 1999)

Two metastable states of a multilayer Ge/p-$Ge_{1-x}Si_x$ heterosystem with wide (~35 nm) potential wells (Ge) are observed in strong magnetic fields B at low temperatures. In the first state, the Hall resistivity exhibits an inflection near the value $\rho_{xy}=h/e^2$ scaled to one Ge layer. The longitudinal magnetoresistivity $\rho_{xx}(B)$ possesses a minimum in the range of fields where this inflection occurs. The temperature evolution of the inflection in $\rho_{xy}(B)$, the minimum of $\rho_{xx}(B)$, and the value of ρ_{xy} at the inflection indicates a weakly expressed state of the quantum Hall effect with a uniform current distribution over the layers. In the second metastable state, an unusually wide plateau near $h/2e^2$ with a very weak field dependence is observed in $\rho_{xy}(B)$. Estimates show that in these samples the Fermi level lies below but close to the top of the inflection in the bottom of the well. For this reason, the second state can be explained by separation of a hole gas in the Ge layers into two sublayers, and the saturation of $\rho_{xy}(B)$ near $h/2e^2$ can be explained by the formation of a quantum Hall insulator state. © *1999 American Institute of Physics.* [S0021-3640(99)01216-5]

PACS numbers: 73.50.Jt, 73.40.Hm, 73.40.Lq

The conductivity of a two-dimensional electron (2DE) system is highly sensitive to the characteristic features of the potential relief in the layer and the distribution of the electron liquid in it. For various ratios of the characteristic lengths describing the 2DE system (phase interruption and localization lengths) and the average size of the two-dimensional drops of the electron liquid in a layer, as well as for various size distributions of the drops and density distributions of the electron liquid contained in them, a macroscopic sample can be in fundamentally different states. For a high degree of disorder and low average density of the 2DE liquid per unit area, a two-dimensional system exhibits the characteristic properties of an insulator, i.e., its resistance increases with decreasing

temperature T.[1,2] This state was assumed to be the only possible state for all 2DE systems until the discovery of a metallic state of 2DE systems with high mobility and high density of the electron liquid.[2]

The components of the magnetoresistance of a 2DE system exhibit very diverse behavior. If the longitudinal magnetoresistivity $\rho_{xx}(T)$ exhibits insulator behavior, then as the temperature decreases, the Hall component ρ_{xy} either diverges[1] or it possesses a classical temperature-independent linear dependence on the magnetic field.[3–8] The latter state has been termed a Hall insulator.[9] As the magnetic field increases, the 2DE system transforms into the quantum Hall effect (QHE) phase. If the system in weak fields is in the insulator state, then between this phase and the QHE phase there is a sharp boundary — the magnetic field B_c^L, at which there is a node of the family of isotherms $\rho_{xx}(B,T)$ for different temperatures: for $B<B_c^L$ the value of ρ_{xx} increases with decreasing temperature, and for $B>B_c^L$ it decreases.

In highly disordered 2DE systems, the plateaus of the integer QHE are blurred. As the disorder decreases, the boundaries of the plateaus become progressively sharper, and almost vertical transitions between neighboring plateaus near half-integer values of the Landau filling factor ν of the levels are observed in certain ranges of moderate values of the mobility, i.e., the width of the plateaus reaches the maximum possible values.[10] As mobility increases further, sections of a linear field dependence are formed between the plateaus the plateaus decrease in size.[11] The disorder evolution of the first integer QHE plateau on the high-field side is more complicated. On the one hand, in systems with high mobility the Hall resistance isotherms $\rho_{xy}(B,T)$ start to deviate from the quantum value h/e^2 in the direction of the classical linear dependence on the field even for values $\nu>1/2$, passing through a common node near $\nu=1/2$.[8,12] However, for lower mobilities it has been observed that this plateau can be anomalously wide and can extend to values $\nu<1/2$, penetrating deeper into the field range $B>B_c^H$ (the field of the second (high-field) node of the isotherms $\rho_{xx}(B,T)$ that separates the QHE phase from the high-field insulator phase). Such an anomalously wide plateau $\rho_{xy}=h/e^2$ has been observed in the n-type heterosystem GaAs/n-$Al_{1-x}Ga_xAs$ (Ref. 13) and in a quantum well of the heterosystem Ge/p-$Ge_{1-x}Si_x$ (Refs. 14 and 15). An anomalously wide fractional QHE plateau for $\nu=1/3$ has also been observed in the system GaAs/n-$Al_{1-x}Ga_xAs$ (Ref. 16). This state — with diverging $\rho_{xx}(B,T)$ and unchanged $\rho_{xy}(B,T)$, equal to or a multiple of the resistance quantum h/e^2 — has been termed a ''quantum Hall insulator'' (QHI).[7] The limited number of experiments in which the QHI state has been observed is probably an indication that this state exists in very limited ranges of disorder in a 2DE system. On the other hand, it is known that the additional degree of freedom due to the possibility of bounded motion of carriers in a third dimension in wide layers or systems of coupled layers could lead to additional stabilization of certain unstable states of the QHE.[18] This is the problem addressed in the present work — investigation of the characteristic features of quantum magnetotransport in a wide quantum well of a heterosystem with moderate mobility.

We measured the longitudinal $\rho_{xx}(B)$ and Hall $\rho_{xy}(B)$ magnetoresistivities of Ge/p-$Ge_{1-x}Si_x$ multilayer samples grown by the gas-transport method and possessing the following structure: Ge(111) substrate/$\sim$1.8 μm Ge buffer/0–1.6 μm $Ge_{1-y}Si_y$ buffer/(Ge/$Ge_{1-x}Si_x$:B)$\times N$. The thickness of the Ge layers (d_w, potential well for holes) and $Ge_{1-x}Si_x$ layers (d_b, barrier) in the multilayer region were comparable and

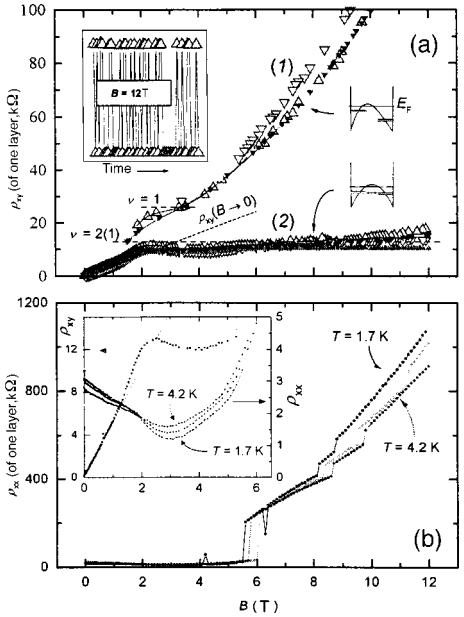

FIG. 1. a) Bistability of the Hall resistance of sample 451b4. The triangles with vertex pointing upwards correspond to positive current polarity, triangles with vertex pointing downwards correspond to negative polarity. The unfilled and filled triangles are for $T=1.7$ and 4.2 K, respectively. The numbers *1* and *2* on the curves are the numbers assigned to the states. The dashed horizontal lines show the values $\rho_{xy}=h/e^2$ and $h/2e^2$ scaled to one Ge layer. The solid curves show the results of a polynomial fit of the points of the state *1* at $T=1.7$ and 4.2 K. The dashed sloping straight line (just as in the inset in Fig. 1b) was obtained by extrapolating the linear section of $\rho_{xy}(B)$. Inset on the left-hand side: Results of measurements in a fixed field $B=12$ T. The insets on the right-hand side illustrate the proposed differences of the potential profile and the arrangement of the size-quantization levels in two metastable states. b) Longitudinal magnetoresistivity $\rho_{xx}(B)$ at $T=1.7$,3.2, and 4.2 K. In the inset the minimum of $\rho_{xx}(B)$ is juxtaposed with the dependence $\rho_{xy}(B)$.

varied from sample to sample in the range from 10 to 40 nm. The $Ge_{1-x}Si_x$ layers were doped with boron in the central part so that undoped spacers with a width of about 1/4 of the barrier thickness remained on both sides of the barrier. In the parameter ranges $d_w=10$–30 nm, $y\approx 0.07$, and $x=0.07$–0.10, hole gas density $p_s=(2.8–5)\times 10^{15}$ m^{-2} and mobility $\mu=1$–1.5 m^2/V·s, the characteristic integer QHE picture,[19] typical of systems with moderate carrier mobility,[20] was observed. It is important that the Hall resistance plateaus scaled to one layer corresponded to the fundamental values $h/e^2\nu$, $\nu=1, 2, \ldots$ with an accuracy not worse than several percent (for the smallest values of ν). This means that virtually all layers of the samples participated equally in current transport (with a maximum error of one layer).

A more complicated behavior in a magnetic field was observed in the samples 451a4 and 451b4 of the same system with wider potential wells $d_w=35.5$ nm and much lower hole density $p_s=1.4\times 10^{15}$ m^{-2} (all other parameters, $d_b=23.5$ nm, the number of periods $N=36$, $y\approx 0.087$, $x=0.097$, and $\mu=1.4$ cm^2/V·s). See Fig. 1, which displays data for sample 451b4 (analogous results were obtained with different pairs of junctions; similar results were also obtained for sample 451a4, grown in the same technological cycle). Up to fields of about 2 T the results of the measurements are stable, i.e., all

experimental points for each component of the magnetoresistivity $\rho_{xx}(B)$ and $\rho_{xy}(B)$ fall on a single smooth curve. Unstable behavior appears in higher fields: The positions of the points $\rho_{xy}(B)$ change abruptly from measurement to measurement. The essential finding is that for $\rho_{xy}(B)$ these points form two smooth curves, while the behavior of $\rho_{xx}(B)$ remains stable up to high fields, approximately up to 6 T.

The upper $\rho_{xx}(B)$ curve (we assign the number *1* to this curve and to the corresponding state) at fields in the region $B \gtrsim 4$ T increases monotonically with the field and extrapolates to zero as $B \to 0$. In fields $B < 4$ T this curve possesses an inflection near $\rho_{xy} = 25.8\ \text{k}\Omega = h/e^2$, scaled to one Ge layer. A sharp minimum is observed in the longitudinal magnetoresistivity $\rho_{xx}(B)$ in the same field range (~ 3 T) in which the inflection in $\rho_{xy}(B)$ occurs. As the temperatures decreases from 4.2 K to 1.7 K, the minimum of $\rho_{xx}(B)$ becomes deeper, and the slope of $\rho_{xy}(B)$ at the inflection point decreases (i.e., the inflection gradually transforms into a horizontal plateau). The curves $\rho_{xx}(B,T)$ at different temperatures pass through a common point at $B \approx 1.8$ T, to the left of which lies the insulator phase. The QHE phase should lie to the right of this point.[3–8] Therefore the behavior of the components $\rho_{xy}(B,T)$ and $\rho_{xx}(B,T)$ leaves no doubt that the inflection in ρ_{xy} and the minimum in ρ_{xx} are weakly expressed features of the QHE, and the fact that ρ_{xy} is close to h/e^2 at the inflection point shows that, first, this feature corresponds to a filling factor of the Landau levels $\nu = 1$ in the Ge layer and, second, almost all (at least) of the Ge layers in the structure are equivalent.[1)] We also note that in high fields the family of isotherms $\rho_{xx}(B,T)$ also approaches a common node. Although the unstable behavior of $\rho_{xx}(B)$ in this field range does not permit determining this node accurately, the node definitely exists (at a field $B_c^H \approx 6$ T). This is evident, specifically, from the fact that the curve $\rho_{xx}(B)$ for 1.7 K is the lowest curve at the minimum at $B \approx 3$ T, but it is the uppermost curve in the strong-field range (Fig. 1b).

The lower $\rho_{xy}(B)$ curve (curve and state *2*) after a quite sharp inflection saturates, and in fields from ~ 2 T up to the maximum measured field 12 T it is concentrated in the range from 11 to 13 kΩ, including the value $h/2e^2 = 12.9\ \text{k}\Omega$, corresponding to a filling factor $\nu = 2$ of the Landau levels of one layer. We note once again that the multilayer nature of the structures investigated does not permit us to realize one of the advantages of the QHE — the high accuracy of ρ_{xy} at the center of a plateau, equal to or a multiple of the universal value h/e^2. The possible nonequivalence of the layers introduces a greater or lesser error in the value obtained after the measurement results are scaled to one layer, and it can also distort the form of the QHE plateaus. Nonetheless, it is difficult to imagine that the observed closeness of the values of ρ_{xy} at the inflection in the state *1* and in the wide plateau in the state *2* to h/e^2 and $h/2e^2$, respectively, and their ratio of 2 are accidental. Likewise, the results of Ref. 19, obtained on samples from the same family but with a sharper QHE picture, show that the error contributed to ρ_{xy} on a plateau by the multilayer nature of the structure *can* be negligible. For this reason, we attribute the results obtained here primarily to processes occurring in an individually taken (averaged) Ge layer, and we assume that the nonequivalence of the layers will lead to only small, nonfundamental distortions in the results of such an analysis. We note that the small slope of $\rho_{xy}(B)$ on the QHI plateau is possible because because of the finiteness of the temperatures. It has also been observed in single-layer structures at $T \geqslant 4.2$ K.[14] According to theory,[21] small deviations of $\rho_{xy}(B)$ from quantum values in the QHI regime are also possible because of quantum interference between different tunneling transitions in a

system of two-dimensional conducting drops in the body of the sample.

In the experiment, the abrupt transition from one state into another is caused by the interruption or switching of the polarity of the current. It is important that data for both current polarities are present on each of the two curves obtained in this manner (see triangles with vertex pointing upward and downward in the figure). For this reason, the observed splitting of the experimental data is not a manifestation of any asymmetry in the sample (for example, at the junctions); more likely, the interruption of the current provides an impetus, transferring the sample from one metastable state into another. The inset in Fig. 1a shows results of measurements of $\rho_{xy}(B)$ in a fixed field $B=12$ T for one polarity of the current; each point was obtained after a current pulse with the reverse polarity was passed through the sample. It is evident that the points move arbitrarily between two fixed values of the resistance, the distance between which is regulated by the magnetic field. In the approximate range of fields $B \geqslant 6$ T, where intense instabilities are already observed in $\rho_{xy}(B)$, the curve of longitudinal magnetoresistivity likewise exhibits instability, transforming into rapid stepped growth (see Fig. 1b), which could indicate breakdown of the QHE. However, the bistability of the Hall resistance remains. This bistability was observed without large changes over the current range 10–100 μA and temperature range 1.6–4.2 K.

In a wide potential well, with selective doping of the barriers, the spatial separation of the charges leads to an inflection at the bottom of the well. Estimates for an infinitely deep well give an amplitude of the inflection of the bottom $u_0=\pi e^2 p_s d_w/2k$ (k is the permittivity). Equating this value to the Fermi level $E_F=\pi\hbar^2 p_s/m^*$, we obtain $u_0/E_F = e^2 m^* s d_w/2\hbar^2 k$. For structures with not very wide wells, investigated in Ref. 19 (on which the standard results for QHE were obtained), this parameter is smaller, ~ 0.9. For samples 451b4 and 451a4 it is 1.3 and 1.5, respectively. That is, in these samples the Fermi level lies below the amplitude of the inflection of the well bottom. For this reason, here a new physical situation can be expected to appear as a result of a transition to two tunneling-coupled quantum wells, formed as a result of the separation of the carrier gas in each Ge layer into two sublayers.

The $\rho_{xy}(B)$ curve *2* taken together with the $\rho_{xx}(B,T)$ curves forms a picture which is surprisingly similar to the results of the manifestations of the quantum Hall insulator state in Ref. 14: A wide plateau is observed which is strongly asymmetric about the point of its intersection with the straight line of the classical Hall resistance obtained by extrapolating from weak fields and about the position of the minimum of $\rho_{xx}(B)$; the left-hand boundary of the plateau lies near the low-field node B_c^L of the family of curves $\rho_{xx}(B,T)$, while in the high-field region the plateau extends far beyond the position of the high-field node B_c^H of this family. Just as in Ref. 14, the observed plateau is the only one; there are no features of an integer QHE for larger filling factors. The difference lies in the fact that in our case the plateau corresponds approximately to $\rho_{xy}=h/2e^2$ (scaled to one Ge layer), while in Ref. 14 this plateau corresponds, to a high degree of accuracy, to $\rho_{xy}=h/e^2$. Since a transition to the QHI state from the QHE state with $\nu=2$ is not possible in light of existing models[17] and has never been observed, it is natural to infer that curve *2* in our experimental results corresponds to a situation where in each Ge layer current flows along two equivalent sublayers at the walls of a potential well with a curved bottom. Then the real number of 2D layers in the sample will be twice the number of Ge layers, and the resistance of one such sublayer in the region of the plateau will be close

to $\rho_{xy}=h/e^2$. As mentioned above, the small error in this value in our results can be explained by the multilayer nature of our samples; this also explains the distortion of the plateau in the form of a small depression at $B\approx 4$ T.

The minimum of $\rho_{xx}(B)$ at 3 T should correspond to a filling factor $\nu=1$ for one 2D layer, and not $\nu=2$, since it is evident that there is no other minimum at twice the field, 6 T. Indeed, calculations of Landau levels of the Ge valence band in a quantum well[22] show that the energy splittings between all total-angular-momentum-split-off levels are comparable (in contrast, for example, to the conduction band of Ga and As, whereas the spin sublevels can be unresolved because of the small g factor). For this reason, in the presence of a feature with $\nu=2$, another, even more sharply expressed, feature with $\nu=1$ should also exist in the system Ge/p-$Ge_{1-x}Si_x$ at twice the field. The position of the minimum of $\rho_{xx}(B)$ at 3 T gives $p_s=0.7\times 10^{15}$ m^{-2} for the two-dimensional gas with $\nu=1$, half the value obtained from the slope of $\rho_{xy}(B)$ in a weak field, scaled to one Ge layer. This also indicates the presence of two two-dimensional layers in each Ge layer.

In summary, it follows from the data that a sample in fields $B\gtrsim 3$ T can exist in two states: *1* — a state with a weakly expressed quantum Hall feature with $\nu=1$, where one conducting 2D layer of holes is present in each Ge layer, and *2* — a QHI state with holes divided into two two-dimensional sublayers in each Ge layer and saturation of $\rho_{xy}(B)$ of each sublayer near h/e^2. In state *1* the density of mobile holes in the Ge layer is approximately half as large as in state *2*.

The following model can be suggested. The metastability of the states *1* and *2* indicates the existence of a self-stabilizing mechanism. Evidently, this mechanism is due to the very essence of the formation of intercoupled double layers in a wide well. If the configuration of the potential well is nearly symmetric, then the equivalent energy levels in triangular wells at the walls are closest to one another in energy, which increases the probability of tunneling between them. The sublayers in the Ge layer are in a state of mutual balance. A small skewing of the potential well by an external impulse will cause carriers to flow through the tunneling channel from one sublayer into another, which will prevent further skewing of the well and ultimately restore its configuration (see, for example, Ref. 23 and references cited therein). However, if a different (asymmetric) state of the system is possible, for example, because of reproducible asymmetry in the arrangement of the doped layer in the barriers, then the system can pass into it under the action of a sufficiently strong perturbation, which will cause a skewing of the potential well such that tunneling between identical levels of the sublayers will be substantially suppressed (see the inset on the right-hand side in Fig. 1a). For an asymmetric profile, the properties of the 2D sublayers in triangular wells at the boundaries of the Ge layer will become different. The appearance in the experiment of a weak plateau for $\nu=1$ of the Ge layer in the state *1* on the whole means that one of the sublayers in each Ge layer is excluded from conduction. Evidently, this is the sublayer that lies in a narrower triangular well. Indeed, a smaller width of the sublayer will result in a decrease of the concentration in it. Both factors will facilitate transition of a hole gas in the sublayer into an insulator phase, i.e., they will decrease the critical magnetic field in which such a transition must inevitably occur.[18] Broadening of the other triangular well can serve as a reason for a transition of the sublayer located in it from the QHI into the QHE phase (specifically, this will be enabled by a change in the parameters of disorder in the direction of growth[17]).

On account of the Coulomb coupling between the Ge layers (the width of the GeSi

barriers is less than the width of the Ge quantum wells in our samples) the transition to an asymmetric distribution of charge in one Ge layer will affect adjoining Ge layers and then the entire multilayer structure as a whole. That is, these two metastable states are collective modes in a multilayer system, so that a transition between them will occur in all layers synchronously. The presence of collective charge modes will also stabilize the individual states of the system. Effects due to bistability in asymmetric double quantum wells have been observed in a number of works.[23]

In the present model, however, it remains unclear why the regions of stability of $\rho_{xy}(B)$ ($\lesssim 2$ T) and $\rho_{xx}(B)$ ($\lesssim 5.5$ T) are different. This is probably due to the complicated mechanism of current flow through the sample, for example, in the model of chaotic array of flat drops — percolation along a network of edge states surrounding the drops. The possibility of the existence of the QHI phase has been shown precisely in this model on the basis of an analysis of the balance between percolation along a network and tunneling between neighboring drops.[17] Then, in our samples with wide Ge layers it is necessary to study the conductivity in each layer along two networks located at the edges of the layer. The novelty of the situation here will lie in the fact that these networks are weakly coupled with one another by tunneling, the Coulomb interaction, and the possible presence of rare conducting bridges between them. Whether or not a change in the charge balance between two networks can lead in such a combined model to the existence of the states described in the present letter, which are characterized either by a weak QHE or QHI, and whether or not qualitatively different dependences $\rho_{xy}(B)$ with the same form of the dependence $\rho_{xx}(B)$ can appear in it, are questions for further investigations.

This work was supported by the Russian Fund for Fundamental Research, Grants Nos. 98-02-17306 and 99-02-6256.

*)e-mail: yakunin@imp.uran.ru

1)These two conclusions cannot be the result of interrelated coincidences. For example, the same value of ρ_{xy} could be obtained for $\nu=2$, if exactly half the layers were operational. But then the curve *1* would necessarily have another, more pronounced feature with twice the Hall resistance at twice the field; for the same number of operating layers that feature would correspond to a factor $\nu=1$ (see text below). However, there is not even a hint of this!

[1] M. J. Uren, R. A. Davies, M. Pepper *et al.*, J. Phys. C: Solid State Phys. **14**, 5737 (1981); D. J. Bishop, D. C. Tsui, and R. C. Dynes, Phys. Rev. Lett. **46**, 360 (1981).
[2] S. V. Kravchenko, G. M. Kravchenko, J. E. Furneaux *et al.*, Phys. Rev. B **50**, 8039 (1994).
[3] H. W. Jiang, C. E. Johnson, V. L. Wang *et al.*, Phys. Rev. Lett. **71**, 1439 (1993).
[4] T. Wang, K. P. Clark, G. F. Spencer *et al.*, Phys. Rev. Lett. **72**, 709 (1994).
[5] R. J. F. Hughes, J. T. Nicholls *et al.*, J. Phys.: Condens. Matter **6**, 4763 (1994).
[6] C. H. Lee, Y. H. Chang, Y. W. Suen *et al.*, Phys. Rev. B **56**, 15238 (1997).
[7] D. Shahar, D. C. Tsui, and J. F. Cunnigham, Phys. Rev. B **52**, R14372 (1995).
[8] S. H. Song, D. Shahar, and D. C. Tsui, Phys. Rev. Lett. **78**, 2200 (1997).
[9] S. Kivelson, D.-H. Lee, and S.-C. Zhang, Phys. Rev. B **46**, 2223 (1992).
[10] H. H. Paalanen, D. C. Tsui, and A. C. Gossard, Phys. Rev. B **25**, 5566 (1982); G. Ebert, K. V. Klitzing, C. Probst *et al.*, Solid State Commun. **44**, 95 (1982).
[11] H. L. Stromer, A. Chang, D. C. Tsui *et al.*, Phys. Rev. Lett. **71**, 1439 (1993); T. Sajoto, Y. W. Suen, L. W. Engel *et al.*, Phys. Rev. B **41**, 8449 (1990).
[12] L. W. Wong, H. W. Jiang, and W. J. Schaff, Phys. Rev. B **54**, R17323 (1996).
[13] D. Shahar, D. C. Tsui, M. Shayegan *et al.*, Solid State Commun. **102**, 817 (1997).
[14] M. Hilke, D. Shahar, S. H. Song *et al.*, Nature **395**, 675 (1998).
[15] M. V. Yakunin, Yu. G. Arapov, O. A. Kuznetsov, and V. N. Neverov, in *Proceedings of the 6th International*

Symposium on ''Nanostructures: Physics and Technology'', St. Petersburg, 1998, p. 462; Izv. Ross. Akad. Nauk, Ser. Fiz. **63**, 334 (1999).
[16] D. Shahar, D. C. Tsui, M. Shayegan *et al.*, Science **274**, 589 (1996); M. Hilke, D. Shahar, S. H. Song *et al.*, http://xxx.lanl.gov/abs/cond-mat/9810217
[17] E. Shimshoni and A. Auerbach, Phys. Rev. B **55**, 9817 (1997).
[18] H. C. Manoharan, Y. W. Suen, M. B. Santos *et al.*, Phys. Rev. Lett. **77**, 1813 (1996).
[19] Yu. G. Arapov, V. N. Neverov, G. I. Kharus *et al.*, Fiz. Tekh. Poluprovodn. **32**, 721 (1998) [Semiconductors **32**, 649 (1998)].
[20] M. E. Cage, in *The Quantum Hall Effect*, edited by R. E. Prange and S. M. Givrin (Springer-Verlag, New York, 1989) [Russian translation, Mir, Moscow, 1989].
[21] L. Pryadko and A. Auerbach, Phys. Rev. Lett. **82**, 1253 (1999); E. Shimshoni, http://xxx.lanl.gov/abs/cond-mat/9904145.
[22] Yu. G. Arapov, N. A. Gorodilov, V. N. Neverov *et al.*, JETP Lett. **59**, 245 (1994).
[23] Y. Takagaki, K.-J. Friedland *et al.*, J. Phys.: Condens. Matter **10**, 8305 (1998); M. I. Stockman, L. N. Pandey *et al.*, Phys. Rev. B **48**, 10966 (1993).

Translated by M. E. Alferieff

Magnetoplastic effect in InSb

E. V. Darinskaya and E. A. Petrzhik
Institute of Crystallography,[*)] Russian Academy of Sciences, 117333 Moscow, Russia

S. A. Erofeev and V. P. Kisel'
Institute of Solid-State Physics, Russian Academy of Sciences, 142432 Chernogolovka, Moscow Region, Russia

(Submitted 9 July 1999)
Pis'ma Zh. Éksp. Teor. Fiz. **70**, No. 4, 298–302 (25 August 1999)

We have observed dislocation motion in InSb semiconductor crystals under the action of a static magnetic field in the absence of a mechanical load. The dependence of the average dislocation travel distance and of the relative number of diverging and converging half-loops on the magnetic induction and the ''magnetic treatment'' time is obtained. The activation energy of the motion of diverging dislocations in a magnetic field in the temperature range 120–250 °C is estimated. Possible reasons for the observed phenomenon are discussed. © *1999 American Institute of Physics.* [S0021-3640(99)01316-X]

PACS numbers: 75.80.+q, 61.72.Lk, 81.40.Lm

The existence of the magnetoplastic effect — dislocation motion in a static magnetic field in the absence of a mechanical load — has now been reliably established in nonmagnetic alkali-halide and metallic crystals (NaCl, CsI, LiF, Zn, and Al). This phenomenon has been studied in a number of experimental and theoretical works by independent groups.[1–5]

The systematic investigations[6–8] that have been performed give a basis for assuming that the dislocation motion occurs in the internal stress field of the crystal, and the role of the magnetic field reduces to depinning of dislocations from paramagnetic centers. This depinning can be explained on the basis of the concept of spin-dependent electronic transitions in an external magnetic field. The magnetic field gives rise to evolution of the spins in the system dislocation + paramagnetic center, which is completed by lifting of the spin forbiddenness on a certain electronic transition. This changes radically the configuration of the system; for example, it decreases the height of the barrier for dislocation motion. The total energy in the system remains essentially unchanged. A similar ideology lies at the basis of the physical interpretation[9] of the effect of a magnetic field on a host of processes, including the chemical reaction rates[10] and photocurrent in semiconductors.[11]

In the present work, the magnetoplastic effect has been observed in semiconductor crystals. In this letter we report the results of an investigation of the motion of 60-degree dislocations in InSb crystals under the action of a static magnetic field in the absence of a mechanical load.

The experiments were performed on pure *n*-InSb single crystals with carrier density $1\times10^{14}\,\mathrm{cm}^{-3}$. The samples were cut out in the form of quadrangular bars with the dimensions $3\times1.5\times40$ mm in the [111], [112], and [110] directions, respectively. To introduce ''fresh'' dislocations, a slight scratch in the [110] direction on the (111) observation surface was made with a corundum needle. During subsequent deformation by four-point bending at temperature 200 °C under a load $\tau=15$ MPa in 5 min the dislocations dispersed to distances of 1000–2000 μm away from the scratch. The sample preparation method is described in detail in Refs. 12 and 13.

The prepared samples were placed in a uniform static field of an electromagnet ($B=0.2-0.9$ T) for time t ranging from several seconds to 50 min. The experiments were performed at temperatures $T=120$, 150, 200, and 250 °C with slow preheating for 50 min and subsequent analogous slow cooling. No external mechanical load was applied during ''magnetic treatment.''

The observations were performed on fast 60-degree dislocations. The initial and final positions of the dislocations before and after holding in a magnetic field, respectively, were determined by selective chemical etching (SR-4A etchant: 5 parts HNO_3 + 3 parts HF + 3 parts CH_3COOH).

The motion of 60-degree fast dislocations in InSb crystals in a static magnetic field in the temperature range $T=120-250$ °C without any mechanical load was observed. The essential point is that dislocations are observed to move toward the scratch (contracting half-loops) and away from the scratch (diverging half-loop). Control annealing of the samples in the absence of a magnetic field results primarily in the contraction of the half-loops ($\approx90\%$ of the total number of the dislocations that have moved). The typical etch pattern of the (111) face of the InSb sample after holding in a $B=0.7$ T magnetic field at 200 °C for 10 min is displayed in Fig. 1. It is evident that dislocations move predominantly away from the scratch. The average dislocation travel distances l were determined from the etch patterns for various conditions of the experiment (the measurement accuracy was $\approx15\%$). Figure 2a shows the average travel distance of diverging dislocations as a function of the external magnetic field B. The essential point is that at a certain magnetic field the average travel distance becomes proportional to the squared magnetic induction. For converging dislocations, no dependence of the travel distance on the magnetic induction was observed.

Together with measurement of the average travel distance, the relative number (n/N, where N is the total number of dislocations that have moved) of diverging (points *1* in Fig. 2b) and converging (points *2* in Fig. 2b) dislocations was also determined. It was found that as the magnetic induction increases, the relative number of converging half-loops decreases and, correspondingly, the relative number of diverging half-loops increases. After a certain ''inversion field'' these dependences saturate. The points *3* and *4* in Fig. 2 refer to control experiments in which samples were heated without the application of a magnetic field. Similar data (points *5* and *6* in Fig. 2) were obtained for a brief ($\approx2-3$ s) switching on and off of the electromagnetic without further magnetic treatment.

Figure 3 shows the travel distance and the relative number of mobile dislocations as a function of the holding time t of the samples in a magnetic field. A linear dependence of the average travel distance of diverging dislocations on the time is observed. The

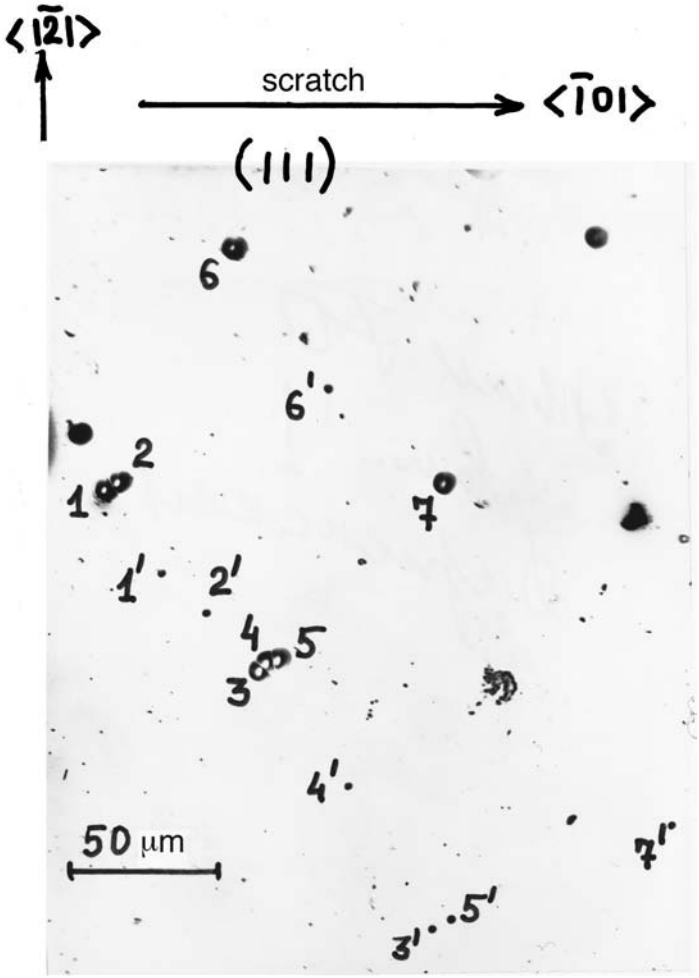

FIG. 1. Displacements of dislocations in InSb crystals under the action of a 0.7 T static magnetic field at temperature 200 °C, $t=10$ min: *1, 2,* ... — initial positions of the dislocations, *1′, 2′,* .... — final positions of the dislocations.

relative number of diverging and converging half-loops increases and decreases, respectively, with increasing *t,* and after a certain ''inversion time'' they saturate. For holding in a $B=0.7$ T magnetic field (and simultaneously at $T=200\,^{\circ}$C) for 50 min, the relative number of diverging half-loops decreases sharply ($\approx 20\%$ instead of the expected 80%), though their average travel distance continues to increase and follows well a linear dependence $l(t)$.

The results of the investigations of the effect of temperature on dislocation mobility in a magnetic field are presented in Fig. 4. An estimate of the activation energy from the slope of the plot $\ln(l/t)$ versus $(1/T)$ gives ≈ 0.3 eV. The value obtained for the activation energy of dislocation motion in a magnetic field during heating is 2.5 times lower than the activation energy of the motion of 60-degree dislocations in the same InSb crystals

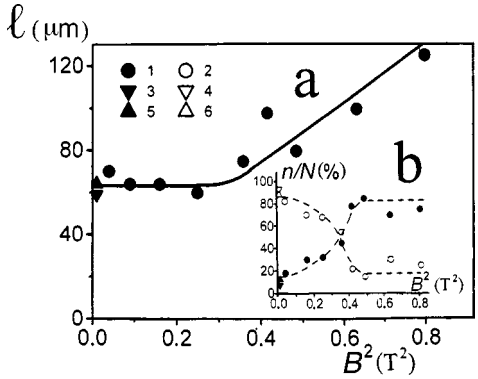

FIG. 2. a — Average travel distance l of diverging dislocations, and b — relative number n/N of diverging (*1, 3, 5*) and converging (*2, 4, 6*) dislocations versus the magnetic induction B; $t=10$ min, $T=473$ K; *3, 4* — annealing only, *5, 6* — electromagnet switched on and off.

under the action of a mechanical load with the same heating in the absence of a magnetic field.[12–14] Such a decrease of the activation energy of dislocation motion in a magnetic field seems to be due to the detachment of dislocations from paramagnetic obstacles as a result of spin-dependent electronic transitions in the system dislocation + paramagnetic center. Therefore a magnetic field ''removes'' some obstacles and greatly facilitates the thermal activation process of relaxation of the dislocation structure.

The effect of successive applications of a magnetic field on dislocation motion during annealing was studied. In the first case, after annealing at 200 °C for 50 min a $B=0.8$ T magnetic field was immediately applied for $t=10$ min at the same temperature. In the second case, first magnetic treatment ($B=0.8$ T; $t=10$ min; $T=200$ °C) and then annealing ($T=200$ °C; $t=50$ min) were performed. The average travel distance and the relative number of diverging dislocations were found to be greater in the first case (134 μm and 70% as against 114 μm and 40%). For ordinary annealing ($T=200$ °C, $t=50$ min) less than 20% of the dislocations diverge. Therefore our preliminary experi-

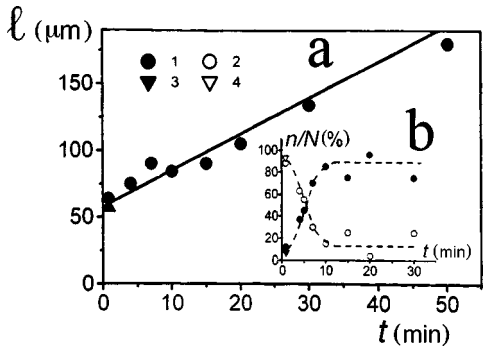

FIG. 3. a — Average travel distance l of diverging dislocations, and b — relative number n/N of diverging (*1, 3*) and converging (*2, 4*) dislocations versus the holding time t of the samples in a $B=0.7$ T magnetic field; $T=473$ K; *3, 4* — annealing only.

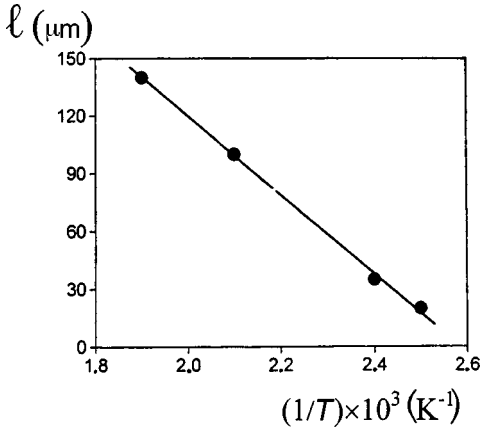

FIG. 4. Average travel distance l of diverging dislocations versus the temperature T; $B = 0.8$ T, $t = 10$ min.

ments show that a magnetic field not only facilitates ordinary relaxation of the dislocation structure during annealing but it also changes the direction of motion: predominant contraction of half-loops is replaced by divergence.

Further investigations are required to determine the nature of the phenomenon observed here. We thank V. I. Al'shits and B. V. Petukhov for helpful discussions.

This work was supported by the Russian Fund for Fundamental Research (Grant No. 97-02-16327).

*)e-mail: public@mechan.incr.msk.su

[1] V. I. Al'shits, E. V. Darinskaya, T. M. Perekalina, and A. A. Urusovskaya, Fiz. Tverd. Tela (Leningrad) **29**, 467 (1987) [Sov. Phys. Solid State **29**, 265 (1987)].
[2] Yu. I. Golovin, R. B. Morgunov, V. E. Ivanov *et al.*, JETP Lett. **68**, 426 (1998).
[3] É. P. Belozerova, A. A. Svetashov, and V. L. Krasnikov, Izv. Ross. Akad. Nauk, Ser. Fiz. **61**, 291 (1997).
[4] V. I. Al'shits, N. N. Bekkauer, A. E. Smirnov, and A. A. Urusovskaya, Zh. Éksp. Teor. Fiz. **115**, 951 (1999) [JETP **88**, 523 (1999)].
[5] M. I. Molotskii and V. Fleurov, Phys. Rev. Lett. **78**, 2779 (1997).
[6] V. I. Alshits, E. V. Darinskaya, O. L. Kazakova *et al.*, J. Alloys Compd. **211/212**, 548 (1994).
[7] V. I. Alshits, E. V. Darinskaya, O. L. Kazakova *et al.*, Mater. Sci. Eng., A **234-236**, 617 (1997).
[8] V. I. Alshits, E. V. Darinskaya, O. L. Kazakova *et al.*, *Proceedings of the International Symposium on Trends in Continuum Physics* (World Scientific, Singapore, 1999).
[9] Ya. B. Zel'dovich, A. L. Buchachenko, and E. L. Frankevich, Usp. Fiz. Nauk **155**, 3 (1988) [Sov. Phys. Usp. **31**, 385 (1988)].
[10] A. L. Buchachenko, R. Z. Sagdeev, and K. M. Salikhov, *Magnetic and Spin Effects in Chemical Reactions* [in Russian] (Nauka, Novosobirsk, 1978).
[11] V. V. Kveder, Yu. A. Osip'yan, and A. I. Shalynin, Zh. Éksp. Teor. Fiz. **83**, 699 (1982) [Sov. Phys. JETP **56**, 389 (1982)].
[12] S. A. Erofeeva, Philos. Mag. **70**, 943 (1994).
[13] V. P. Kisel, S. A. Erofeeva, and M. Sh. Shikhsaidov, Philos. Mag. A **67**, 343 (1993).
[14] S. A. Erofeeva and Yu. A. Osip'yan, *Dynamics of Dislocations* [in Russian] (Naukova Dumka, Kiev, 1975), p. 26.

Translated by M. E. Alferieff

Giant red shift of the absorption edge in $La_{0.9}Sr_{0.1}MnO_3$

R. V. Demin and L. I. Koroleva
M. V. Lomonosov Moscow State University, 119899 Moscow, Russia

A. M. Balbashov
Moscow Power Engineering Institute, 111250 Moscow, Russia

(Submitted 20 July 1999)
Pis'ma Zh. Éksp. Teor. Fiz. **70**, No. 4, 303–306 (25 August 1999)

The absorption edge of the perovskite $La_{0.9}Sr_{0.1}MnO_3$, determined using the diffuse reflection coefficient spectra, shifts by the giant amount 0.4 eV in the direction of lower energies as the temperature decreases from the Curie point (155 K) to 141 K. © *1999 American Institute of Physics.* [S0021-3640(99)01416-4]

PACS numbers: 75.50.Pp, 75.30.Vn, 78.40.Fy

In recent years interest in compounds with perovskite structure $Re_{1-x}A_xMnO_3$ (Re=La and rare-earth elements, A=Sr, Ca, Ba, and others) has increased sharply because of the colossal magnetoresistance (CMR) observed in some of them at room temperature. This makes it possible to use them in various sensor devices. At present, there exist various points of view concerning the nature of the CMR in manganites. The problem is that compared with conventional magnetic semiconductors (EuO, EuSe, EuTe, $CdCr_2Se_4$, and $HgCr_2Se_4$), where CMR is attributed to special magnetoimpurity states — ferrons,[1] in manganites the picture is complicated by the presence of the Jahn–Teller effect, giving rise to localization of charge carriers, and relative softness of the lattice, as a result of which a change of lattice type occurs under the action of a magnetic field, pressure, and temperature. As a result, a number of authors have advanced other explanations of CMR in these materials: melting of a charge-ordered state, transition from Zener double exchange to polaron-type conductivity above the Curie point T_C, and others, described in the reviews[2–4] and the references cited therein. However, it should be noted that the CMR (and especially its peak) is observed near the Curie point and consists of the suppression of the resistance peak at T_C, while the hypotheses listed above cannot explain this fact. Moreover, it should be indicated that the charge ordering and the Jahn–Teller effect are observed in many materials, including perovskites, but CMR has not been observed in any of them.

We assume that the CMR occurs in manganites for the same reasons as in conventional magnetic semiconductors, specifically, a magnetically two-phase ferro–antiferromagnetic state. Negaev has shown[1,5] that in antiferromagnetic (AFM) semiconductors, because of the gain in $s-d$ exchange energy, the conduction electrons are localized with not too high density near donor impurities in ferromagnetic (FM) microregions in an insulating AFM matrix. Under the action of a magnetic field the volume of these FM drops increases, and in addition percolation of these drops and an insulator–

metal transition are possible. In fields up to the percolation threshold, an increase in the FM drop sizes facilitates tunneling of charge carriers between them. Moreover, a magnetic field orients the magnetic moments of the drops along the field, and this also facilitates tunneling. Finally, a magnetic field increases the kinetic energy of the electrons, which facilitates electron tunneling and causes the FM drops to breakdown. These circumstances give rise to CMR.[6]

However, the above-described magnetically two-phase state is possible only in compounds where the band gap decreases with increasing degree of FM order (with decreasing temperature or imposition of a magnetic field). For example, the giant red shift of the fundamental absorption edge, caused by a shift of the conduction-band bottom and associated with an increase in the degree of FM order, has been observed in a number of conventional magnetic semiconductors.[7–10] This means that the energy of the conduction electrons decreases with increasing degree of FM order, and for this reason it was energetically favorable for conduction electrons to become localized with not too high density near impurities, maintaining FM order around them. Here their localization, besides a gain in $s-d$ exchange energy, gave rise to Coulomb attraction of electrons to donors. In doped manganites, conduction is due to holes at the top of the valence band. The observation of a giant red shift of the fundamental absorption edge in them with decreasing temperature, due to the shift of the valence-band top, would signify that it is energetically favorable for holes to localize near acceptor impurities, maintaining FM order around them on account of a gain in the $p-d$ exchange energy. It should be kept in mind that in an interband transition an electron transition with the formation of a hole occurs from the electronic state with the highest energy in the valence band. However, the hole energy is opposite in sign to the electron energy in the valence band, and for this reason its energy decreases with decreasing temperature or increasing the degree of FM order with a magnetic field switched on, if the above-indicated red shift occurs. At present, the temperature dependence of the absorption edge in manganites has not been studied.

In the present work, to obtain information about the temperature dependence of the band gap in the manganite $La_{0.9}Sr_{0.1}MnO_3$, we investigated its spectrum of the diffuse reflection coefficient (DRC). This method is often more suitable for the indicated purpose than the specular reflection method, since in this method reflection from the surface of a powder sample, which has not been subjected to polishing, is studied. It is known that polishing often changes the properties of a surface and contributes various contaminants. This is the method that has been used to determine the red shift of the absorption edge in a number of magnetic semiconductors.[7,8]

The setup for investigating the DRC spectra is described in Ref. 11. The DRC measurements were performed using a single-beam scheme with alternate measurement of the intensity of the light reflected from the sample and reference surfaces. The optical part of the setup was constructed in such a way that the intensity of the light reflected from the surface of crystallites of a powered sample at angles not greater than 6.2° is recorded. This maintains the conditions of applicability of the Kramers–Kronig relations, which are convenient for calculations and which were used to calculate the spectra of the absorption coefficient α from the DRC spectra. The Kramers–Kronig computational method was used.[12] Analysis of the experimental data and calculation of the spectra α were performed with a computer using specially developed programs. It should be noted that this method does give the absolute values of the absorption coefficient. However, the

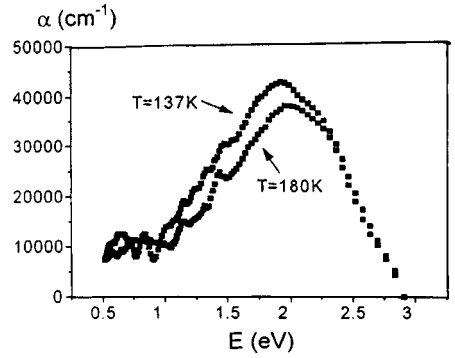

FIG. 1. Absorption coefficient spectra of the composition $La_{0.9}Sr_{0.1}MnO_3$ at two temperatures above and below the Curie temperature.

general form of these spectra gives information about certain properties of the experimental substances, specifically, the fundamental absorption edge. Comparing the absorption spectra obtained by different methods for various substances, including magnetic semiconductors, showed that the error in determining α does not exceed one order of magnitude.

Figure 1 shows the α spectra obtained from the DRC spectra for the compound $La_{0.9}Sr_{0.1}MnO_3$ by the method described above. The form of the curves $\alpha(E)$ clearly indicates that the fundamental absorption edge corresponding to the band gap occurs in this energy range of the incident light. It is known that

$$\alpha \sim (E - E_g)^p \tag{1}$$

for $h\nu \geqslant E_g$ for different types of band structures. Here E_g is the band gap and p usually ranges from 1/2 to 3/2.[13] As one can see from Fig. 1, in the present case p is close to 1. Approximating the linear sections of the spectra obtained at different temperatures T up to intersection with the E axis, we obtained the fundamental absorption edge for different values of T. Its temperature dependence is displayed in Fig. 2. As is evident from this

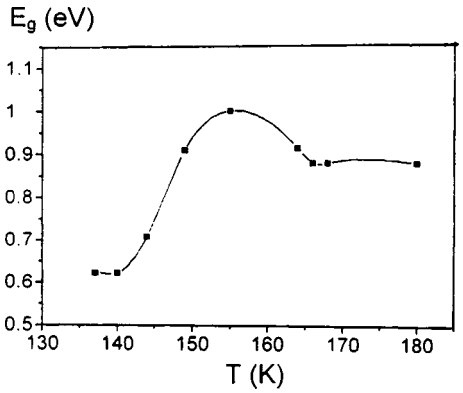

FIG. 2. Temperature dependence of the fundamental absorption edge of the composition $La_{0.9}Sr_{0.1}MnO_3$.

figure, the energy of the fundamental absorption edge decreases rapidly as temperature decreases from the Curie point (155 K). At temperatures ranging from 155 K to 140 K (the lowest measurement temperature is 137 K) the fundamental absorption edge shifts by the giant amount ~ 0.4 eV. This giant red shift of the fundamental absorption edge occurs near the Curie point, i.e., it is associated with the appearance of FM order. A blue shift, characteristic for nonmagnetic semiconductors, occurs above T_C.

The indicated giant red shift of the band gap seems to be due to a shift of the valence-band top, since holes in the indicated compound propagate via manganese ions, with which they have a strong $p-d$ exchange interaction. The presence of a red shift of the valence-band top makes possible the existence of the above-described magnetically two-phase state. Indeed, the experimental compound is a strontium-doped AFM semiconductor $LaMnO_3$ with Néel temperature 1.41 K. Doping of the indicated AFM semiconductor with acceptor ions Sr^{2+} leads to the formation of FM drops, in which holes are concentrated, i.e., to the above-described magnetically two-phase state. In this case, the Curie point is the thermal breakdown temperature of the FM drops. Indeed, near T_C a maximum of the electric resistance and CMR are observed.[2–4] Another confirmation of the magnetically two-phase state in the indicated composition is the negative volume magnetostriction, which we observed at $T<T_C$ and which attests to compression of the sample in a magnetic field.[14] Yanase and Kasuya have shown[15] that the lattice parameters are smaller inside the FM drops of a magnetically two-phase state. The strong dependence of the breakdown temperature of FM order (short-range order in the present case) on the magnetic field also attests to the existence of a magnetically two-phase state in the indicated compound. For example, if T_C is determined by extrapolating the steepest part of the magnetization curve as a function of T to its intersection with the T axis, then the difference between the values of T_C in 3 kOe and 10 kOe fields reaches 40 K. At the same time, in pure $CdCr_2Se_4$ and Gd this difference does not exceed 4 K.[16] This is due to the fact that at temperatures somewhat above the thermal breakdown temperature of FM drops an external magnetic field increases the degree of FM order near impurities more strongly than on the average over the crystal because of a gain in the $p-d$ exchange energy, i.e., it restores the FM drops destroyed by heating.

This work was supported by the Russian Fund for Fundamental Research, Project 96–15–96429.

[1] É. L. Nagaev, *The Physics of Magnetic Semiconductors* [in Russian] (Nauka, Moscow, 1979).
[2] É. L. Nagaev, Usp. Fiz. Nauk **166**, 833 (1996).
[3] A. P. Ramirez, J. Phys.: Condens. Matter **9**, 8171 (1997).
[4] A. Moreo, S. Yunoki, and E. Dagotto, http://xxx.lanl.gov/abs/cond-mat/9901057.
[5] É. L. Nagaev, JETP Lett. **16**, 394 (1972); V. A. Kashin and É. L. Nagaev, Zh. Éksp. Teor. Fiz. **66**, 2105 (1974) [Sov. Phys. JETP **39**, 1036 (1974)].
[6] E. L. Nagaev, Phys. Lett. A **218**, 367 (1996); **239**, 321 (1998).
[7] G. Busch, P. Junod, and P. Wachter, Phys. Lett. **12**, 11 (1964); G. Bush and P. Wachter, Phys. Condens. Matter **5**, 232 (1966).
[8] G. Busch, B. Magyar, and P. Wachter, Phys. Lett. **7**, 438 (1966).
[9] G. Harbeke and H. Pinch, Phys. Rev. Lett. **17**, 1090 (1966).
[10] H. W. Lehmann and F. P. Emmenegger, Solid State Commun. **7**, 965 (1969).
[11] L. I. Koroleva, Sh. Sadykova, and V. Yu. Pavlov, Fiz. Tverd. Tela (Leningrad) **34**, 3638 (1992) [Sov. Phys. Solid State **34**, 1948 (1992)].
[12] R. K. Ahrenkiel, J. Opt. Soc. Am. **61**, 1651 (1971).
[13] T. S. Moss, G. J. Burrell, and V. Ellis, *Semiconductor Opto-Electronics* (Butterworths, London, 1973) [Russian translation, Mir, Moscow, 1976].

[14] L. I. Koroleva and R. V. Demin, Physica B **259-261**, 816 (1998).
[15] A. Yanase and T. Kasuya, J. Phys. Soc. Jpn. **25**, 1025 (1968).
[16] K. P. Belov, L. I. Koroleva, M. A. Shalimova *et al.*, Zh. Éksp. Teor. Fiz. **72**, 1994 (1977) [Sov. Phys. JETP **45**, 1047 (1977)].

Translated by M. E. Alferieff

ERRATA

Erratum: Anomalous magnetic properties of the complex $(ET)_2C_{60}$ [JETP Lett. 69, 785–791 (25 May 1999)]

S. V. Demishev, A. A. Pronin, and N. E. Sluchanko
Institute of General Physics, Russian Academy of Sciences, 117942 Moscow, Russia

L. Weckhuysen and V. V. Moshchalkov
Laboratorium voor Vaste-Stoffysica en Magnetisme, K. U. Leuven, B-3001 Leuven, Belgium

N. G. Spitsina and É. B. Yagubskiĭ
Institute of Chemical Physics, Russian Academy of Sciences, 142432 Chernogolovka, Moscow Region, Russia

[S0021-3640(99)01516-9]

PACS numbers: 99.10.+g, 81.05.Tp, 81.40.Rs, 75.20.Ck, 77.22.Ch

On pages 786 and 788 the term ''vibrating coil magnetometer'' used by the translator is incorrect: The magnetometer was actually a vibrating sample magnetometer. Also, the instrument identified on page 786 as an ''NR-4191 A impedance meter'' was a Hewlett-Packard HP-4191A impedance analyzer.

